



HAL
open science

Multilayer monochromators for EUV and X-ray optics and the interface characterization

Yuchun Tu

► **To cite this version:**

Yuchun Tu. Multilayer monochromators for EUV and X-ray optics and the interface characterization. Other [cond-mat.other]. UPMC Université Paris VI; Tongji University, Shanghai, China, 2015. English. NNT: . tel-01134315v1

HAL Id: tel-01134315

<https://hal.science/tel-01134315v1>

Submitted on 23 Mar 2015 (v1), last revised 12 May 2015 (v2)

HAL is a multi-disciplinary open access archive for the deposit and dissemination of scientific research documents, whether they are published or not. The documents may come from teaching and research institutions in France or abroad, or from public or private research centers.

L'archive ouverte pluridisciplinaire **HAL**, est destinée au dépôt et à la diffusion de documents scientifiques de niveau recherche, publiés ou non, émanant des établissements d'enseignement et de recherche français ou étrangers, des laboratoires publics ou privés.

Université Pierre et Marie Curie

Ecole doctorale 388

Laboratoire de Chimie-Physique-Matière et rayonnement

**Multilayer monochromators for EUV and X-ray optics and
the interface characterization**

Par Yuchun Tu

Thèse de doctorat de Chimie Physique et Chimie Analytique

Dirigé par les Dr. Philippe Jonnard et Pr. Jingtao Zhu

Présentée et soutenue publiquement le 09 Mars 2015

Devant un jury composé de :

Pr. Wanqi Jie

Pr. Li Zhao

Pr. Alain Dubois

Pr. Baozhong Mu

Dr. Jianfeng Sun

Dr. Xianglong Zeng

Pr. Jingtao Zhu (Co-director of thesis)

Dr. Philippe Jonnard (Co-director of thesis)



CONTENTS

Chapter 1 Introduction	3
1.1 Extreme ultraviolet and soft x-ray regions	3
1.2 Multilayer mirrors	4
1.2.1 Theory of multilayers mirrors	4
1.2.2 Material selection for multilayers	8
1.2.3 The imperfection of interfaces	8
1.2.4 Thermal stability	10
1.3 Application of multilayer monochromator	11
1.3.1 Solar astronomy	11
1.3.2 EUV and x-ray spectrometry	13
1.3.3 Plasma diagnosis	13
1.3.4 Synchrotron radiation	14
1.3.2 The contribution of this thesis	16
Chapter 2 Experimental	18
2.1 Sample preparation	18
2.2 X-ray measurements	19
2.3 Fluorescence induced by x-ray standing wave	20
2.4 Nuclear magnetic resonance spectroscopy	22
2.6 Transmission electron microscopy	25
2.7 Raman scattering	25
Chapter 3 Study of barrier layers in Co/Mg multilayers	28
3.1 Introduction	28
3.2 Thermal stability of Co/Mg multilayers	29
3.2.1 Samples	29
3.2.2 Characterization of structure and interfaces	29
3.2.3 Conclusion	33
3.3 Introduction of Zr in Co/Mg multilayers	34
3.3.1 Samples	34
3.3.2 Nuclear magnetic resonance spectroscopy	35
3.3.3 Fluorescence induced by x-ray standing wave	36
3.3.4 Conclusion	42
Chapter 4 Study the thermal stability of carbon-based multilayers	43
4.1 Structural changes induced by thermal annealing in Cr/C multilayers	43
4.1.1 Samples	43
4.1.2 Characterization of structure and interfaces	43
4.2.3 Conclusion	50

Contents

4.2 Interface changes induced by thermal annealing in Co/C Multilayers	51
4.2.1 Samples	51
4.2.2 Characterization of structure and interfaces	51
4.2.3 Conclusion	56
Chapter 5 Improvement of Ti-based multilayers	57
5.1 Introduction	57
5.2 Co/Ti multilayers prepared by reactive sputtering	58
5.2.1 Samples	58
5.2.2 Characterization of structure and interfaces	58
5.2.3 Conclusion	63
5.3 Cr/Ti multilayers prepared by co-deposition of B₄C	63
5.3.1 Samples	63
5.3.2 Characterization of structure and interfaces	64
5.3.3 Conclusion	68
Chapter 6 Study of Mo₂C/B₄C and Mo/B₄C multilayers	69
6.1 Introduction	69
6.2 Optical and structural characterization of the Mo₂C/B₄C and Mo/B₄C multilayers	70
6.2.1 Samples	70
6.2.2 Characterization of structure and interfaces	71
1. Mo/B ₄ C	71
2. Mo ₂ C/B ₄ C	73
6.2.3 EUV reflectivity	75
6.2.4 Conclusion	77
6.3 Stress of the Mo₂C/B₄C and Mo/B₄C multilayers	78
6.3.1 Experimental	78
6.3.2 Results and discussion	78
6.3.3 Conclusion	81
Conclusions and perspectives	82
Reference	85
Appendix: publications	95

Chapter 1 Introduction

1.1 Extreme ultraviolet and soft x-ray regions

The visible light is a very small part of the electromagnetic spectrum, with wavelengths from 380 to 780 nm. The extreme ultraviolet (EUV) range extends from the photon energy of about 30 eV to about 250 eV, with corresponding wavelengths from about 5 nm to 40 nm. The energy of soft x-rays extends from 250 eV to several keV. The application of these spectral regions consists of two sides:

1. The resolution of an optical system is limited by the well-known Rayleigh criterion: $\Delta \sim \lambda/NA$, where NA is the numerical aperture of the optical system and λ the working wavelength. Because the wavelengths are relatively shorter, it is possible to see smaller structures as in EUV microscopy [1] and soft x-ray microscopy [2], and to write smaller patterns as in EUV lithography [3].
2. These spectral regions cover the main atomic resonances and absorption edges of most low and intermediate atomic number elements. This provides mechanisms for elemental and chemical identification. Many analysis methods of spectroscopy are developed, such as emission spectroscopy and absorption spectroscopy etc. These in turn lead to new scientific understandings, for instance in materials science [4], EUV and X-ray astronomy [5, 6] and plasma diagnosis [7, 8].

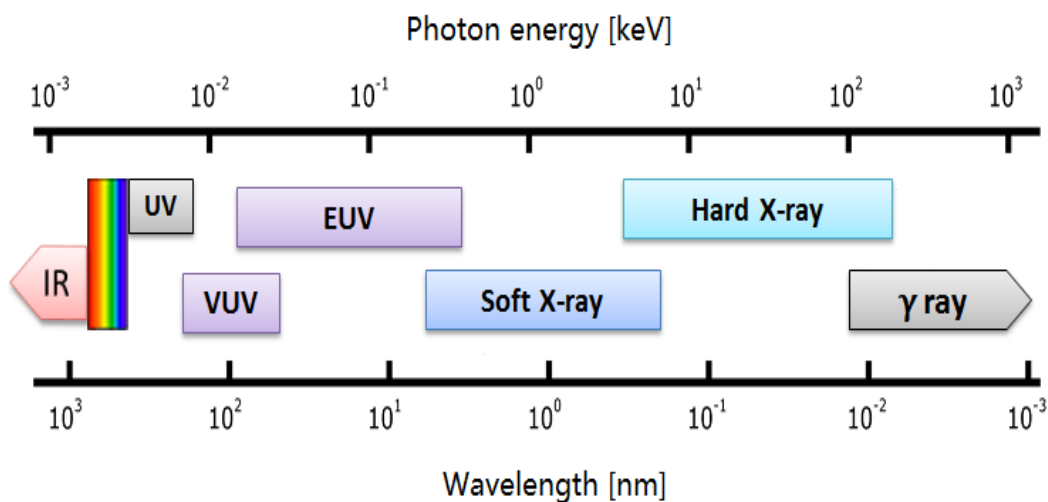


Figure 1.1 The electromagnetic spectrum from the infrared to the γ -ray region.

Chapter 1 Introduction

The optical elements working at EUV and soft x-ray ranges are required in these applications mentioned above. In terms of function, there are imaging elements (spatial resolution), dispersive elements (spectral resolution) and some elements with both functions. At these wavelength ranges, the refractive index of all the materials is close to unity, thus the transmissive lenses cannot be used as optical elements because of their weak optical contrast with air or vacuum. On the other hand, the strong absorption limits the application of single reflective interfaces as mirrors. An exception for achieving high reflectivity is the total external reflection at grazing incident angle [9, 10]. The shortcoming of this optics is their large image aberrations, small collection solid angle and bad spectral resolution. The diffraction elements such as grating and zone plate can offer good spectral resolution. However, they also suffer from strong absorption of materials thus from low diffraction efficiency [11].

Bragg reflection of radiation by the lattice planes of crystalline structures is a well-known phenomenon. It can serve as a technique to analyze crystalline materials and it also can be used to monochromatize x-ray radiation and to design x-ray optics. However, the wavelength ranges are determined by the lattice spacing of the available natural crystals, which are too small to reflect EUV and soft x-ray radiations. This limitation can be overcome by the use of synthetically produced layered structures of alternating materials with a high optical contrast. A multilayer system is composed of alternative layers of two materials. The multilayers permit the achievement of high reflectivity, with a modest spectral bandwidth at EUV and soft x-ray wavelengths. It has been proposed and experimentally demonstrated that it is possible to improve the resolution by making multilayer grating at the detriment of a loss of reflectivity [12-14]. The multilayer gratings can be prepared by multilayer deposition onto a structured substrate or lithographically etching a flat multilayer structure. In summary, multilayers nowadays play an important role for optical applications from the EUV to x-rays ranges.

1.2 Multilayer mirrors

1.2.1 Theory of multilayer mirrors

We consider the case of a multilayer structure deposited on a thick substrate, as shown in Figure 1.2. The N layers having the thickness d_j . The zeroth layer represents the ambient for incident plane wave. The ambient may be vacuum or air. The $(N+1)^{\text{th}}$ layer is the substrate. The equation of a plane electromagnetic wave in the j^{th} layer at a position r can be expressed as:

$$E_j(r) = E_j e^{i\vec{k}_j \cdot \vec{r}} \quad (1.1)$$

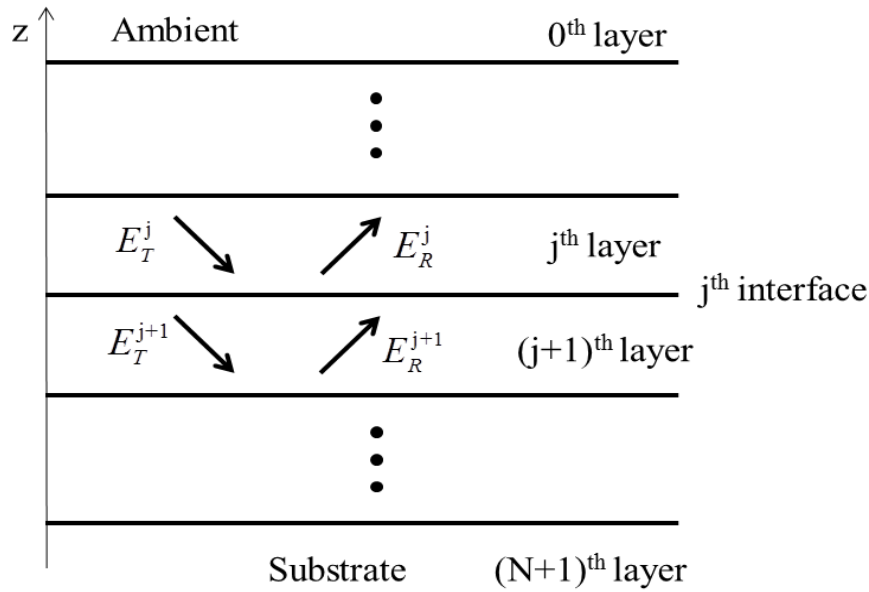


Figure 1.2 The electric field at j^{th} interface of a multilayer.

where E_j is the amplitude of the field at the top of layer j and \vec{k}_j is the wave vector of the j^{th} layer. Its component in z direction is given by:

$$k_z^j = \frac{2\pi}{\lambda} \sqrt{s^2 \sin^2 \theta_j - \delta_j - i\beta_j} \quad (1.2)$$

where θ is the grazing angle of incidence, λ is the wavelength of the x-rays. The refractive index of j^{th} layer is $n_j = 1 - \delta_j - i\beta_j$, where δ_j is the deviation of real part of the refractive index from unity and β_j , the imaginary part, denotes the absorption of x-rays into this material.

The electric field in a layer can be calculated for both s and p polarizations. However, in EUV and x-ray region and usually in grazing incidence and normal incidence condition, the s and p polarizations are almost identical. Here we only consider s -polarization and the boundary conditions at j^{th} layer are:

$$\begin{cases} \mathbf{E}_T^j + \mathbf{E}_R^j = \mathbf{E}_T^{j+1} \\ k_z^j (\mathbf{E}_T^j - \mathbf{E}_R^j) = k_z^{j+1} \mathbf{E}_T^{j+1} \end{cases} \quad (1.3)$$

where E_T^j and E_R^j are the transmitted and reflected x-ray field amplitudes, at the top of j^{th} layer.

The complex coefficients of reflection r_j and transmission t_j at the j^{th} interface can be given from Fresnel's formula:

$$\begin{cases} r_{j,j+1} = \frac{E_R^j}{E_T^j} = \frac{k_z^j - k_z^{j+1}}{k_z^j + k_z^{j+1}} \\ t_{j,j+1} = \frac{E_T^{j+1}}{E_T^j} = \frac{2k_z^j}{k_z^j + k_z^{j+1}} \end{cases} \quad (1.4)$$

Form equation 1.3 and 1.4, the electric field amplitude of reflection and transmission can be solved as:

$$\begin{cases} E_R^j = \frac{1}{t_{j,j+1}} (E_R^{j+1} \cdot e^{-ik_z^{j+1}d_{j+1}} + E_T^{j+1} \cdot r_{j,j+1} \cdot e^{ik_z^{j+1}d_{j+1}}) \\ E_T^j = \frac{1}{t_{j,j+1}} (E_T^{j+1} \cdot e^{ik_z^{j+1}d_{j+1}} + E_R^{j+1} \cdot r_{j,j+1} \cdot e^{-ik_z^{j+1}d_{j+1}}) \end{cases} \quad (1.5)$$

The reflectance from the top of the j^{th} ayer, including multiple reflections is now calculated. The recursive relation can be seen from the calculation of reflectance of the next layer up, which is called Parratt recursive method:

$$\mathfrak{R}_j = \frac{r_{j,j+1} + \mathfrak{R}_{j+1} e^{-2ik_z^{j+1}d_{j+1}}}{1 + r_{j,j+1} \mathfrak{R}_{j+1} e^{-2ik_z^{j+1}d_{j+1}}} \quad (1.6)$$

Because the reflectivity in the substrate is $\mathfrak{R}_{N+1} = 0$, the reflectivity in the ambient can be calculated. Thus the reflectivity of the multilayer is given by $R = |\mathfrak{R}_0|^2$.

For periodic multilayers, all reflected radiation at all interfaces should be added in phase. When the phase factor of one period $e^{-2ik_z d} = 1$ (d is the thickness of one period), interference enhancement occurs, i.e. Bragg condition:

$$2d \sin \theta = m\lambda \quad (1.7)$$

where m is the order of Bragg reflection. Considering the refraction of material, the Bragg

law should be modified as:

$$2d \sin \theta \sqrt{1 - \frac{2\bar{\delta}}{\sin^2 \theta}} = m\lambda \quad (1.8)$$

where $\bar{\delta}$ is the average real part of the refractive index for one period:

$$\bar{\delta} = \frac{d_A \delta_A + d_B \delta_B}{d} \quad (1.9)$$

d_A and d_B are the thickness of the two layers (absorber and spacer, respectively) in one period. Maximum of reflectivity for a multilayer mirror occurs when its period satisfies equation (1.8). It can be describe as an analogy of reflection of crystal as shown in Figure 1.3.

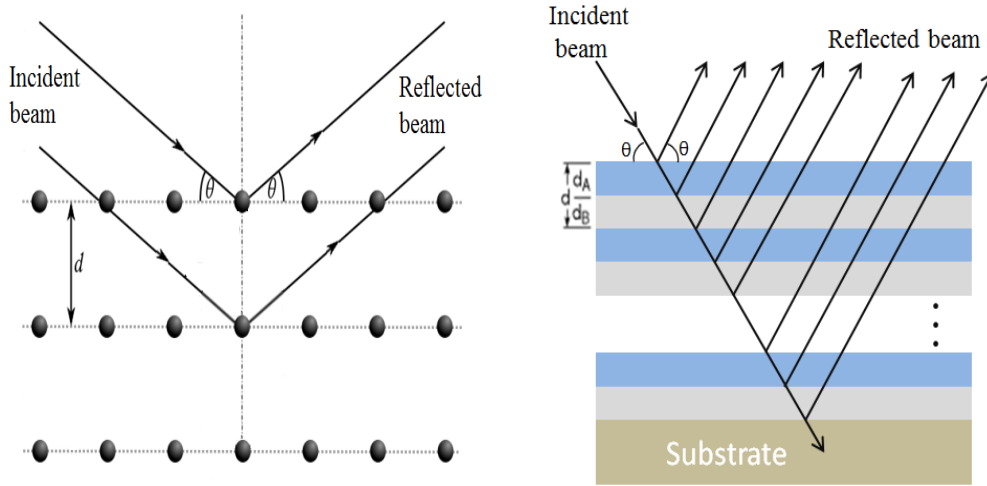


Figure 1.3 Reflection scheme of a crystal lattice (left) and a multilayer stack (right).

From the Bragg law, it is clear that multilayer mirrors can be dispersive elements: at a particular angle, one wavelength is reflected for each Bragg order. The resolving power of a multilayer is given by the kinematical theory of x-ray diffraction [15]:

$$\frac{\lambda}{\Delta\lambda} = \frac{E}{\Delta E} \approx mN_{\max} \quad (1.10)$$

where E is the photon energy and N_{\max} is the maximum number of periods that contribute to the overall reflection. We can conclude that a large number of effective periods increase the resolution of a multilayer mirror. N_{\max} is corresponding to the penetration depth of incident x-rays into the multilayer and determined by the incident angle and the absorption coefficient of materials.

Taking absorption into account, the reflectivity of the multilayer can be increased by reducing the thickness of the absorber layer. The optimum value of the thickness ratio $\Gamma = d_A/d$

is given by [16]:

$$\tan \pi \Gamma_{opt} = \pi \left[\Gamma_{opt} + \frac{\beta_B}{\beta_A - \beta_B} \right] \quad (1.11)$$

1.2.2 Material selection for multilayers

Multilayer for EUV and x-rays can also be seen as an extension of traditional optical coatings to shorter wavelengths. However, the absorption of materials in this wavelength range should be considered. The most important choice of material selection is that of the spacer (low Z) material. To obtain a maximum reflectance, this should be a material with as low absorption as possible at the working wavelength. The absorption coefficient of a material is quite small when the required wavelength is slightly larger than the absorption edge, and the refractive index has greater contrast with another material because of anomalous dispersion [17]. Thus the selection of spacer is dependent on the absorption edges in EUV and X-ray ranges. For example, boron-based multilayers perform well above the boron K-edge at 6.6 nm and Mg-based multilayers are for applications in the range close to the Mg L-edge at 25nm. Selection of the absorber material should be based on a maximum difference in refractive index, specifically in real part. Generally, heavy metals such as Mo, Ru, Cr, W etc. are choosing as absorber layers.

Furthermore, in EUV and x-ray ranges, individual layers are each about a few nanometers thick, i.e. made of 10 to dozens of atomic layers. That is to say that the quality of interfaces greatly affects the optical performance of a multilayer. Thus in addition to optical contrast and absorption, chemical diffusion or reaction of the materials should also be considered while choosing the materials.

1.2.3 The imperfection of interfaces

The interfaces of a multilayer in practice are far from perfect. The optical performance of a multilayer mirror however depends critically on the interface quality which is defined by the morphological roughness and interdiffusion of the two materials at the interfaces. For the diffused interfaces, the refractive index profile perpendicular to the interfaces traces the composition gradient. For rough interfaces, there is discontinuous change in refractive index

at the interface. However, the laterally average profile of a rough interface also presents a gradient, as shown in Figure 1.4. Thus the morphological roughness (σ_r) and diffusion (σ_d) affect the specular reflectivity in the same way: the imperfect interfaces reduces the reflectivity by lowering the optical contrast of the two materials.

In most cases, the imperfection of an interface is taken into account as a Gaussian distribution through a Debye-Waller factor: $\exp(-k^2\sigma^2/2)$, where k is the amplitude of wave vector and σ can be described by $\sigma = \sqrt{\sigma_r^2 + \sigma_d^2}$ [18]. For the calculation of reflectance with imperfect interfaces, equation (1.4) should be multiplied by the Debye-Waller factor. Thus the reflectance is given by:

$$R = R_0 \exp\left(\frac{-4\pi\sigma \sin\theta}{m\lambda}\right)^2 = R_0 \exp\left(\frac{-2\pi\sigma}{d}\right)^2 \quad (1.12)$$

where R_0 is the reflectance from ideal interfaces. According to this equation, the shorter the wavelength, the more the interface width will have a negative impact on the optical performance of multilayer mirrors.

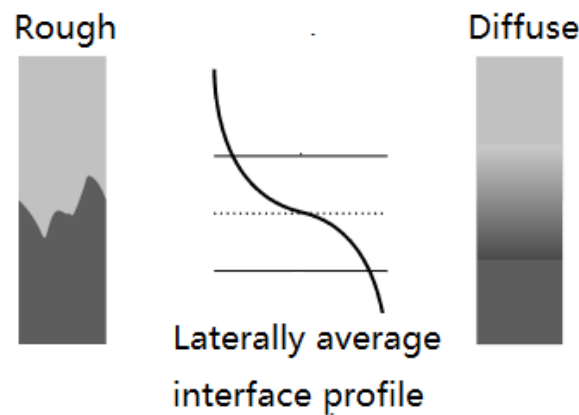


Figure.1.4 Schemes of the interface profile, which describes a rough or diffuse interface.

The interface width of multilayers is typically several atom layers thick. Interdiffusion in these nanoscale multilayers is a phenomenon not as well understood as diffusion in bulk materials. It attracts considerable research interest, not only in understanding of the phenomenon itself, but also in so-called “interface engineering” to improve of the interface quality, thermal stability and stress property in practical applications. The interface engineering methods include diffusion barrier layer, nitrogen incorporation, ion assistance, etc. For example, researchers revealed that Mo/Si multilayers consist of layers of polycrystalline

Mo and amorphous Si that are separated with interdiffusion regions of mixed composition. Diffusion at Mo-on-Si interface was found to be much larger than that at Si-on-Mo interface. Because it is easier for Si to penetrate into the amorphous growing Mo layer at Mo-on-Si interface than for Si to penetrate into textured Mo grains at Si-on-Mo interface [19,20]. Using sub-nanometer carbon or B₄C as diffusion barriers, the reflectance of Mo/Si multilayers can be enhanced [21, 22]. Such an increase was reported from 68.8% at 13.4 nm for magnetron sputtered Mo/Si multilayers, to 70% at 13.5 nm by using B₄C at both interfaces. Reactive sputtering with N₂ was used to deposit Co/C, W/B₄C and Cr/Sc X-ray multilayers [23-25]. In comparison to films deposited non-reactively, reactively-sputtered films show lower stress and lower roughness. Moreover, ultra-thin ($d < 1.7$ nm) Cr/Sc and Cr/Ti multilayers show severe roughness and layer distortions. By using ion-assisted growth (ion energy range of 21 eV to 37 eV and an ion flux of 10 ions per deposited atom), the intermixing, flattening and abruptness of interfaces were improved [26, 27].

1.2.4 Thermal stability

The other parameter, which is crucial for the application of multilayer mirrors, is the stability. Multilayers usually are exposed to high heat-load and large flux radiation for long time, such as in application of synchrotron radiation and astronomy [28-30]. The as-deposited multilayer may not be in thermal equilibrium which generates chemical and physical instabilities. It is known that the structure and interfaces of multilayers can change during heat treatment, e.g. period expansion, interdiffusion and crystallization [31, 32]. Roughness and interdiffusion lead to formation of compounds and interlayers at the interfaces. The two-layer periodic stack may become a three- or four-layer periodic system [33, 34]. Therefore it is necessary to study the possible thermal changes in multilayers when they are in the extreme environments. It helps in not only predicting the optical performance, but also understanding the physical-chemical environment of interfaces in the multilayers in order to improve their stability.

For convenience, the thermal-induced change mechanisms in multilayer are often investigated by thermal annealing instead of real intense radiation. For example, thermal annealing studies of Mo/Si multilayers have shown that the crystallization of layers and

silicides such as MoSi_2 and Mo_5Si_3 grow from room temperature to 800 °C [35]. Another feature of annealed Mo/Si system is the reduction of period due to the formation of denser silicides [36]. In a metal/carbon system, the annealing process usually induces an increasing in the period thickness due to expansion of carbon layers [37, 38] or the crystallization of metal layers [39].

1.3 Application of multilayer monochromator

DuMond and Youtz reported the first positive results of multilayers in 1940 [40]. By evaporation, they made periodic structures composed of alternate layers of Au/Cu, with a period of 10 nm, and observed diffraction of x-rays from the superlattice. However, the diffracting power decayed to zero in just about a month as the interdiffusion of two metals. In 1967, Dinklage found that Fe/Mg structures with a period of 3-5nm can last for more than one year [41]. The peak diffracted intensity for soft x-rays is comparable to that from a lead stearate soap film multilayer structure made by the Langmuir-Blodgett technique. In 1985, Mo/Si multilayers were fabricated by using magnetron sputtering [42]. The measured peak reflectance was 50% at 17 nm. Because of the potential application in semiconductor industry, Mo/Si multilayers were widely studied by many groups all over the world. With the development of micro-machining and high-precision deposition technology, the Mo/Si multilayer reflectors can show reflectance (70% at 13.5nm) very close to theoretical performance. Nowadays, the first machine to produce computer chips using Mo/Si multilayer optics is commercially available [43].

In some science facilities, multilayers provide a modest spectral bandpass with a relatively high throughput, which can be used a monochromator. In the following we will give examples from solar astronomy, EUV and x-ray spectrometry, plasma physics and synchrotron radiation.

1.3.1 Solar astronomy

The temperature range of solar atmosphere is 10^4 - 10^7 K. A lot of emission lines lie in the EUV and soft x-ray ranges. High-resolution imagers comprising normal-incidence telescope

Chapter 1 Introduction

mirrors coated with multilayers tuned to specific coronal or transition-region emission lines have been used in a variety of missions, such as the SOHO [44], TRACE [45] and SDO [46] satellite instruments.

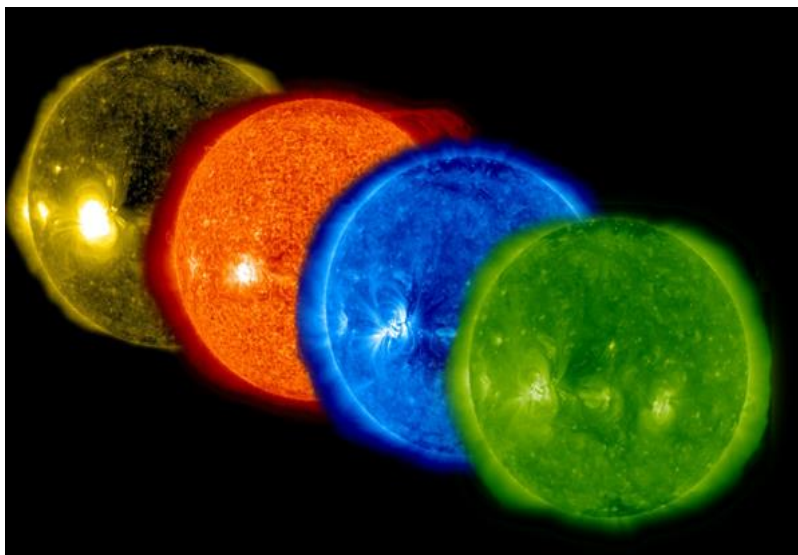


Figure 1.5 EUV images of the solar atmosphere at four wavelengths (17.1, 30.4, 33.5 and 9.4 nm, from left to right)

The use of multilayer coated optics to obtain astronomy images is illustrated in Figure 1.5. This shows images of the solar corona obtained at nominal 17.1 nm, 30.4 nm, 33.5 nm and 9.4 nm (from left to right) [47, 48]. The image was obtained by Atmospheric Imaging Assembly (AIA) instrument aboard the Solar Dynamics Observatory mission (SDO). Four Cassegrain telescopes were coated with Mo/Si (for wavelength at 13.1, 17.1, 19.4, 21.1 nm), Mo/Y (9.4 nm) and SiC/Mg (30.4, 33.5 nm) multilayers. Thus seven EUV channels can be selected in order to observe the solar corona at specific temperatures corresponding to Fe and He ion lines [48].

The multilayer-coated normal incidence optics can provide a powerful tool capable of achieving high spatial resolution, wide field of view, broad wavelength coverage, and moderate spectral resolution ($\lambda/\Delta\lambda \approx 10-100$). The other parameters which are crucial for the application of reflecting mirrors using in outer space, are the thermal and life stabilities. Additional, shorter period multilayers, such as Mo/B₄C, Cr/Ti, Cr/Sc, Co/Mo₂C, W/B₄C and others may lead to the development of narrow-band imagers operating in the soft x-ray, specifically near the Si VII (7.3 nm), C VI (3.4 nm), O VII (2.2 nm), O VIII (1.9 nm), and Fe

XVII (1.7 and 1.5 nm) lines [49].

1.3.2 EUV and x-ray spectrometry

Characteristic emissions available for the analysis of the light elements (Li, Be, B, C, N) are the EUV and soft x-ray K emission bands. The measurement of these radiations is difficult because of their relatively weak intensities arising from the low fluorescence yield and the strong absorption inside the sample. To compensate for these physical effects, it is necessary to use good x-ray monochromators. Lead stearate, made by the Langmuir-Blodgett technique, can be used to analyse these emissions. Multilayers are nowadays widely used to perform wavelength dispersive spectrometry. Compared to Langmuir-Blodgett soap-films, multilayers have some advantages: 1) they have a larger integrated reflectivity, 2) they offer good stability under thermal and radiation loads and under vacuum; 3) they let one choose the material and structures and thus optimize the energy and reflectance.

Mo/B₄C and La/B₄C multilayer monochromators have been reported for the detection of the boron K emission at a large Bragg angle close to 45° [50]. In the water window, a bent Cr/Sc multilayer mirror has been used to study the emissions as monochromators for spectroscopy [51]. The use of these multilayers in a curved-crystal or double-crystal spectrometer lead to a spectral resolution good enough to distinguish the chemical state of the emitting B, N or Sc atoms.

With multilayers as monochromator elements, the quantitative analysis is often difficult or even impossible, in particular in case of two close emission lines because multilayers suffer from moderate spectral resolution due to their large diffraction patterns. In 1993, the principle of a multilayer grating monochromator with an improved resolution was given [52]. The device was fabricated by means of combining deposition of thin films on a nanometer scale, UV lithography and reactive ion etching [53]. It was possible to improve the resolution by factor 2-3 to the detriment with a small loss of reflectivity [13].

1.3.3 Plasma diagnosis

Multilayer mirrors are widely used for the diagnostics of hot plasmas. By using an assembly of multilayer monochromators, multi-channel polychromators can be realized for

spectrally selective radiometry of high-temperature plasmas. A polychromator channel includes a streak camera, a filter cutting off the long-wavelength radiation and a multilayer mirror.

Providing a moderate spectral selectivity, multilayer-based devices offer a high sensitivity and relatively easy way to obtain time and spectral resolution simultaneously. For example, a polychromator for the tokamak facility has five channels at the FOM Institute for Plasma Physics. For measurements of time and spatial distributions of impurity ions in the plasma three spectral lines were chosen: B V (4.86 nm), C VI (3.37 nm) and O VII (2.164 nm) [54].

Researchers in Tongji University have improved this polychromator so that time and spectral resolved one dimensional x-ray imaging can be realized to study implosion dynamics in laser inertial confinement fusion. This facility uses the new optical design of the multi-channel Kirkpatrick-Baez (KB) microscope to obtain high-throughput high-resolution x-ray images at multi-keV energy bands. It consists of a total reflection mirror in the sagittal direction and two multilayer mirrors in the tangential direction. The two multilayer mirrors providing two channels as follow: Cr/C multilayers with $d=8$ nm at 2° grazing incidence for 2.5 keV channel ($E/\Delta E=12$), Cr/C multilayer with $d=6.8$ nm at 1.9° for 3.0 keV channel ($E/\Delta E=15$). Figure 1.6 shows an image of laser irradiated target in a period of 1 ns obtain from this system.

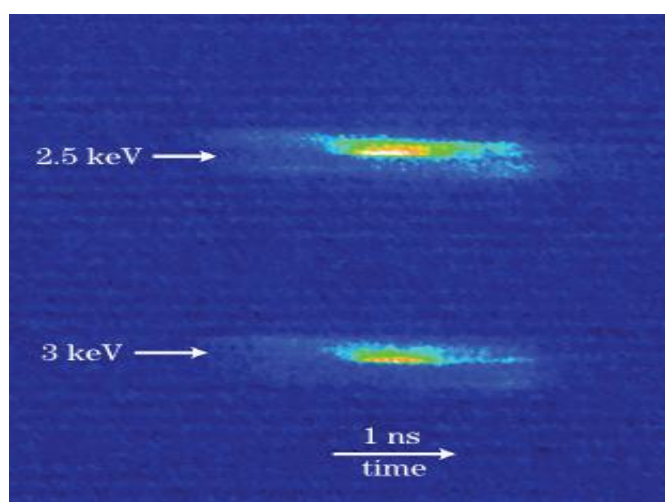


Figure 1.6 Time resolved image of plasma obtained from Cr/C multilayer coated KB mirror

1.3.4 Synchrotron radiation

Multilayers are also used for x-ray optical elements in-between single reflective mirrors and crystals at beamlines of synchrotron radiation. The single reflective mirrors work below the critical angle as a low-pass energy filter. The crystal monochromators, using Bragg reflection at much higher incident angles, have typical energy bandwidth ($\Delta E/E$) of 10^{-4} [55]. The typical energy band width of a multilayer is much larger than that of a crystal. In this way the multilayer reflects a larger portion of the energy spectrum leading to increased integral intensity. Thus multilayer is suitable for some application where medium resolution optics with high throughput is required, for instance x-ray imaging and fluorescence [56, 57], where the narrow bandwidth of the crystal optics is not required. Typical multilayer x-ray optical elements, based on materials such as W/B₄C, W/Si or Ni/B₄C, yield a relative spectral resolution of the order of a few percents.

The multilayer period can be adjusted to arbitrary values, in particular to wavelengths above 1 nm that are hardly or not accessible by crystals. In this wavelength range, multilayer are used to provide a tool for controlling and measuring the polarization properties. The incidence angle is the Brewster angle at which the polarizing power has a maximum. The multilayers are used as polarizers and polarimeters. For example, the multilayer phase retarder are studied at both an SR beam and a laser plasma source near 97 and 277 eV [58] and in the range 390-570 eV [59]. For the water window spectral range, Cr/Sc have been developed [60] to be incorporated into a high precision polarimeter. Using this setup, the full polarization state of the light from the beamline could be determined at energies around 400 and 570 eV.

Curved geometries can be manufactureasily with multilayers that are deposited on bent or curved substrates than bending a crystal to small radii of curvature. Focusing or collimating multilayer optics generally require a lateral thickness gradient to meet with Bragg conditions with varying angle of incidence along the whole length of the mirror [61]. An x-ray beam has been focused in one direction to a width of 7 nm in SPring-8 synchrotron radiation facility by using a Pt/C multilayer coated on a elliptically curved substrate [62].

Another application of multilayers in synchrotron radiation is quantitative analysis of the high order spectral purity in a soft X-ray beamline output. A multilayer is used as a bandpass filter for order sorting with the angle of incidence changing. An example is given in reflectometry of a normal incidence Cr/C multilayer mirror for use around 282 eV [63].

1.4 The contribution of this thesis

As mentioned in 1.2.3 and 1.2.4, for the research of multilayer coatings, great effort can be expected in two areas of : 1) research for new material combinations for multilayer mirrors with improved optical performances; 2) study of interface engineering methods to improve the interface quality and thermal and radiation stabilities. Our work focuses on several material combinations as follows:

Mg-based multilayer mirrors are promising in the 25-40 nm range for Mg L absorption edge lies in 25nm. Co/Mg multilayers are found with minor diffusion and roughness. Besides, Co/Mg multilayers have a slightly better thermal stability than traditional SiC/Mg multilayers. In chapter 3, barrier layers are considered to further improve the optical performance and stability of Co/Mg multilayers. Zr barrier layer can significantly increase the thermal stability of Mg/Co to 400 °C without optical performance degradation. Additionally, analysis of fluorescence induced by soft x-ray standing waves, which can yield valuable information about the depth profiles of specific elements in the multilayers, is discussed in this chapter.

The most important problem for the multilayer working in the range of “water window” is the extremely high sensitivity to interface imperfections. The interest in multilayers containing C and Ti are called for by their high theoretical reflectivity in the range of the anomalous dispersion at their absorption edges. In chapter 4, a comparative study of the thermal stability of Co/C and Cr/C multilayers is described firstly. In chapter 5, two interface engineering methods are used to improve the interfaces of Ti-based multilayers. We intentionally incorporated B and C into Cr/Ti multilayers by depositing ultra-thin B₄C at the interfaces and using reactive sputtering with N₂ to deposit Co/Ti multilayers. We show that the interfaces and soft x-ray reflectivity of Ti-based multilayers are enhanced by interface engineering.

As Co is a ferromagnetic material, the multilayer containing Co can be analyzed by magnetic techniques, for instance nuclear magnetic resonance spectroscopy. In chapters 3 and 4, this characterization technique is used for Co/Mg, Co/Ti and Co/C multilayers to understand the behavior of Co atoms in these multilayers.

Boron-based multilayers are expected to perform well above the Boron K-edge at 6.6nm.

Chapter 1 Introduction

Mo/B₄C multilayers are promising for the wavelengths near 6.7-7nm because of its good thermal stability and it is easy to handle. The shortcoming of Mo/B₄C system is its asymmetric interfaces and high intrinsic stress. The research presented in chapter 6 shows that replacement of molybdenum by molybdenum carbide (Mo₂C) can limit the reaction and diffusion of boron and carbon atoms with molybdenum ones. The thermal stability and stress are also improved by Mo₂C/B₄C multilayer system.

Chapter 2 Experimental

2.1 Sample preparation

High performance EUV and X-ray multilayer mirrors have been successfully deposited with different physical deposition techniques including evaporation [64], sputtering [65] and pulsed laser [66]. Magnetron sputtering and electron beam evaporation are the most widely used. Magnetron sputtering is a plasma vapor deposition (PVD) process in which the plasma is created and where positively charged ions from the plasma are accelerated by an electrical field superimposed on the negatively charged target. The positive ions are accelerated by potentials ranging from several hundred to several thousand electron volts and strike the negative electrode with sufficient force to dislodge and eject atoms from the target. These atoms will be ejected in a cosine distribution from the face of the target and will condense on surface of substrate that is placed close to the sputtering target. The targets are fabricated from materials that one wishes to deposit. Usually, conductive materials can be deposited using a direct current (DC) power supply and insulators can be deposited by using a radio frequency (RF) power supply.

Compared with electron beam evaporation, magnetron sputtering have several advantages: 1) the deposited atoms have higher kinetic energy (about 10 eV, two orders of magnitude higher than electron beam evaporation) so that the deposited films are denser and smoother 2) the thickness of individual layers can be precisely controlled by the sputtering time; 3) it is possible to deposit laterally gradient multilayers on figured substrate.

All the samples in our work are deposited by DC magnetron sputtering system (JGP560C6, SKY Inc., China) with high-purity targets of Co, Mg, Zr, Mo, B₄C, C, Mo₂C, Cr and Ti targets. The working gas is argon (purity 99.999%). The base pressure is 1×10^{-4} Pa and the sputtering gas pressure is 0.13 Pa (1 mtorr). The multilayers are deposited onto ultra-smooth polished Si substrate with surface roughness of 0.3 nm.

A large part of this thesis involves the research of multilayers at elevated temperatures, enabling the study of thermally induced change of structure and interfaces. The samples are mounted on a holder heated by a wire-wound furnace in a vacuum chamber with a base pressure of 3×10^{-4} Pa. The samples are heated at temperatures in the range 200-600 °C

keeping for 1 hour. A thermocouple enables the temperature reading from the holder.

2.2 X-ray measurements

The physical properties of multilayer samples, such as interdiffusion, roughness and crystallinity can be studied by X-ray measurements using X-ray diffractometry at 0.154 nm (Cu K α emission at 8048 eV). The structural qualities of all multilayers have been checked by using X-ray reflectivity using of a grazing incidence X-ray reflectometer (D1 system, Bede Ltd.). The principle of grazing incidence x-ray reflectivity (XRR) at specular direction is mentioned in section 1.2.1. Bragg law corrected for refraction is used to obtain the multilayer period. We can determine individual layer thickness, interface width and layer density by fitting the XRR curves. The fitting process utilizes recursive equation (1.4) for calculating the reflection curve and genetic algorithm for optimization [67].

An additional method to analyze the correlated morphological roughness is diffuse scattering (off-specular). Rocking curves are measured by using the same diffractometer with the detector fixed at the angle of first order Bragg peak, while the detector is scanned around it. In this work, we performed rocking curves measurement for the Co/Mg, Co/Ti and Co/C multilayers. We can know the morphological roughness of the interface by fitting the rocking curve by a kinetic theory (distorted wave Born approximation) [68] with some interface parameters (fractal exponent, correlation length) which can obtained from the X-ray scattering diagram in the out-of-plane geometry [69]. This study is only performed for Co/Mg multilayers. For other multilayers, we can only see the variation of the correlated morphological roughness.

In the condition of grazing incidence, the Bragg diffraction in mainly come from multilayer structures. When the grazing incident angle increases (generally, larger than 20 $^{\circ}$), the Bragg diffraction is due to reflection of radiation by the lattice planes of crystalline structures. Thus X-ray diffraction (XRD) at large angle is a technique which can be used to determine the crystallinity of metal layers or their compounds. Analysis of XRD peak can give some information such as crystallite size, orientation of lattice planes, and identification of compounds. In this thesis, the XRD experiments for Co/Mg, Co/C are performed in the

symmetric (θ - 2θ) geometry by using a Rigaku-Dmax-2550V powder diffractometer.

The reflectivity of multilayers at working wavelength can be made by scanning the wavelength at an incident angle or by scanning the incident angle at a wavelength. The intensity measurements are made by a silicon photodiode which can convert lights into electric currents. The reflectivity is calculated by the ratio of the two currents corresponding to the reflected and direct incident beams. The Co/Mg multilayers are measured on BEAR beamline at the Elettra synchrotron facility, Italy. The measurements of Cr/Ti multilayers are made in on beamline I06 at the Diamond Light Source, United Kingdom, and the Mo/B4C and Mo2C/B4C multilayers on beamline 3W1B at the Beijing Synchrotron Radiation Facility (BSRF), China.

2.3 Fluorescence induced by x-ray standing wave

Angle-dependent X-ray fluorescence (XRF) analysis is an important tool which has been used to investigate the depth profile of impurity atoms in surfaces, thin films and absorbed molecules. Grazing incidence XRF was demonstrated by Becker for the first time in 1983 [70]. Barbee applied the angle-dependent GIXRF to the study of periodic multilayer [71]. X-ray standing waves generated by the multilayers are a sensitive probe to obtain the depth profile of impurity elements and interdiffusion at the interfaces [72]. The fluorescence intensity of a selected element depends not only on the depth profile of the specific atoms inside the sample, but also on the electric field in the multilayer structure, which can be controlled by changing the grazing incidence angle. Compared with XRF, XRR technology is more sensitive to the density variations and surface/interfacial roughness in multilayers. The combined analysis of XRR and XRF permits the determination of consistent micro structural parameters of multilayers.

2.3.1 Theory of Fluorescence induced by x-ray standing wave

Using the model mentioned in section 1.2, the normalized x-ray intensity $I_j(\theta, z_j)$ in j^{th} layer at depth z_j of a multilayer is given by:

$$I_j(\theta, z_j) = \frac{|E_T^j(0) + E_R^j(0)|^2}{|E_T^j(0)|^2} = \left[e^{-\text{Re}(k'_{j,z} z_j)} + \left| \frac{E_R^j(0)}{E_T^j(0)} \right|^2 e^{-\text{Im}(k''_{j,z} z_j)} + \left| \frac{E_R^j(0)}{E_T^j(0)} \right| \left\{ \cos \theta + \text{Re}(k'_{j,z} z_j) \right\} \right]^2 \quad (2.1)$$

where $E_T^j(0)$ and $E_R^j(0)$ are the transmitted and reflected amplitudes of electromagnetic field at the top of j^{th} layer. $k'_{j,z}$ and $k''_{j,z}$ are the real and imaginary part of k_j , the z-component of the wave-vector k . $\nu(\theta)$ is the phase of the electric field ratio and expressed as:

$$\frac{E_R^j(0)}{E_T^j(0)} = \left| \frac{E_R^j(0)}{E_T^j(0)} \right| e^{i\nu(\theta)} \quad (2.2)$$

The XRF yield from element A in a multilayer, $Y_A(\theta)$ is given by:

$$Y_A(\theta) = \sum_{j=1}^N \left(\exp \left[- \sum_{n=1}^{j-1} \frac{(\mu/\rho)_{n,E} \rho_n d_n}{\sin \varphi} \right] Y_{j,A}(\theta) \right) \quad (2.3)$$

$$Y_{j,A}(\theta) = \int_0^{d_j} C_{j,A}(z_j) \times I_j(\theta, z_j) \times \exp \left(- \left[\frac{(\mu/\rho)_{j,E}}{\sin \varphi} \right] \rho_j z_j \right) dz_j$$

where $Y_{j,A}(\theta)$ is the emitted fluorescence intensity by atoms of element A distributed in the j^{th} layer. $Y_A(\theta)$ is calculated by the sum of the contributions from each layer corrected by the absorption from the upper layers. $C_{j,A}(z_j)$ is the concentration profile of element A in the j^{th} layer. ρ_j is the density of j^{th} layer. $(\mu/\rho)_{j,E}$ is mass attenuation coefficient of j^{th} layer at the energy of emitted fluorescence. φ is the take-off angle of the emitted fluorescent x-rays from the surface.

2.3.2 Experimental

On the BEAR beam line at Elettra synchrotron radiation facility. We perform angle-dependent XRF measurements induced by x-ray standing waves (XSW) in Co/Mg based periodic multilayers. The incident beam and detector are fixed and the sample is rotated.

Chapter 2 Experimental

The angle between the incident beam and the fluorescence detector is about 60° due to mechanical constraints.

Two different experiments are done as a function of the glancing angle: 1) grazing incidence fluorescence (GIF), the grazing incident angle are varied in the range of the Bragg peak of the incident radiation, 2) grazing exit fluorescence (GEF), the grazing exit angle are varied in the range of the Bragg peak of the fluorescence radiation. In this case, the incident angle is large (between 110 and 120°) and the sample surface is very close to the direction of detector, as shown in Figure 2.1.

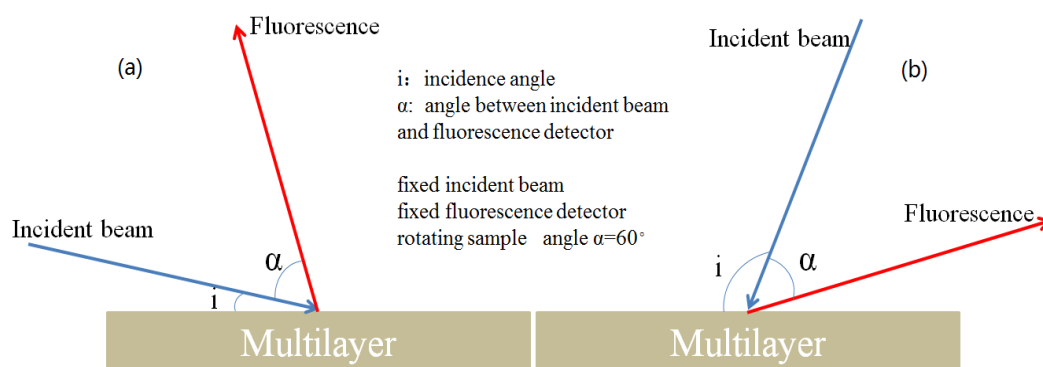


Figure 2.1 Scheme of the x-ray fluorescence experiments in the (a) grazing incidence and (b) grazing exit (b) modes.

In the GIF case, the resolution is governed by the divergence of the incident beam, which is generally quite small on synchrotron beam lines. A $50 \mu\text{m}$ wide slit is put into the path of incident beam to further decrease the divergence of the beam. In the GEF case, the angular resolution is governed by the aperture of the detector. The original aperture of the detector is 0.9° . In order to decrease the aperture of the detector, a 0.5 millimeter wide slit is put between the detector and the sample. The fluorescence radiation is detected by using a silicon drift detector cooled to around -15°C . For each experiment, two different energies of incident beam are used: 807.6 eV for Co $L\alpha$ emission and 1332 eV for Mg $K\alpha$ emission.

2.4 Nuclear magnetic resonance spectroscopy

Nuclear magnetic resonance (NMR) spectroscopy is based on the fact that nuclei of atoms have magnetic moment that can be utilized to yield chemical information. The NMR

Chapter 2 Experimental

allows the observation of specific quantum mechanical magnetic properties of the atomic nucleus. There are two possible measurement techniques. One is the conventional NMR where the sample needs to be placed in a high magnetic field. The applied magnetic field serves several purposes. Most nuclei have two states: spin-up and spin-down. When nuclei are placed in a magnetic field, the spin-down state is at a higher energy level than the spin-up state. The sample is excited by radio waves and then we measure the energy absorbed or emitted when nuclei flip between the two states. The same nuclei in different parts of a molecule have slightly different transition frequencies. Thus measuring these frequencies allows determining the environment of particular atoms in the molecule. The other one is the zero-field NMR; in this mode no external field is applied and the nuclei are excited by the oscillation of the hyperfine field which is created by the spontaneous magnetic moment in the magnetic materials.

The zero-field NMR spectroscopy for magnetic material probes primarily the hyperfine field, which is arising from local magnetic moments around the observed nuclei. The hyperfine field determines the NMR frequency and its strength depends on the local symmetry and chemical environment of the probed nuclei [72, 73]. This analysis yields the fractions of atoms involved in the various atomic configurations or structural components in a sample. In the materials which contain magnetic and non-magnetic composites, these are mainly the bulk of the magnetic phase and its interfaces with the other phase. For a perfect Co/X multilayer, the spectrum should exhibit two peaks: one for the bulk part of Co layers and another for Co atoms at the interfaces because the alien atoms as nearest neighbor of the probed atoms shift the resonance frequency. In real multilayers, there are a certain amount of interdiffusion and admixture at the interfaces. Thus the peaks usually become broad since the NMR reflects the probability distribution of all nearest neighbor configurations in the samples (each configuration giving rise to a characteristic structure in the spectrum) .

In this thesis, zero-field NMR spectra of the Co-based (Co/Mg, Co/C, Co/Ti) multilayers are performed with the homemade automated broadband NMR spectrometer of IPCMS, Strasbourg. All the multilayer samples are made measured at 2K since the NMR signal increases as the inverse of the measurement temperature according to Curie's law. All spectra have been recorded for different values of radio frequency field strengths allowing for

correcting the NMR intensities with a frequency dependent enhancement factor. The NMR spectra represent the distribution of Co atoms versus their resonance frequency.

2.5 X-ray photoelectron spectroscopy

X-ray photoelectron spectroscopy (XPS) is an important surface characterization method which combines surface sensitivity with the ability to obtain elemental and chemical state informations. In the area of thin films, XPS is a widely used analytical tool to give useful information such as composition, chemical state, and thickness etc. of thin films. The principle of XPS is based on the photoelectric effect proposed by Einstein in 1905. This process can be expressed by the equation [74] : $E_{binding} = h\nu - E_{kinetic} - \phi$, where $E_{binding}$ is the binding energy of the electron in the atom (a function of the type of atom and its environment), $h\nu$ is the photon energy of x-ray source, $E_{kinetic}$ is the kinetic energy of the emitted electron that is measured in the XPS spectrometer and ϕ is the work function dependent on both the spectrometer and the detected material. Al K α (1486.6eV) or Mg K α (1253.6eV) are common the photon energies. The XPS technique is highly surface sensitive due to the short inelastic mean free path of the photoelectrons that are excited from the solid. The energy of the emitted photoelectrons is determined using an analyzer and this gives a spectrum with a series of photoelectron peaks. The binding energy of the peaks are characteristic of each element. The peak areas can be used (with appropriate sensitivity factors) to determine the composition of the materials surface. Normally, in the outmost several nanometer of thin films surface XPS can identify all elements (at concentration larger than 0.1 atomic %) except H and He [74]. The detailed information of each element in the thin film can be obtained from the narrow scan spectrum of XPS.

XPS measurements are carried out for the Cr/Ti and Cr/C multilayer. The measurements are performed on a Thermo Scientific K-Alpha system with an Al K α source. The binding energy scale is calibrated from hydrocarbon contamination using the C 1s peak at 284.6 eV. The surfaces of samples are removed by argon ions (3 keV) sputtering until we can get the information of the interface before the measurements. Narrow scan spectra are analyzed using a nonlinear Shirley-type background. The peak positions and areas are optimized by a

weighted least-squares fitting method using 70% Gaussian, 30% Lorentzian lineshapes.

2.6 Transmission electron microscopy

Cross-section transmission electron microscopy (TEM) can provide 2D analysis for a 3D specimen and magnifications of hundreds of thousands times can be routinely obtained for many materials making it an ideal method for the study of multilayers [75]. A focused high energy electron beam (40 to 400 keV) penetrates a thin perpendicular slice of the multilayer. It contains information about the structure of the slice that is magnified by an objective lens system. From the TEM images, darker areas of the image show that the sample is thicker or denser in these areas, so we can observe the different components and structures of the specimen from a grayscale. TEM provide a high resolution image for nanomaterials but also it can distinguish each layer within a nanostructured material. Additionally, the selected-area electron diffraction SAED can be performed for a part of the specimen. It is similar to XRD, but unique as areas as small as several hundred nanometers in size can be examined, whereas XRD typically samples areas having several centimeters in size.

The Cr/Ti, Mo/B₄C, Mo₂C/B₄C multilayers are measured by using high resolution TEM (FEI-TECNAI G2 F20) operated at 200 kV. For preparation of sliced sample, the multilayers are thinned by dimpling that followed by ion milling to get a large electron transparent area. Ion milling is carried out using a 5 keV Ar ion beam at 5 ° grazing angle.

2.7 Raman scattering

Raman scattering (RS) is a standard nondestructive tool for the characterization of crystalline, nanocrystalline, and amorphous carbon since it is sensitive to changes in translational symmetry in materials [76]. The RS spectra of disordered graphite show two sharp modes: the G peak around 1580 cm⁻¹ and the D peak around 1360⁻¹, usually assigned to zone center phonons of E_{2g} symmetry and K-point phonons of A_{1g} symmetry, respectively. The unusual fact is that G and D peaks, of varying intensity, position, and width, continue to dominate the RS spectra of nanocrystalline and amorphous carbons, even those without widespread graphitic ordering. The visible RS spectra depend formally on the configuration of the sp² sites in sp²-bonded clusters.

Chapter 2 Experimental

In this thesis, we made the RS on Cr/C multilayers, both un-annealed and annealed, which have (for those annealed to 600 °C) period expansion. The RS are carried out with a HORIBA JOBIN YVON HR-800 Raman instrument using an argon-ion laser operating at 514.5 nm. Considering the balance between the signal-to-noise ratio and the measuring time, we chose an integration time of 5 s and took 10 accumulations for each spectrum. The RS are made in a backscattering mode at room temperature. The RS spectra can be decomposed into two Gaussian lines, where the line position and full width at half maximum are given with a fitting error lower than 10 cm^{-1} .

Some common characterization methods mentioned above are listed in Table 2.1:

Table 2.1: Lists all the analysis techniques used in our work and their advantages and disadvantages.

Technique	Principle	Information	Advantages	Disadvantages
XRR	Bragg diffraction in one dimension structure	Individual layers, roughness of interfaces, density of material	Non-destructive	Fitting data from several variables
XRD	Bragg diffraction by lattice plane	Crystalline structure	Non-destructive	No in-depth information
Fluorescence excited by XSW	The emission of x-rays in the process of ionization, excited by photons	Depth profiles of impurity elements	Elemental specific, non-destructive	Insensitive to density variations and surface/interfacial roughness
NMR	Magnetic properties of atomic nuclei	Atom local chemical environment	Non-destructive	Only sensitive particular elements, no in-depth information
TEM	The interaction of the electrons transmitted through the specimen	Cross-section of multilayer structure	High in-depth resolution	Intensity scale has no calibration

Chapter 2 Experimental

XPS	The emission of inner-shell electrons excited by photons	Chemical state of layers and interfaces	Elemental specific, non-destructive	No in-depth information
RS	Inelastic scattering of light by molecular vibrations	molecular structure, disorder and crystallite	Elemental specific, non-destructive	No in-depth information

Chapter 3 Study of barrier layers in Co/Mg multilayers

3.1 Introduction

Co/Mg multilayers are promising for application in the EUV range close to the Mg L edge around the wavelength of 25 nm (50eV). Compared with Mg/SiC, [77, 78] Mg/Y₂O₃, [79] and Mg/Sc/SiC [80], Co/Mg multilayers have narrower bandwidth which leads to better spectral resolution, making it more attractive for applications, such as monochromatic solar imaging, in particular for the observation of the 30.4 nm He II emission.

Multilayers mirrors usually endured a high flux of incident light or high heat loads in applications such as synchrotron radiation and astronomical observation. Mg is known to have a low melting point (650 °C) [81], much lower than those of traditional multilayer materials such as Mo (2622 °C) or Si (1410 °C), making it difficult to improve the thermal stability of Mg-based multilayers. Previous studies demonstrated that Mg/SiC and Mg/Y₂O₃ are thermally stable below the temperature of 200 °C, but start to deteriorate drastically at higher temperatures. Thus, it is important to investigate the thermal stability of Mg/Co multilayers.

From the phase diagram, the Mg-Co system is stable in the solid state up to a high temperature. The only possible compound is MgCo₂ [82]. Mg/Co can be stable at 200 °C [83] and further investigation on the heat resistance of this multilayer is rare. To improve the thermal stability, diffusion barrier layers can be inserted between the Mg and Co layers. B₄C is a stable ceramic and typical diffusion barrier material in multilayers. The efficiency of B₄C barrier layer has been demonstrated for the Mo/Si multilayers [21, 22]. However, B₄C barrier layer is disastrous in Mg/Co multilayer mainly due to the poor quality of Mg-B₄C interface [84]. Zr is also barrier layer candidates to prevent interdiffusion in Mg/Co multilayer induced by annealing since Zr cannot chemically react and maintain relatively stable phase with Mg. Mg/Zr multilayers show the best thermal stability in the Mg-based multilayers as they preserve 87% of their original reflectivity in 400 °C annealing and 50% even after 600 °C annealing [85].

Section 3.2 examines Mg/Co multilayers and their thermal stability by studying interdiffusion, interfacial compound formation and roughness development. In Section 3.3,

the property of Mg/Co multilayer with Zr diffusion barrier layers are investigated. An application of NMR and fluorescence induced by x-ray standing waves in Co/Mg based multilayers is also discussed.

3.2 Thermal stability of Co/Mg multilayers

3.2.1 Samples

The Co/Mg multilayers are designed with period $d=16.9$ nm with 30 bi-layers and thickness ratio (thickness of the Mg layer to the period, d_{Mg}/d) $\Gamma=0.85$, achieving high reflectivity for 25.2 nm wavelength at 45° incident angle. To investigate the thermal behavior of Co/Mg multilayers, the samples are annealed from room temperature to 300 °C, 350 °C or 400 °C and for one hour in a furnace with a base pressure of 3×10^{-4} Pa. After annealing, the samples are cooled down to room temperature naturally.

3.2.2 Characterization of structure and interfaces

1. EUV and X-ray reflectivity

The thermal stability of Mg/Co is described by the measured X-ray and EUV reflectance results shown in Figure 3.1. The measured EUV reflectance of as-deposited sample is 43% in Figure 3.1(a). It shows slight decrease at 300 °C and then, notable decline at 350 °C, while no reflectance is obtained after 400 °C annealing. Figure 3.1(b) presents the XRR curves of Mg/Co multilayers. After 300 °C annealing, despite that the Bragg peaks remained intense, the 8th and higher Bragg orders have shifted a little and broadened, indicating a slight period thickness contraction and the development of interdiffusion. When it comes to 350 °C, the multilayer encountered a significant change and the high Bragg orders were not so well-defined compared to the unannealed sample. The roughness of interface increased remarkably and the individual thickness change notably after 300 °C annealing. After 400 °C annealing, no Bragg peaks is obtained by the XRR measurements indicating that the annealed sample had no periodic structure. Mg/Co multilayer stayed constant below 300 °C and the multilayer structure and reflectance changed when being annealed at 300 °C or higher temperatures. After 400 °C heat treatment, the multilayer structure has been destroyed and the

reflectance decline to near zero. These structural changes can probably be attributed to the drastic interdiffusion or crystallization in the multilayer, which results in degradation of optical performance.

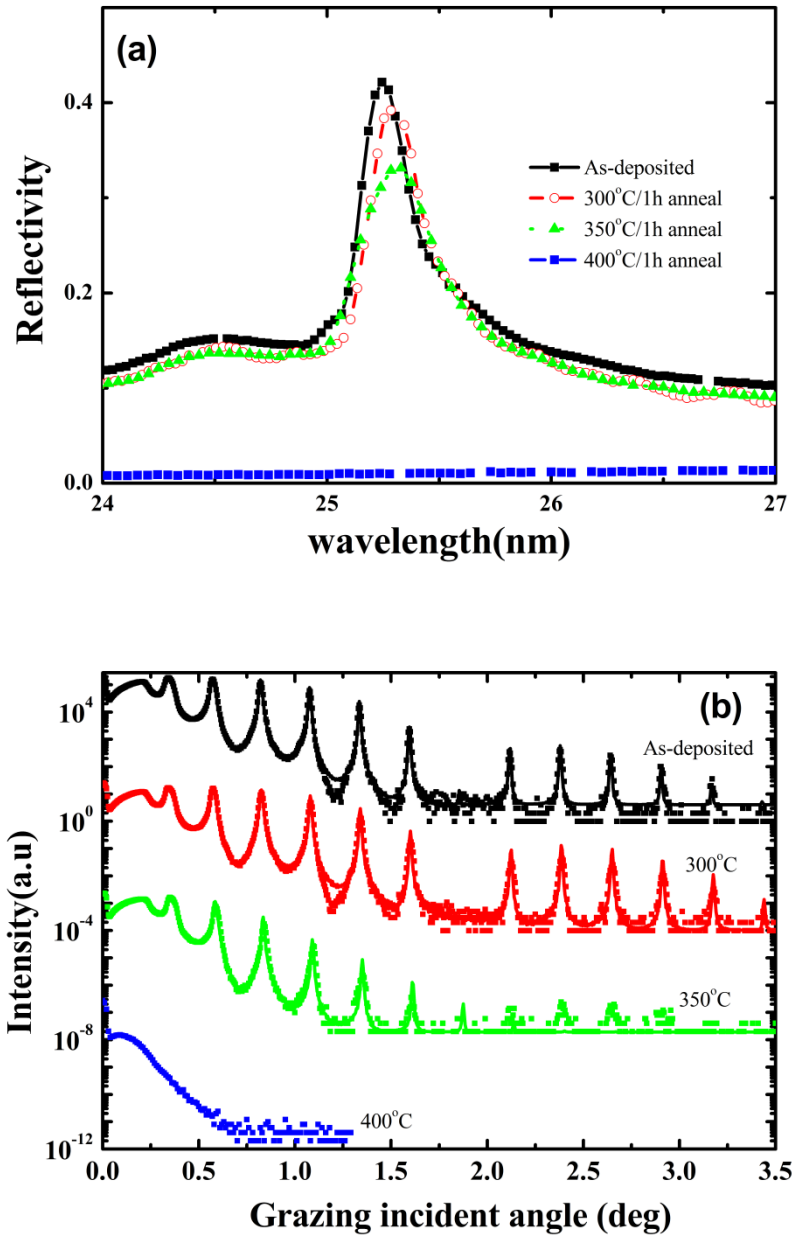


Figure 3.1 (a) EUV reflectance curves of Mg/Co multilayers before and after annealing (b) XRR curves of Mg/Co multilayers before and after annealing, each curve has been shifted vertically by 4 orders-of magnitude for better discrimination, scatter and solid lines represent measured and fitted XRR curves, respectively.

2. X-ray diffuse Scattering

The X-ray scattering diagram of the as-deposited sample in the out-of-plane geometry is

showed in Figure 3.2 (a). The integration method was used to analyze the measured diagrams. A detailed description of the methods can be found in Ref. [69]. There is no obvious change for the annealed samples thus they are not presented here. The red area represents the high intensity and the blue area represents the low intensity. There are four Bragg sheets in the diagram. The black area between the first and second Bragg sheets is the beamstop which is inserted to shade the reflected beam. According to Stearns [86], the full width at half-maximum (FWHM) of the m^{th} Bragg sheet (q_z direction) is proportional to ξ_{\perp} , the vertical correlation length, i.e. $\text{FWHM} \approx 2m\pi/\xi_{\perp}$. The analyzed result of vertical correlation length is shown in Figure 3.2 (b). The power spectral density (PSD) function is shown in Figure 3.2 (c). It shows a linear feature in the log–log plot at high q_y values, thus indicates the power-law asymptotic behavior. The exponent γ is found to be -3.85 by power-law fit and this exponent is associated with the static roughness exponent (also called the fractal exponent) $\alpha = 0.928$. The autocorrelation function (ACF) which is the Fourier transformation of PSD function, is shown in Figure 3.2 (d). The lateral correlation length ξ_{\parallel} is equal to 16.7 nm, deduced by fitting the ACF. The vertical correlation length, lateral correlation length and fractal exponent is 123 nm, 16.5 nm, 0.915 for the 300 °C annealed sample and 118 nm, 16.3 nm, 0.922 for the 350 °C annealed sample, respectively.

The results of XDS (rocking curve) are presented in Figure 3.3. After 300 °C annealing, the XRD curve is similar with the one of as-deposited sample but the intensity of scattering decreases at 350 °C. We can know the geometrical roughness of the interface by fitting the XDS curve by using the parameter (ξ_{\perp} , ξ_{\parallel} and α) obtained from the X-ray scattering diagram. After 350 °C annealing, the geometrical roughness decreases.

The roughness deduced from the fitting of XRR (σ_t) is an overall imperfection of interfaces, including the contributions from both geometrical roughness (σ_r) and interdiffusion (σ_d). According to the equation $\sigma_t^2 = \sigma_r^2 + \sigma_d^2$, the interface width can be calculated. These values are collected in Table 3.1. They show that σ_t increases with the increasing of temperature but σ_r has a decreasing tendency. That is to say, the deterioration of the interface is due to the interdiffusion of the layers of Co and Mg.

Table 3.1 Parameters of the Co/Mg multilayers deduce from fitting the XRR and XDS curves.

Annealed temperature (°C)	Periodic thickness (nm)	XRR fitting		XDS fitting		σ_d (nm)	
		σ_t (nm)		σ_r (nm)			
		Mg on Co	Co on Mg	Mg on Co	Co on Mg	Mg on Co	Co on Mg
As-deposited	16.9	0.47	0.46	0.29	0.31	0.37	0.34
300	16.7	0.52	0.53	0.29	0.30	0.43	0.44
350	16.7	0.71	0.68	0.25	0.26	0.66	0.63

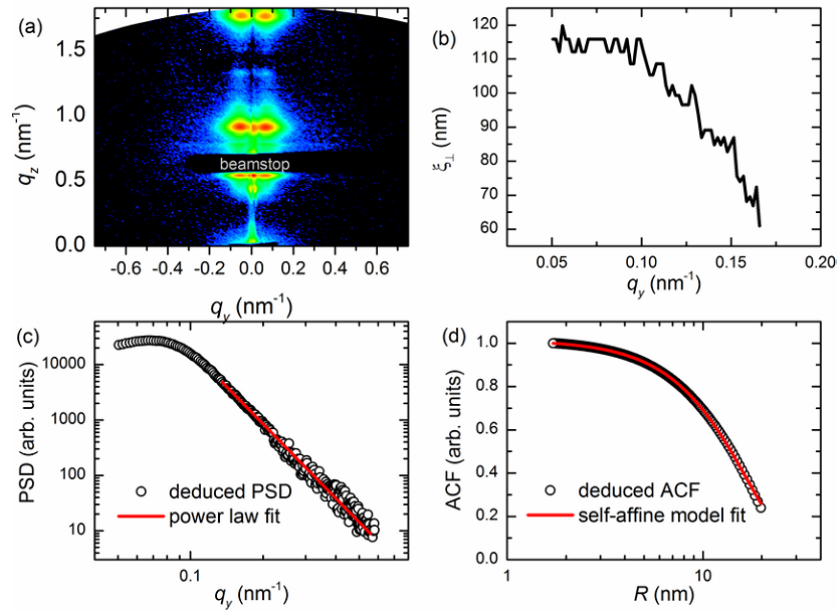


Figure 3.2 (a) X-ray scattering diagram of Co/Mg multilayer, as-deposited; (b) the curve of vertical correlation length; (c) PSD and the fitting curve; (d) ACF and the fitting curve.

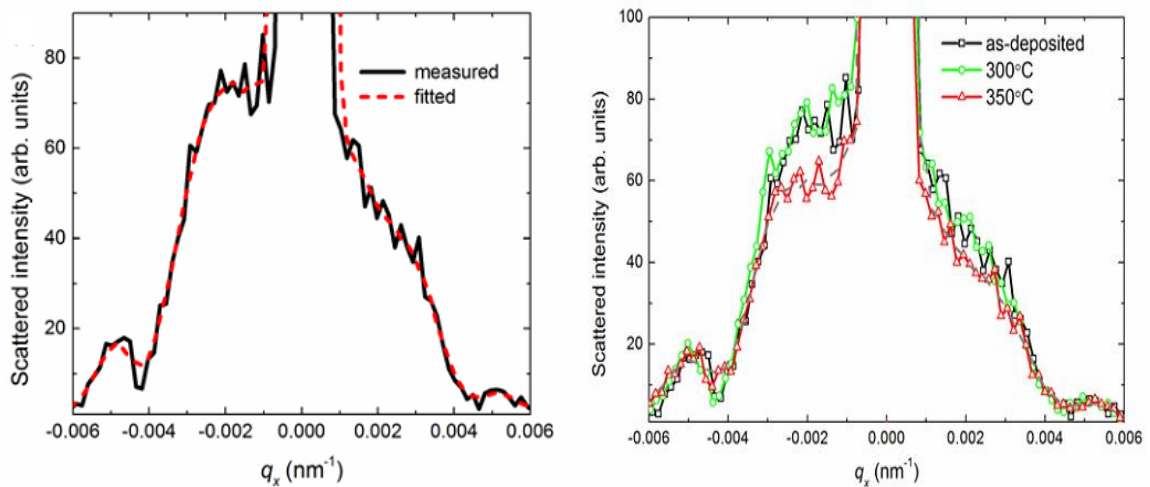


Figure 3.3 X-ray diffuse scattering (rocking curve) of Mg/Co multilayer, (left) as-deposited sample, measured and fitted curve; (right) as as-deposited and annealed sample.

3. X-ray Diffraction

Results of XRD are illustrated in Figure 3.4. For the as-deposited sample, two obvious diffraction peaks can be observed around 34.6° and 44.5° which correspond to Mg *hcp* (002) and Co *hcp* (002) planes respectively. When annealing to 350°C , the intensity of the two peaks reduces, which is attributed to the diffusion between the Co and Mg layers during annealing. The peaks shift slightly toward low angles, meaning that the lattice constant of Co and Mg increases after annealing. After 400°C annealing, it shows only one strong peak around 44.57° . This peak can be related to MgCo_2 *hcp* (201) plane and Co *hcp* (002) plane. In our previous studies [87], for the 400°C annealed sample, the NMR results showed a well-defined line at 226 MHz which corresponds to Co atoms lying in the bulk of the Co layers with an *hcp* structure. However, the contribution of the Co atoms at the Co/Mg interfaces (156 MHz) vanishes after annealing. That is to say, Co and Mg layers mix completely and the multilayer structure is destroyed after 400°C annealing, which is consistent to XRR curves. The films are converted into crystalline compound MgCo_2 with embedded Co grains, which contribute to the XRD peaks.

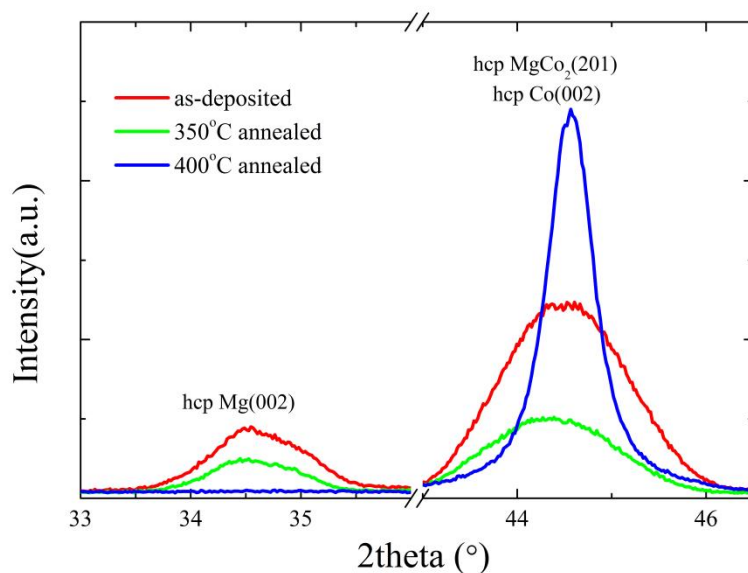


Figure 3.4 XRD curves of Mg/Co multilayers before and after annealing

3.2.3 Conclusion

Co/Mg multilayers are fabricated and annealed up to 400°C . Both Co and Mg layers are

in crystalline state before annealing, and the EUV reflectance is 42%. Co/Mg multilayers have a slightly better thermal stability than SiC/Mg multilayers as they start to degrade at 300 °C annealing while SiC/Mg multilayers do so at 200 °C annealing. However they are both completely destroyed at 400 °C annealing. The degradation of Co/Mg multilayers in the annealing process is attributed to MgCo₂ formation following interdiffusion according to XRD measurements. To further improve the thermal stability, diffusion barrier layers can be inserted between the Mg and Co layers.

3.3 Introduction of Zr in Co/Mg multilayers

Our previous study shows that the introduction of Zr barriers can not only enhance the promising optical performance of the Mg/Co system but also improve the thermal stability from 200 °C to 400 °C [84]. The experimental EUV reflectivity at 25.1 nm and 45° of grazing incidence for Mg/Co, Mg/Zr/Co, Mg/Co/Zr is equal to 42.4%, 41.4%, 50.0%, and 40.6%, respectively. The addition of Zr at the only Mg–on–Co interface has been proven to be an efficient combination to enhance the reflectance. The Mg/Zr/Co/Zr multilayer almost kept its abrupt interfaces and high EUV reflectance when heated up to 400 °C. Despite that a slight decrease of EUV reflectance can be noted after 400 °C annealing, the multilayer structure has no obvious changes according to the XRR measurement.

However, introducing a Zr layer at one or at the other interface or at both interfaces of Mg/Co does not induce an equivalent effect on the optical performances. We are interested in understanding this asymmetrical behavior by correlating the mirror reflectivity to the quality of its interfaces.

3.3.1 Samples

We prepare two sets of Co/Mg-based multilayers. The first is designed for high reflectivity at 25.1 nm at 45° incidence angle. This set is performed for NMR measurements. The thickness is expressed in nm: Mg (14.45)/Co (2.55); Mg (13.20) /Zr (1.50) /Co (2.50); Mg (13.20) /Co (2.50) /Zr (1.50); Mg (12.00) /Zr (1.50) /Co (2.00) /Zr (1.50). For the XRF measurements, the thickness of Mg layers are reduced to 5.45 nm in order to meet the Bragg

condition when the energy of incident light is near 807.6 eV for Co L α emission and 1332 eV for Mg K α emission.

3.3.2 Nuclear magnetic resonance spectroscopy

The NMR spectra of all samples are presented in Figure 3.5. On one hand, the Mg/Co and Mg/Co/Zr spectra are both characterized by a well-defined and intense line at 226 MHz due to bulk *hcp* Co and a shoulder at 156 MHz related to the Co/Mg interface. In the spectrum of Mg/Co/Zr, we note the additional presence of a shoulder at 180 MHz corresponding to the Co/Zr interface. On the other hand, the 226 MHz line is no more observed in the spectra of Mg/Zr/Co and Mg/Zr/Co/Zr: they are made of a wide and flat feature covering the whole frequency domain.

From this distinction, we can deduce that: 1) the Co layers and related interfaces are well-defined in Mg/Co and Mg/Co/Zr, giving evidence in Mg/Co/Zr system that the Zr-on-Co interface is sharp. 2) no more pure Co layers remain within Mg/Zr/Co as a consequence of an intermixing between upper Co and lower Zr layers at the Co-on-Zr interface. A careful look at the Mg/Co/Zr and Mg/Co spectra shows significant differences: lower amplitude and broadening of the *hcp* Co bulk line and larger intensity in the low-frequency range. This suggests that the Zr-on-Co interface in Mg/Co/Zr is not as sharp as the Co-Mg interface in Mg/Co.

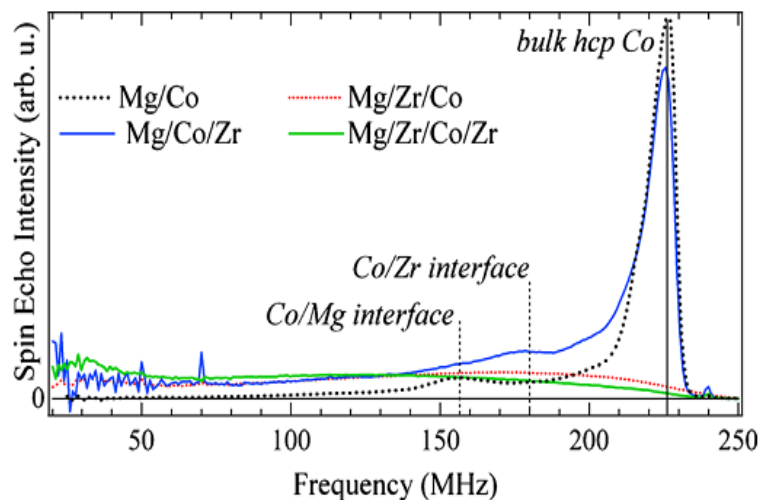


Figure 3.5 NMR spectra of the Mg/Co, Mg/Zr/Co, Mg/Co/Zr, and Mg/Zr/Co/Zr multilayers.

3.3.3 Fluorescence induced by x-ray standing wave

We show in the figure below a typical spectrum obtained when both Co 2p and Mg 1s electron levels can be ionized. In this case the photon energy is 1332 eV. The low energy peak is the Co $L\alpha$ emission (in fact the spectral resolution of the detector is not enough to separate Co $L\alpha$ and Co $L\beta$ emissions); the high energy emission is the Mg $K\alpha$ emission. During the experiments with excitation incident photon energies of 807.6 eV, only the channels corresponding to the Co $L\alpha$ emission are taken into account. With excitation incident photon energies of 1310, 1332 and 1492 eV, only the channels corresponding to the Mg $K\alpha$ emission are taken into account.

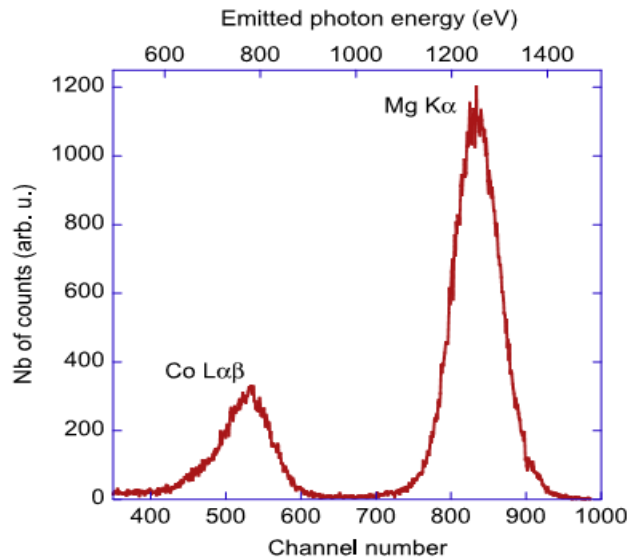


Figure 3.6 X-ray fluorescence spectrum excited at photon energy of 1332 eV.

Figure 3.7 shows the measured XRR curves of samples of Mg/Co, Mg/Zr/Co and Mg/Co/Zr multilayers at x-ray photon energy of 8 keV. The XRR curves are fitted based on the genetic algorithm in order to derive the actual layer thickness and interface roughness. The fitted results agree quite well with the experimental data, which are shown in Table 3.2.

The measured XRF yields of the multilayer samples are shown in the following. The number of counts under the Co $L\alpha$ or Mg $K\alpha$ emission is integrated during a given time and plotted as a function of the glancing angle i and is normalized to the current of a gold mesh inserted in the incident beam in order to correct for its intensity variations.

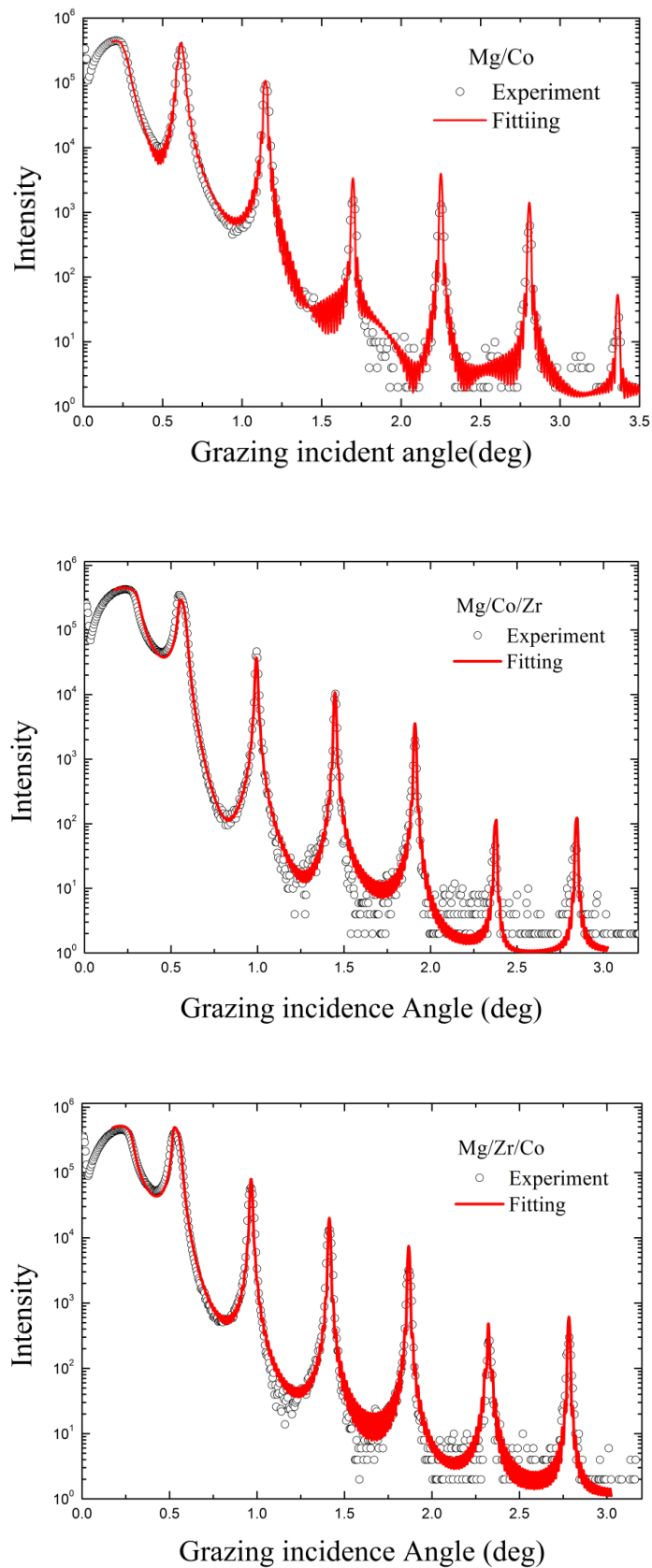
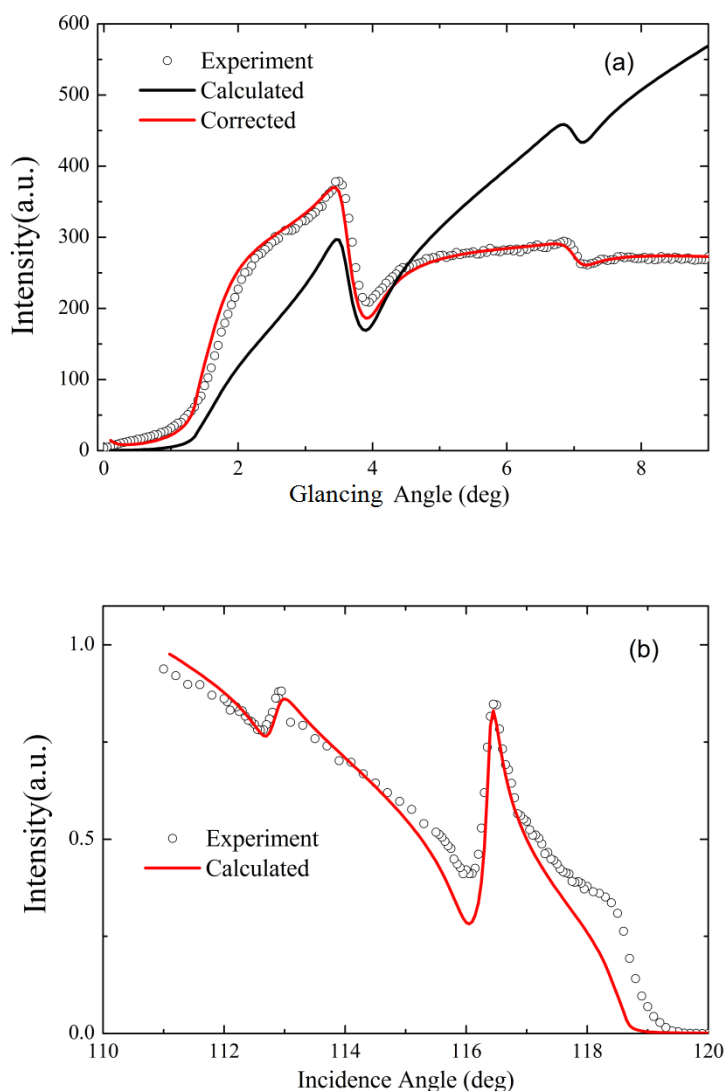


Figure 3.7 Measured (circles) and fitted (red line) XRR curves of Co/Mg, Mg/Co/Zr and Mg/Zr/Co samples.

1. Co/Mg

Figure 3.8 shows the XRF of Co/Mg multilayers as a function of glancing angle. A modulation of the intensity is clearly observed on each curve at an angle close to the one calculated from the Bragg law in the first and second diffraction orders. For the grazing incidence mode, the modulations correspond to the incident light and for the grazing exit mode, the emitted radiation. Based on the structure obtained from the XRR fitting results, the Mg $K\alpha$ and Co $L\alpha$ fluorescence yields are also calculated with and without the correction of the geometrical factor described in Ref [88]. Compared with the experimental data, it is clear that the geometrical factor has strong effects on the measured data in grazing incidence mode. For the grazing exit mode, no geometrical factor has been taken into account since this correction is generally significant only for the very small incident angles.



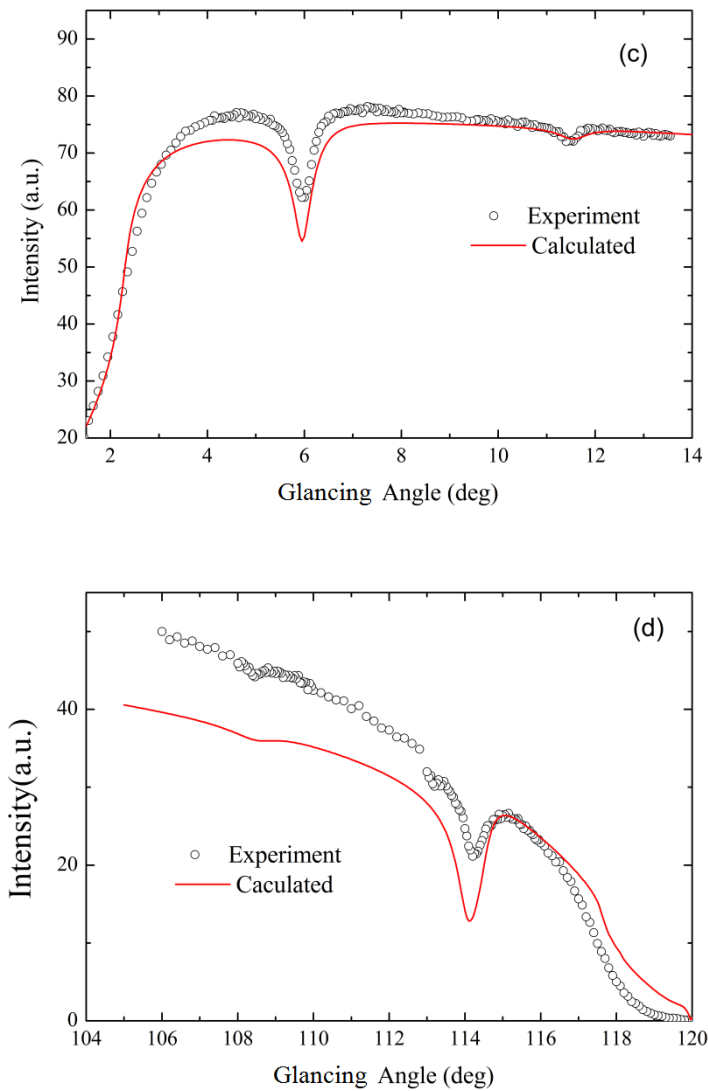


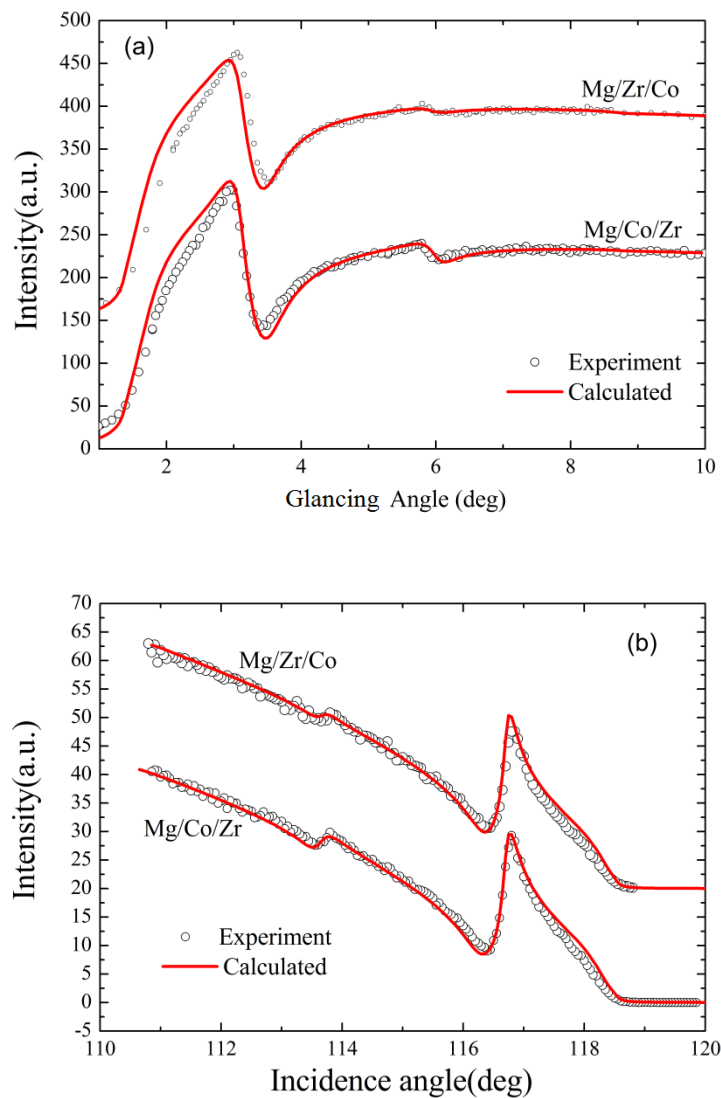
Figure 3.8 XRF curves of Mg/Co sample, experimental (circles) and calculated (solid line), obtained at 807.6 eV for the Co L α emission ((c) and (d)) and 1332 eV for the Mg K α emission ((a) and (b)). (a) and (c), (b) and (d) correspond to the grazing incidence mode and the grazing exit mode, respectively.

The calculated and experimental results fit well for the Mg K α emission except for a shoulder at 119 $^\circ$ for grazing exit mode which may be due to the oxidation of Mg layers close to the surface. This means the Co/Mg multilayers have sharp interfaces which is consistent with NMR results. The disagreement between experiment and theory of Co L α emission can be attributed mainly to the difference between the values of the tabulated optical indices. We note that there is a small energy difference, 1.7 eV, between the Co L α emission and the Co L3 absorption edge whereas there are about 50 eV between the Mg K α emission and the Mg K

absorption edge. Thus, in the Co case, the optical index is strongly varying in the region of the emission bandwidth, while it is almost constant in the case of Mg. The calculations are made with constant optical indices of the emitted radiation: this does not represent exactly the case of Co emission.

2. Mg/Co/Zr and Mg/Zr/Co

Figure 3.9 shows the XRF of Co/Mg multilayers with Zr barrier layers as a function of glancing angle. We observed the modulation of the fluorescence emissions in the standing wave mode for tri-layer systems when working in both angular ranges to diffract the incident radiation or the fluorescence emission. That is to say, fluorescence excited by standing wave can also be applied to tri-layer systems.



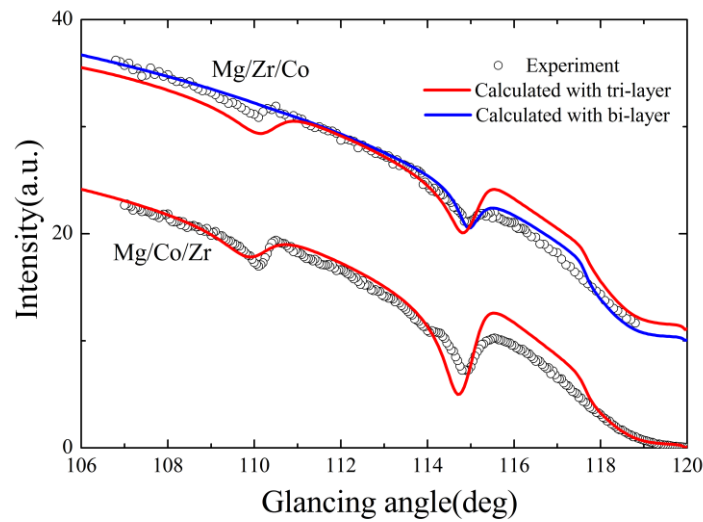
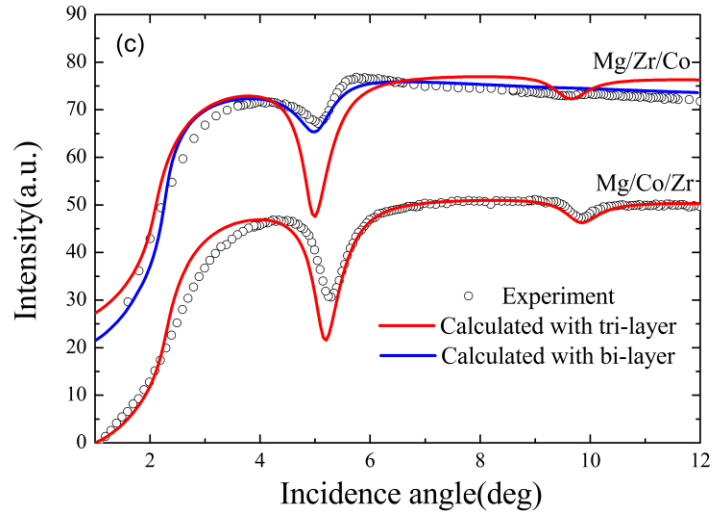


Figure 3.9 XRF curves of Mg/Co/Zr and Mg/Zr/Co samples, experimental (circles) and calculated (solid line), obtained at 807.6 eV for the Co $L\alpha$ emission ((c) and (d)) and 1332 eV for the Mg $K\alpha$ emission ((a) and (b)). (a) and (c), (b) and (d) correspond to the grazing incidence mode and the grazing exit mode, respectively.

The simulation of Mg $K\alpha$ emission of Mg/Co/Zr and Mg/Zr/Co multilayer agrees well with the fitting of XRR results. We can deduce that in Mg/Co/Zr and Mg/Zr/Co multilayers, the Mg-Zr and Co-Mg interfaces are sharp in agreement with the NMR results. For the Co $L\alpha$ emission, we can simulate the XRF curves of Mg/Co/Zr multilayer based in the parameters obtained from XRR, indicating that the Zr-on-Co interface is relatively sharp. Compared with the results of Mg/Co/Zr multilayer, the XRF curves of Mg/Zr/Co show lower amplitude at the

position of first and second diffraction orders. This indicates that the intermixing occurs at the Co-on-Zr interface. The simulation cannot fit well with the measurement with the tri-layer structure. Thus, we model Mg/Zr/Co as a Mg/Co_xZr_y bi-layer stack where x and y are the relative number of Co and Zr atoms, respectively. The values of x and y, estimated from the number of Co and Zr atoms within the Co and Zr layers in Mg/Zr/Co, are found equal to 0.78 and 0.22, respectively. This compound could be ascribed to Co₄Zr (Co₂₃Zr₆ in the literature present in the Zr–Co binary phase diagram) [89]. The comparison in Figure 3.9 (c) and (d) shows that the bi-layer model with the interface width of 0.6 nm gives a better fit to the experimental results than the tri-layer layer model.

Given the drastic differences between the XRF curves of Mg/Co/Zr and Mg/Zr/Co, we infer that the Zr-on-Co interface in Mg/Co/Zr is sharp. The distinctions between the two sets of samples on one hand Mg/Co and Mg/Co/Zr and on the other hand, Mg/Zr/Co and Mg/Zr/Co/Zr are in agreement with NMR results and with our recent studies [90]. In general, alternate interfaces in multilayer structure are asymmetric due to the difference in the surface free energy (γ) of the constituents of the multilayer. The difference in the structure of the two interfaces can be understood in terms of the difference in the surface free energies of Co (2.0 J m^{-2}) and Zr (1.6 J m^{-2}) [91]. During the deposition of Co on Zr, the surface free energy of Zr being lower, Zr atoms try to move to the surface guided by the chemical driving force. This would lead to a stronger mixing at the interface and a possible formation of Co₄Zr compound. On the other hand, during the deposition of Zr on Co, no such chemical driving force exists; therefore the intermixing at Zr-on-Co interface would take place as a result of random thermal motions only and hence concentration profile is expected to be an error function.

3.3.4 Conclusion

We have probed the interface quality through NMR and XRF induced by x-ray standing wave measurements. The Zr-on-Co interface is found quite sharp while a strong intermixing process is evidenced at Co-on-Zr interface and mixing layer exists with approximate composition of Co₄Zr. This difference in the structure of the two interfaces is the cause of different diffusivities at the two interfaces.

Chapter 4 Study the thermal stability of carbon-based multilayers

Carbon-based multilayers exhibit a high reflectivity near the carbon K-edge at 4.47 nm where the absorption of carbon is low. Co/C and Cr/C multilayers show high theoretical reflectivity [92] and state-of-the-art Cr/C [63] and Co/C [93] multilayers have near normal reflectance of about 18.7% and 14.8% respectively. In this chapter, we present the interfacial structure and thermal stability of carbon-based multilayers. Two systems Cr/C and Co/C are studied. In Section 4.1, we investigate thermal induced structural modifications of Cr/C multilayers. Section 4.2 presents the interface changes of Co/C multilayers upon annealing. Cr/C and Co/C multilayers show different changes at the interfaces upon annealing.

4.1 Structural changes induced by thermal annealing in Cr/C multilayers

4.1.1 Samples

Three sets of Cr/C multilayers whose period is about 5 nm are deposited by using DC magnetron sputtering with 30 bi-layers and thickness ratio (thickness of the carbon layer to the period, d_C/d) $\Gamma = 0.29, 0.51$ and 0.65 . To investigate their thermal behavior of Cr/C, all the samples are annealed at 600 °C for one hour in a furnace with a base pressure of 3×10^{-4} Pa. After annealing, the samples are cooled down to room temperature naturally.

4.1.2 Characterization of structure and interfaces

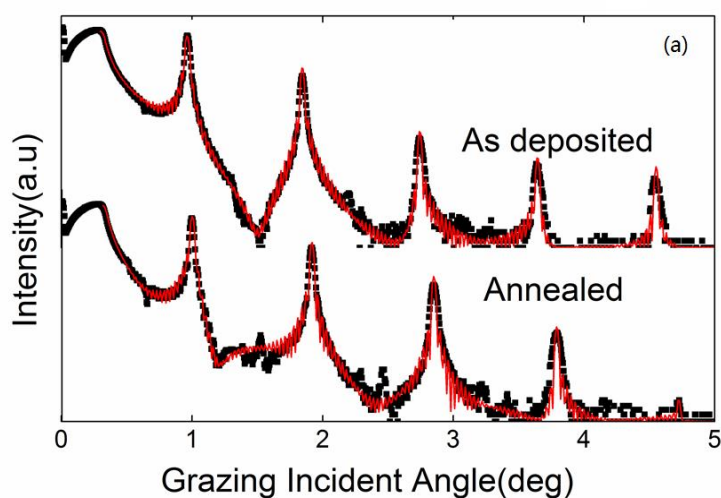
1. X-ray Reflectivity

XRR results are shown in Figure 4.1 as black dots. In Fig. 1(a), for the sample with carbon layer thickness ratio $\Gamma = 0.29$, upon annealing, the Bragg peaks shift to higher grazing incident angle which means that the period decreases. The intensity of 5th order peak (at 4.7 °) vanishes, suggesting that Γ changes to about 0.2. Figure 4.1(b) shows slight shift of the Bragg peaks before and after annealing for the sample whose carbon layer thickness ratio is $\Gamma = 0.51$. In Figure 4.1(c), contrary to that in Figure 4.1(a), the Bragg peaks of annealed sample shift to lower angle meaning that the period increases for the multilayer with $\Gamma = 0.65$. Before and after annealing, all three samples show sharp Bragg peaks, indicating slight changes in interface quality.

All the XRR curves are fitted to obtain the interlayer thickness, individual layer thickness and layer density. The fitted curves are plotted in Figure 4.1 as red thin lines. The fitted values are listed in Table 4.1. When Γ is smaller than 0.5, the period and carbon layer thicknesses decrease. When Γ is larger than 0.5, the opposite situation occurs after annealing. For all samples, the chromium layer thickness decreases and the interlayer thickness increases after annealing. The Cr-on-C interfacial layers are about 0.3 nm-thick for the as-deposited samples and increase to about 0.4 nm. The C-on-Cr interfacial layers grow from 0.6 nm to 0.9 nm after annealing.

Table 4.1 Parameters of the Cr/C multilayers deduced from fitting the GIXRR curves. The * lines correspond to the annealed samples.

Sample	Thickness(nm)					$\Gamma(d_C/d)$	Carbon density (g/cm ³)
	C	Cr	C-on-Cr	Cr-on-C	Period		
S1	1.4	2.49	0.31	0.66	4.86	0.29	2.01
S2	2.53	1.48	0.25	0.70	4.96	0.51	2.04
S3	3.02	0.8	0.29	0.62	4.73	0.64	2.01
S1*	0.97	2.29	0.44	0.98	4.68	0.21	1.73
S2*	2.49	1.25	0.41	0.89	5.04	0.49	1.82
S3*	3.22	0.73	0.36	0.71	5.02	0.65	1.76



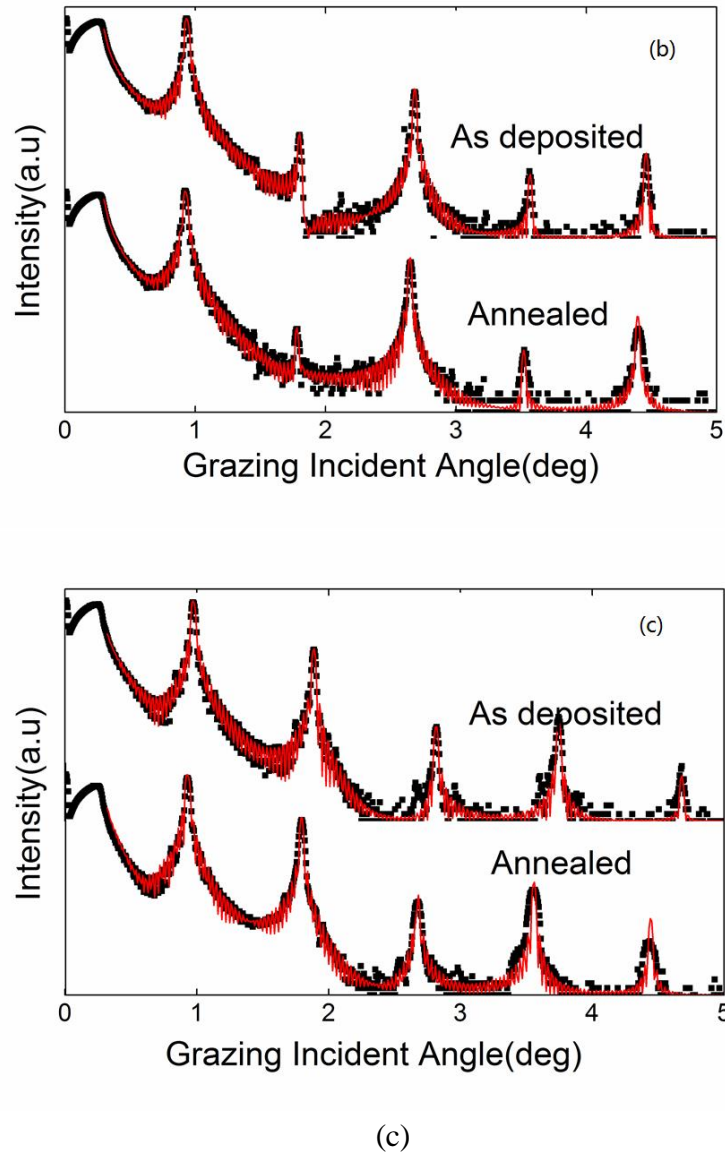


Figure 4.1 Measured XRR curves of as-deposited and annealed Cr/C multilayers with initial carbon thickness ratios of (a) $\Gamma=0.29$; (b) $\Gamma=0.51$; (c) $\Gamma=0.65$; dashed and solid lines represent measured and fitted XRR curves, respectively.

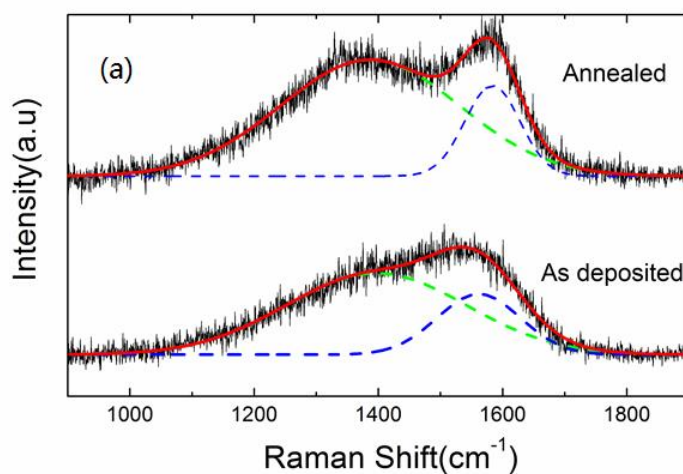
2. Raman spectroscopy

Figure 4.2 shows that the changes in the Raman spectra are similar for the three samples. Table 4.2 shows the variation of Gaussian fitted Raman parameters of G peaks position, FWHM of the G peaks and intensity ratio $I(D)/I(G)$ after annealing. It can be seen that the G band frequency increases towards 1580 cm^{-1} and the FWHM of the G peaks decreases. This means that the crystallites become more dominant upon annealing. The $I(D)/I(G)$ ratio

increases by 0.26 after annealing for all samples. The value of 1546 cm^{-1} for the G peaks position and 1.25 for $I(D)/I(G)$ suggest a sp^3 fraction of about 9-10%. By annealing, the intensity of G peaks increases with a corresponding increase in $I(D)/I(G)$ implying a decrease in sp^3 fraction to about 5-6%. The sp^3 fractions are calculated using three-stage model described by Ferrari *et al.* [94].

Table 4.2 Gaussian fitted Raman parameters of G peak position and intensity ratio $I(D)/I(G)$ before and after annealing. The * line corresponds to the annealed samples.

Sample	G Peak (cm-1)	FWHM of G peak(cm-1)	$I(D)/I(G)$
S1	1562	160	1.21
S1*	1579	104	1.47
S2	1554	166	1.24
S2*	1576	115	1.53
S3	1557	165	1.27
S3*	1574	113	1.54



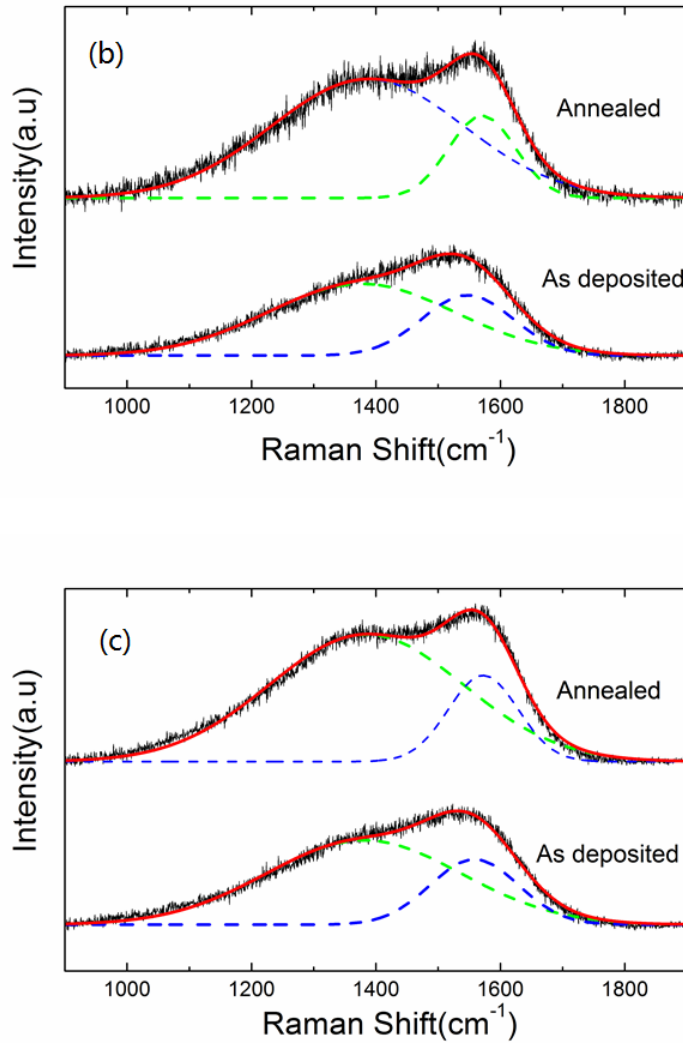


Figure 4.2 Measured Raman spectra decomposed in Gaussian lines of as-deposited and annealed Cr/C multilayers. Initial carbon ratio (a) $\Gamma=0.29$; (b) $\Gamma=0.51$; (c) $\Gamma=0.65$; Black lines are for the measured curves and red lines are for the fitted curves; Blue dotted and green dotted lines are for the fitted G peak and D peaks, respectively.

From the results of RS, we confirm the initial states of the amorphous carbon in Cr/C multilayers. After annealing at 600 °C, the further graphitization of the carbon layers can be observed. $I(D)/I(G)$ is related to the size of the graphite planes in the carbon films [95] and this has been used to analyze the thermal stability. [96] However, Cho et al. [97] have observed that when the value is larger than 1.1, the linear relationship between $I(D)/I(G)$ and the inverse of the microcrystalline size $1/L_a$ may no longer hold. They attribute the increase of

the I(D)/I(G) ratio to the increase of the number of graphite microcrystallites with defects. This also explains the increase in the intensity of D peak for most amorphous films after annealing at a higher temperature [98]. The D peak intensity usually increases after annealing above 300 °C and this phenomenon is generally due to the conversion of sp^3 bonds to sp^2 bonds and the change of the carbon structure to nanocrystalline graphite [96]. For our results, the intensity of the D peak increases after annealing and this shows that the structure of the carbon is at the beginning stage of the graphitization process. Full graphitization should be obtained over 2000 °C [99]. The sp^3 fraction in carbon layers decreases after annealing with the density of carbon changes linearly [94]. That is to say, the density of carbon should decrease and the thickness of the carbon layers should increase upon annealing. It is in agreement with the change of carbon layer thickness and density listed in Table 4.1 obtained from the fitting of XRR curves.

3. X-ray photoelectron spectroscopy

Figure 4.3 shows the high-resolution regional scans of as-deposited and annealed samples with $\Gamma=0.51$. The C 1s peak shape of both samples shows distinct regions which can be assigned to C–O (286.2 eV), C–C sp^2 (284.3 eV), sp^3 (285.3 eV) and C–Cr (283.2 eV) bondings. After annealing, the ratio of sp^3/sp^2 decreases from 0.11 to 0.06 implying the decrease in sp^3 fraction in carbon layers, which is consistent with the RS results. The C–Cr compound exists at the interfaces of both as-deposited and annealed Cr/C multilayers. Compared to the ratio of sp^2 , there is a transition to higher C–Cr bonding after annealing.

The XPS results indicate that the interfaces of Cr/C multilayer are mixture composed of carbon, chromium and C–Cr bondings. The annealing process causes increase of inter-diffusion and denser C–Cr compound forms at the interfaces. Thus the thickness of chromium layers decreases and the thickness of interlayers increases after annealing.

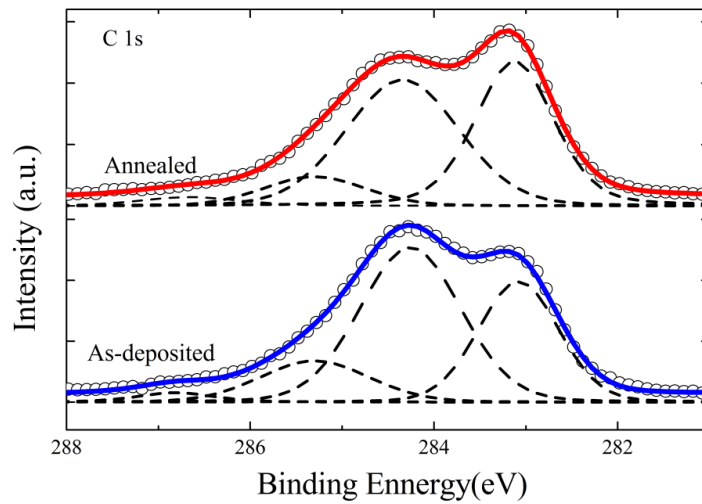


Figure 4.3 Carbon 1s peak XPS scan in for the samples with $\Gamma=0.51$.

When annealed up to 600 °C, the graphitization of carbon and the formation of compounds at the interfaces play simultaneously important role in the structure change of Cr/C multilayers. Based on the Miedema's macroscopic atom model [100], the mixing enthalpy of Cr-C system can be calculated, and the results are shown in Figure 4.4. It can be seen that the value of mixing enthalpy is negative at carbon concentration below 0.6 (mole ratio) and after increases sharply. That is to say, the mixing of Cr-C is easy when the carbon thickness ratio equals to 0.29 and 0.51 (carbon concentration equals to 0.34 and 0.56) thus the reduction of period caused by formation of carbide exceeds the expansion of residual carbon. When the carbon thickness ratio equals to 0.64 (carbon concentration equals to 0.7), the interface shows small possibility of Cr-C mixing and the graphitization carbon layers dominate the expansion of period. The calculated enthalpy of Cr-C mixing also shows that the most possible Cr-C compounds formed in multilayers is Cr_3C_2 because it has the largest negative value of enthalpy of formation (C concentration equals to 0.4). This is confirmed by Wilson et.al [101]. They have observed that the Cr-C sputtering coating had a Cr:C ratio of 3:2, suggesting Cr_3C_2 composition.

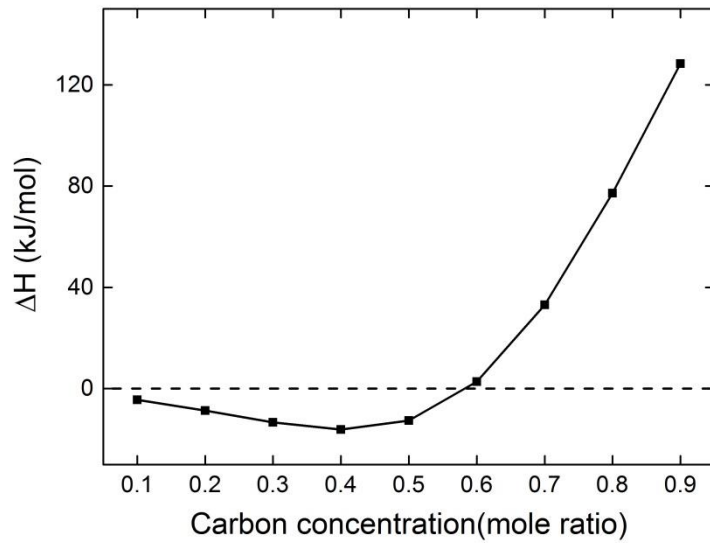


Figure 4.4 Calculated enthalpy of mixing for the Cr-C system.

By annealing, the intensity of XRR peaks does not decrease because the change of roughness and interface is small. However the structure change affects the performance of Cr/C multilayer seriously. For the sample that $\Gamma=0.29$, the period thickness decreases by 4% and for the one that $\Gamma=0.29$, increases by 6%. That means the peak wavelength will shift. Thus the better choice of Cr/C multilayers design is $\Gamma=0.5$ for EUV reflective mirrors and x-ray monochromators. The design of Cr/C multilayers based on theoretical analysis and computer optimization should also take the structural changes induced by heat into consideration.

4.2.3 Conclusion

Sputtering deposited Cr/C multilayers are investigated using XRR, RS and XPS. The samples are exposed to high heat load at the temperature of 600 °C. Thermal induced structural modifications are analyzed by fitting the XRR curves. The graphitization of the carbon could be observed in Cr/C multilayers by RS and the XPS results indicate that more chromium carbide formed at the interfaces. These are the two reasons why the Cr/C multilayers expand or contract with different carbon thickness ratios upon annealing.

4.2 Interface changes induced by thermal annealing in Co/C Multilayers

4.2.1 Samples

The Co/C multilayers are designed with bilayer number $N=20$, period thickness $\Lambda=4.1$ nm, and the thickness of Co layer, $d_{Co}=1.5$ nm. The multilayers are deposited by using DC magnetron sputtering method. To investigate the thermal behavior of Cr/C multilayers, the samples are mounted on a plate heated by a wire-wound furnace in a vacuum chamber with a base pressure of 3×10^{-4} Pa. The samples are heated from room temperature to 300 and 600 °C keeping for 1 hour.

4.2.2 Characterization of structure and interfaces

1. X-ray reflectivity

The XRR curves of the Co/C multilayers are presented in Figure 4.5. The fitted values are listed in Table 4.3. For the sample annealed at 300 °C, the Bragg peaks slightly shift to lower grazing incident angle than those of as-deposited sample. This means a slight increase of period thickness. When the sample is annealed at 600 °C, we observe an expansion of 17.5% in period thickness (from 4.09 nm to 4.81 nm).

The fitting results reveal that the carbon layer plays a crucial role in the period expansion. After 600 °C annealing, the thickness of C layer increases from 2.58 nm to 3.37 nm. This phenomenon is attributed to the graphitization of the amorphous carbon layers by annealing, which is confirmed by RS measurements in section 4.1. The thickness of Co layers decreases from 1.51 to 1.44 nm. This may be due to the demixing of Co and C atoms in the Co layers after annealing which will be mentioned below.

In Figure 4.5, three well-defined peaks are observed for the as-deposited and 300 °C annealed samples up to 3.5° . In the case of the 600 °C annealed sample, only first and second Bragg peaks are observed and the reflectance decreases. The intensity of Bragg peaks increases slightly after 300 °C, meaning that there is an interface smoothening effect in Co/C multilayers. The comparison of the reflectivity curves shows that after 600 °C annealing, the roughness of interfaces increases dramatically, from 0.4 nm to about 1.0 nm. The roughness deduced from the fitting of XRR (σ) is an overall imperfection of interfaces, including the

contributions from both geometrical roughness (σ_r) and interdiffusion (σ_d). Possible reasons for thermally induced roughness change in Co/C multilayers are investigated in the following.

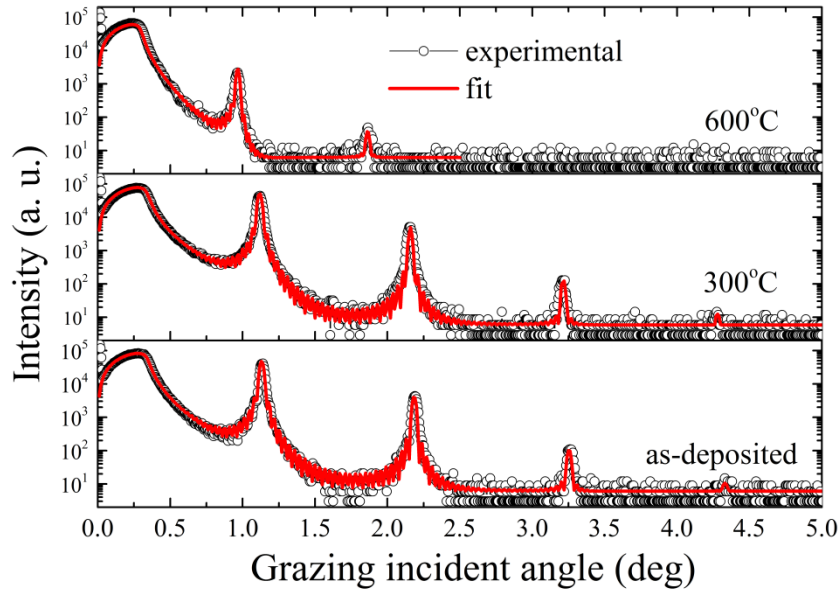


Figure 4.5 Measured (black circle) and fitted (red solid line) XRR curves of as-deposited and annealed Co/C multilayers.

Table 4.3 Parameters of the Co/C multilayers deduced from fitting of the XRR curves. (The density ratio is the fitted density divided by the density of the bulk.)

Sample	Period Λ (nm)	d_{Co} (nm)	d_C (nm)	σ_{Co} (nm)	σ_C (nm)	Density ratio: Co (%), C (%)
as-deposited	4.09	1.51	2.58	0.41	0.37	89 \pm 5, 93 \pm 5
300 °C annealing	4.14	1.53	2.61	0.40	0.35	91 \pm 5, 90 \pm 5
600 °C annealing	4.81	1.44	3.37	1.16	1.02	98 \pm 5, 80 \pm 5

2. Zero-field nuclear magnetic resonance spectroscopy

NMR spectra for the Co/C multilayers are presented in Figure 4.6. The spectrum of the Co/C as-deposited multilayer shows a weak signal without any defined feature in the frequency range of pure Co. This indicates that the Co layers are not pure but that alien carbon atoms are mixed with Co over the total Co layers. In addition some Co atoms are most probably also situated in non-ferromagnetic phases (and therefore give no NMR signal) with a large content of C. The as-deposited multilayers are actually CoC_x/C multilayer with probably

some concentration gradient at the interface with the C layers. The metal-containing layer is a Co-C alloy with the density of 6.2-6.5 g/cm³ lower than the density of massive Co and carbon enriched Co₂C layers [102]. As a result, Co/C multilayers consist of cobalt-carbon alloy and amorphous carbon layers.

The NMR spectrum of the Co/C 300 °C annealed sample also shows no defined peak, meaning that Co and C atoms are still strongly mixed in CoC_x layers. There is a broad structure at 110 MHz showing that some atomic motion occurred during annealing but the exact origin of this signal is difficult to identify. However, compared to the result of as-deposited samples, Co and C may have a tendency of demixing at a temperature of 300 °C. The demixing process between the Co and C atoms increases the x-ray optical contrast of the Co/C multilayers. That is why the X-ray reflectivity is improved at temperature of 300 °C.

The spectrum of the Co/C 600 °C annealed sample shows a well-defined peak at about 220 MHz which corresponds to bulk *hcp* like Co [72,73]. This means that pure Co regions appear and the diffusion decreases at the interfaces. We infer from these results that Co and C layers in the Co/C stack are strongly mixed during deposition and then demixing occurs upon annealing.

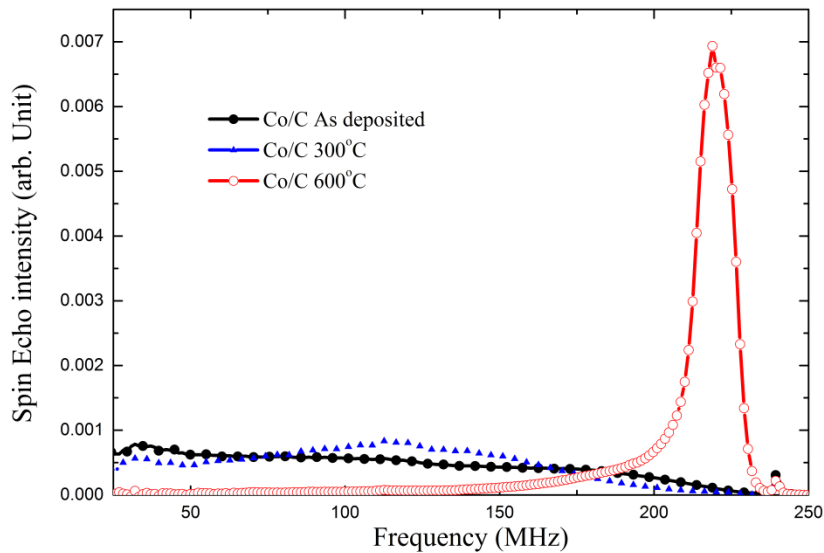


Figure 4.6 Zero-field NMR spectra of as-deposited and annealed Co/C multilayers.

Based on the Miedema's macroscopic atom model [100], the mixing enthalpy of Co-C system is calculated and the results are shown in Figure 4.7. It can be seen that the value of mixing enthalpy is positive at any carbon concentration. This indicates that the Co-C system

is easy to separate into two phases from the view of thermodynamics. This is in agreement with the NMR results. On the other hand, the carbon atoms separating out from CoC_x layers may be an additional reason for the expansion of carbon layers.

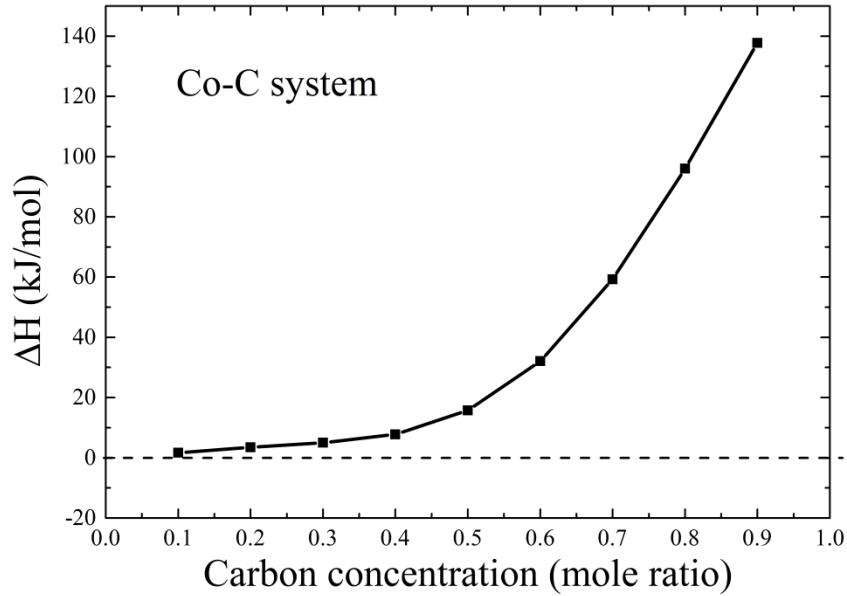


Figure 4.7 Calculated mixing enthalpy of the Co-C system.

3. X-ray diffuse scattering

The NMR results confirm the decrease of intermixing after annealing. Thus we attribute the deterioration of the interfaces to the increase of correlated morphological roughness. Therefore, X-ray diffuse scattering measurements are performed. Figure 4.8 shows the rocking curves measured around the first Bragg peak for the three samples. For the as-deposited and 300 °C annealed sample there is no significant change of the intensity except a slight shift of peak position. After annealed at 600 °C, a high intensity of diffuse scattered x-rays is observed, indicating significant increase of the correlated interfaces roughness.

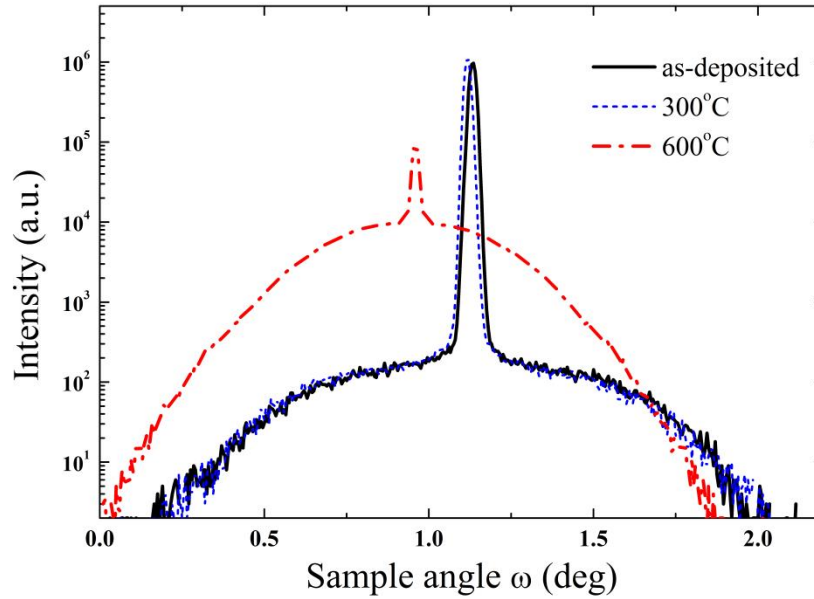


Figure 4.8 Rocking curves around the first Bragg peak of as-deposited and annealed Co/C multilayers.

4. X-ray diffraction

The x-ray diffraction patterns of Co/C as-deposited and annealed at 300 °C and 600 °C samples are presented in Figure 4.9. A broad peak can be observed around 44.5° around the *hcp* (002) [103] peak position for the sample annealed at 600 °C. Compared with the amorphous layers of as-deposited and 300 °C annealed sample, this peak indicates a significant structural change: the amount of crystallize Co increases upon annealing. This is in good agreement with NMR spectra. Co and C atoms may not separate completely because the XRD peak is weak and its width is much broader than reported for Co/Cu multilayers with 1.5 nm thick Co layers [104]. That is to say, the Co layers still contain a certain amount of C upon 600 °C annealing.

The reduction in reflectivity induced by interface roughness becomes more significant as the multilayer period thickness decreases, because the ratio of the interface roughness to the multilayer period thickness directly affects the reflectivity according to the Debye-Waller factor. Crystallization of metal layers in multilayers can cause an increase of geometrical roughness [19]. Crystallites can nucleate at some points during annealing. They have a size limited to the metal layer thickness in the growth direction and are also small in the in-plane

direction. The spatial distribution of crystallites in the metal layer is replicated as a modulation of the surface height. Since the metal layer becomes rougher, the nonmetal layer on top of the metal layer also becomes rougher. For the Co/C multilayers annealed up to 600 °C, the crystallization of Co layers increases the geometrical roughness and aggravates the overall imperfection of the interfaces.

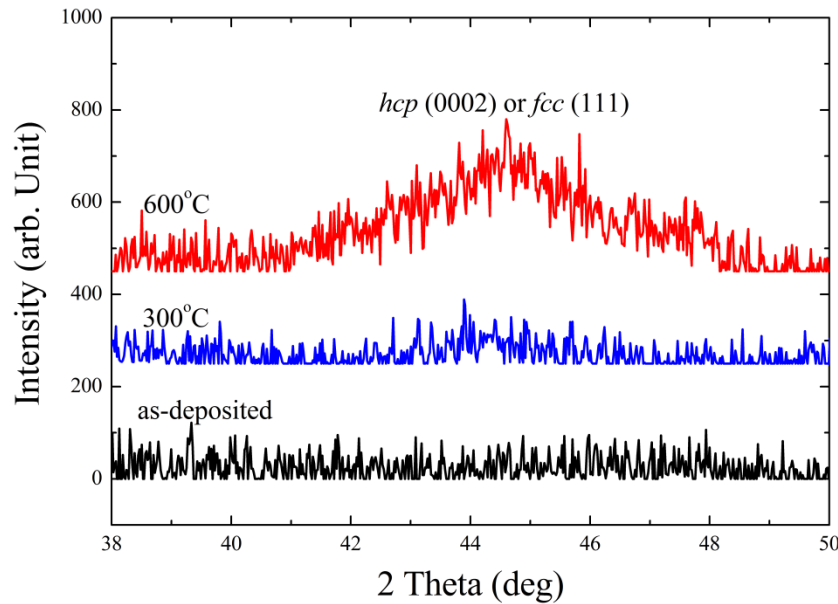


Figure 4.9 Diffraction patterns of as-deposited and annealed Co/C multilayers. The curves are shifted vertically for the sake of clarity.

4.2.3 Conclusion

Sputter-deposited Co/C multilayers annealed up to 600 °C are investigated by using XRR, XRD, XDS and NMR techniques. The multilayer is stable up to 300 °C and there is a slight increase in the period and reflectivity. We demonstrate through the NMR spectroscopy that the strong demixing between Co and C atoms occurs after annealing at 600 °C. This phenomenon is also demonstrated by the Miedema’s model which shows the phase separation of the Co-C system. The XDS and XRD results show that when the annealing temperature increases up to 600 °C, although the demixing of Co and C atoms increases the x-ray optical contrast of the Co/C multilayers, the formation of small Co crystalline grain causes the interfaces roughness. The demixing and graphitization of the amorphous carbon layers induce an expansion of period thickness.

Chapter 5 Improvement of Ti-based multilayers

5.1 Introduction

Multilayers for use in the so-called “water window” between the oxygen K-absorption edge at 2.34 nm (529.9 eV) and the carbon K-absorption edge at 4.38 nm (283.1 eV) have important applications for high-resolution microscopy [23, 25, 92], x-ray polarimetry [59] and spectrometry [51]. Many efforts are being put into realizing highly reflective multilayer mirror in this wavelength range. Ti-based multilayers are promising for application in this range close to Ti-2p absorption edge at $\lambda=2.74$ nm (452 eV). Cr/Ti and Co/Ti multilayers are two of the suitable candidates because their theoretical near-normal incidence reflectivity is as high as 64% at wavelengths just above 2.74 nm. However the reported experimental reflectivity of these multilayers at near-incidence angles is lower than 3%. According to the Debye-Waller term [105] in the reflectance, the performance of a multilayer is increasingly influenced by the interface imperfections with a decrease in wavelength and a corresponding decrease in period of multilayers. That is to say, the most important problem for the multilayer working at the range of “water window” is the extremely high sensitivity to interface imperfections. A possible solution for this problem is to prepare compound multilayers instead of elemental multilayers. Both the absorber and the spacer can be made of relatively stable compounds so that the tendency of interdiffusion and reaction at the interface can be minimized.

In recent years there has been a huge efforts to develop techniques that can reduce the interface width of multilayers. One recent attempt involved the intentional incorporation of light-element impurities such as N into multilayers. It has been shown that the incorporation of nitrogen in Cr/Sc or La/B₄C multilayers can form nonstoichiometric nitride multilayers with reduced interdiffusion or reaction between the layers and leads to major improvements in the x-ray reflectivity.

In this chapter, two interface engineering methods are used to improve the interfaces of Ti-based multilayers. In Section 5.2, Co/Ti multilayers are deposited by using reactive sputtering with N₂. Section 5.3 shows that boron and carbon are incorporated into Cr/Ti multilayers by depositing ultra-thin B₄C at the interfaces. The interfaces and soft x-ray

reflectivity of Ti-based multilayers are enhanced by interface engineering.

5.2 Co/Ti multilayers prepared by reactive sputtering

5.2.1 Samples

The Co/Ti multilayers are optimized for the highest reflectivity at 450 eV at 22.5° grazing incident angle. They are designed with bilayer number $N=20$, period $\Lambda=3.7$ nm, and thickness ratio $\Gamma=0.55$ (Ti layer thickness to period thickness, $\Gamma= d_{Ti}/d$). The calculated reflectance with ideal interface is 26.4%.

Argon gas at 1.5 mTorr is used for non-reactively sputtered films, while a small amount of N_2 (99.9995% purity) is added (maintaining the same 1.5 mTorr gas pressure) for reactively sputtered films. The N_2 gas fraction, defined as the N_2 gas flow rate (units of sccm) divided by the total Ar + N_2 gas flow rate, is respectively set to 5%, 10%, 15% and 20% for the reactively sputtered films.

5.2.2 Characterization of structure and interfaces

1. X-ray reflectivity

The grazing incident XRR curves of the Co/Ti multilayers are presented in Figure 5.1 (a). All the curves are fitted to obtain the interface width and thickness of individual layers. The fitted values are listed in Table 5.1. The reactively sputtered samples show three Bragg peaks while the non-reactively sputtered sample exhibits only two peaks and a relatively broader first peak than the reactively sputtered ones. That is to say that the interface width decreases remarkably by reactive sputtering (from about 0.8 nm to 0.3 nm from fitting).

Table 5.1 Parameters of the Co/Ti multilayers deduced from fitting of the XRR curves.

N_2 Fraction	Period Λ (nm)	d_{Co} (nm)	d_{Ti} (nm)	σ_{Co} (nm)	σ_{Ti} (nm)
0%	3.77	1.69	2.08	0.85	0.68
5%	3.74	1.61	2.12	0.31	0.28
10%	3.73	1.72	2.01	0.30	0.30
15%	3.81	1.74	2.07	0.32	0.33
20%	3.75	1.72	2.03	0.38	0.36

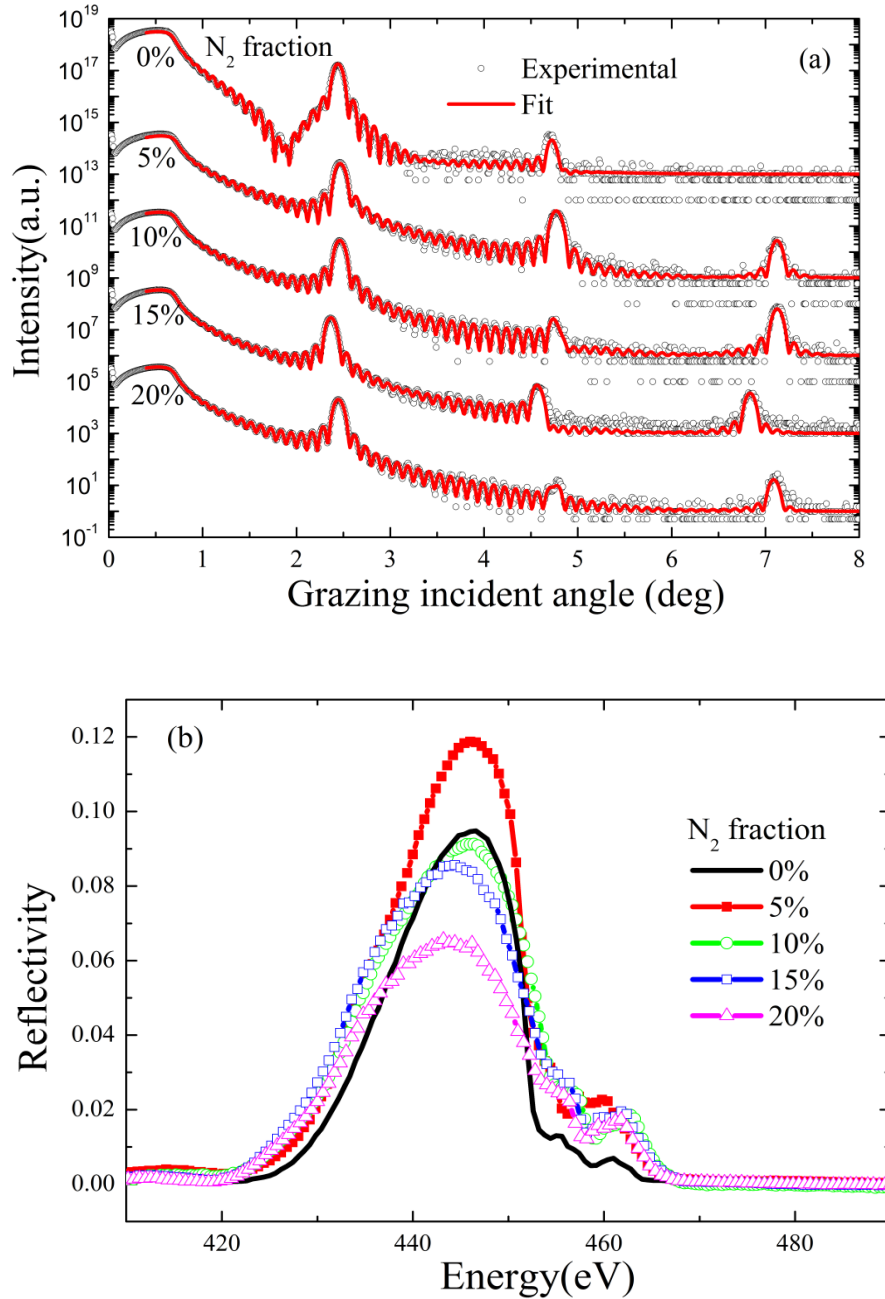


Figure 5.1 (a) Measured (black circle) and fitted (red solid line) XRR curves of Co/Ti multilayers. (b) Soft X-ray reflectivity of Co/Ti multilayers.

The measured curves of soft X-ray reflectivity as a function of the photon energy at 22.5° grazing incidence are shown in Figure 5.1 (b). The non-reactively sputtered multilayer has a peak reflectance of 9.5%. The sample deposited at 5% N₂ fraction shows the highest reflectance, 11.8% and then the reflectance decreases with the increase of N₂ fraction. The improvement of reflectivity is attributed to improved interfaces and reduced interdiffusion. According to the fitted values of XRR curves, the reactively sputtered samples have a similar

interface width. Thus the reduction of soft X-ray reflectivity for the samples which prepared with higher N₂ fraction may be due to the increase of concentration of nitrogen in multilayers. The absorption effect of nitrogen cannot be ignored at the applicable wavelength range of Co/Ti multilayers which is slightly lower than the nitrogen K edge (410 eV, 3.02 nm)

2. X-ray diffuse scattering

XDS measurement is performed to determine the change of correlated morphological roughness of interfaces. As shown in Figure 5.2, rocking curves around the first Bragg peak are measured for the non-reactively and reactively sputtered samples. Apart from a slight shift in the specular peak position due to variation of period, no other change is noticed on reactively sputtered samples. For clarity, we plot only results from the non-reactively sputtered sample and the sample deposited at 5% N₂ fraction. The FWHM of the specular peak for the non-reactively sample is larger than the one of the reactively sputtered one. This indicates reduction of interdiffusion at the interfaces by reactive sputtering. However, the diffuse signal around the specular peak does not decrease, which we interpret as negligible change in correlated roughness of interfaces with reactively sputtered samples.

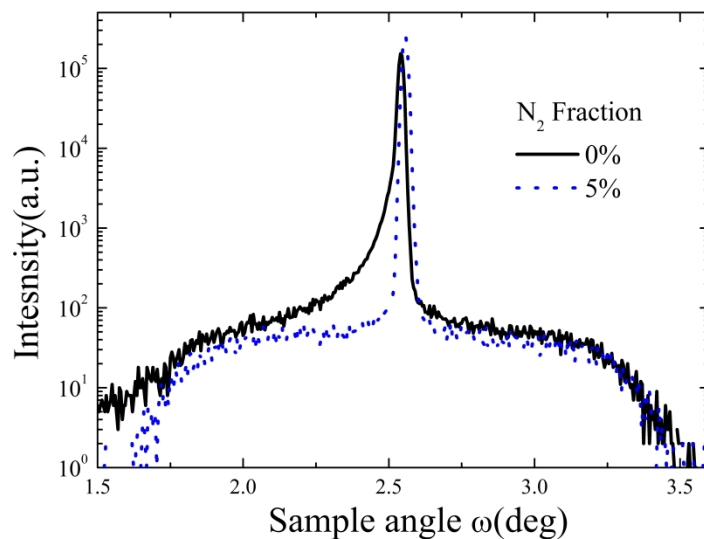


Figure 5.2 Rocking curves around the first Bragg peak of Co/Ti multilayers.

3. Zero-field nuclear magnetic resonance (NMR) spectroscopy

NMR spectra for the Co/Ti multilayers are presented in Figure 5.3. To compare the shape of the spectra, all the data are normalized to their total surface area. The spectrum of the non-reactively sputtered sample shows a weak signal without any defined feature in the frequency range of pure Co. This indicates that the Co layers are not pure and alien titanium atoms are mixed with Co over the total Co thickness. The as-deposited multilayers are actually CoTi_x/Ti multilayer with probably some concentration gradient at the interface with the Ti layers. In addition some Co atoms are most probably also situated into non-ferromagnetic phases (and therefore give no NMR signal) with a large content of Ti.

For the 5% N_2 fraction samples, an intense peak is observed around 217 MHz. This intense line at 217 MHz corresponds to bulk *fcc* or *hcp* Co according to the reference [72, 73]. This means the pure Co regions appear and the diffusion decreases at the interfaces. There is a satellite shoulder at 185 MHz showing that some Co atoms still mix with alien atoms (titanium or nitrogen) but the exact origin of this signal is difficult to identify because of the lack of appropriate reference samples. For the 10% N_2 fraction samples, the peak of Co decreases and its position shifts to lower frequency. This peak vanishes for the sample deposited at 15% N_2 fraction. The change of the bulk Co peak is consistent with the change of soft X-ray reflectivity which can be attributed to the increase in the concentration of nitrogen in Co layer and more nitrogen atoms mixed with Co. We did not plot the result of the sample deposited at 20% N_2 fraction because the signal is almost zero for all the frequency range. That means the Co atoms mixed with nitrogen atoms completely.

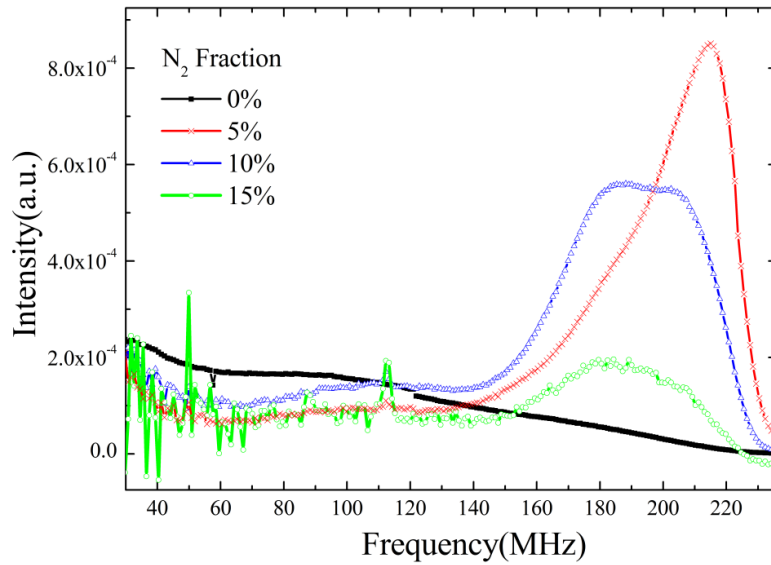


Figure 5.3 Zero-field NMR spectra of Co/Ti multilayers.

4. Transmission electron microscopy

Cross-section transmission electron microscopy (TEM) measurements are performed for the non-reactively sputtered sample and the reactively sputtered one with 5% N_2 fraction. The measured images are shown in Figure 5.4. The non-reactively sputtered multilayers form amorphous layers with rough interfaces. The reactively sputtered reactively sputtered sample shows better contrast and flatness, which is in agreement with the XRR result. Lattice fringes are clearly observed in the Ti-containing (bright) layers in the reactively sputtered film and such fringes are not evident in the non-reactively sputtered one. Figure 5.4 (b) shows that all Ti-containing layers are oriented with a common growth direction and a local epitaxy with neighboring Co-containing layers is frequently observed. Selected area electron diffraction (SAED) patterns show reflections of the Si substrate for both two samples. SAED pattern of reactively sputtered sample is characteristic of an *fcc* structure with the (200) plane and the average plane spacing is 0.22nm. TiN_x exists in *fcc* with the (200) nominal plane spacing is 0.221 nm. We infer that the reactively sputtered multilayer consists of under-stoichiometric *fcc* TiN_x layers. Although the distribution of N could not be determined, it can be expected that TiN_x will be closer to stoichiometric due to titanium high affinity for nitrogen. The TiN_x formation limits the diffusion between the Co and Ti layers.

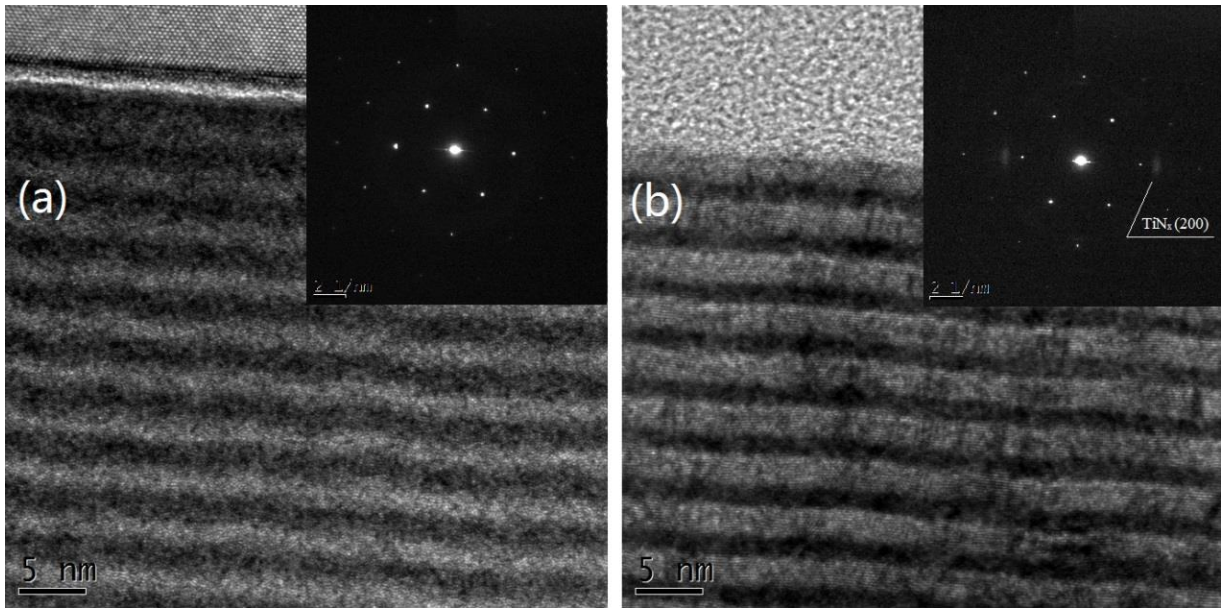


Figure 5.4 Cross-section TEM images and selected area electron diffraction patterns of Co/Ti multilayers (a) non-reactively sputtered (b) reactively sputtered.

5.2.3 Conclusion

Co/Ti multilayers are deposited by reactive magnetron sputtering with a nitrogen-argon gas mixture. The reactive sputtering has positive effects on the interfaces of Co/Ti multilayers, effectively forming crystalline *fcc* TiN_x multilayer structures. The reactively sputtered sample with 5% N_2 fraction exhibits 24% higher soft x-ray reflectance than the conventional Co/Ti multilayer. This is attributed to more abrupt interfaces and reduced interdiffusion by reactive sputtering. With the increase of N_2 fraction, the strong absorption of nitrogen in the applicable wavelength range causes a loss to the soft X-ray reflectivity. This is in consistent with the results of NMR. Thus, other light element such as boron or carbon is a better choice than nitrogen in the wavelengths of “water window”.

5.3 Cr/Ti multilayers prepared by co-deposition of B_4C

5.3.1 Samples

The Cr/Ti multilayers are deposited by DC magnetron sputtering with the B and C impurities incorporated by deposition of ultra-thin B_4C at the interfaces of the Cr/Ti multilayers. Firstly, we study the effect of the amount of incorporated B_4C and the choice of

interfaces at which B₄C is incorporated. Four series of Cr/Ti multilayers with period number $N=50$ are deposited. B₄C is incorporated at both Cr-on-Ti and Ti-on-Cr interfaces in the first series, at only Cr-on-Ti interfaces in the second series, and at only Ti-on-Cr interfaces in the third series. The multilayers in all three series are deposited with the same thicknesses of Cr layers and Ti layers ($d_{Ti}=d_{Cr}=0.7$ nm). Each of the three series consists of six multilayers with different amounts of B₄C. One multilayer had no B₄C incorporated and the nominal amounts (in thickness) of B₄C in the other five multilayers are 0.08, 0.13, 0.18, 0.22 and 0.27 nm, respectively. A fourth series containing four pure Cr/Ti multilayers without B₄C are also deposited for comparison. The period thicknesses of the four multilayers range from 1.4 nm to 1.7 nm and their thickness ratio ($\Gamma=d_{Ti}/\Lambda$) is ~ 0.5 .

5.3.2 Characterization of structure and interfaces

1. X-ray reflectivity

Only the first order Bragg peak could be observed for each multilayer because of the ultra-short period. We show the peak reflectivity as a function of the grazing incident angle in Figure 5.5(a), in which thicker multilayers appear toward the left (low angle) side. It can be seen from the figure that incorporating B₄C at either or both interface leads to higher reflectivity suggesting improved multilayer quality. More specifically, it is better to incorporate B₄C at the Cr-on-Ti interfaces than at the Ti-on-Cr interfaces, and best of all to do so at both interfaces. Another conclusion from Figure 5.5(a) is that 0.13 nm of B₄C is good enough for the interface quality improvement. The period thicknesses deduced from the peak angles are plotted as a function of the nominal B₄C thickness in Figure 5.5 (b). A linear relation between the period thickness and the nominal B₄C thickness is expected and observed as the deposition times of Cr or Ti are the same for each series. The slopes determined from linear fit are 1.15, 0.58, and 0.56 for the first, second, and third series, respectively. The value of the slope in the second and third series or half of the slope in the first series (because B₄C is deposited twice in a period in the first series) represents the ratio of the actual growth rate to the nominal B₄C deposition rate. The large disparity between this value and unity reveals that deposited B and C do not exist in B₄C form in the multilayers. We calculated this ratio

assuming that B_4C react with Cr using the formula $2B_4C + 7Cr \rightarrow 4CrB_2 + Cr_3C_2$ with all chemical species at their bulk densities. The result suggests that the ratio should be 0.73 if B_4C react with Cr. Similar calculations assuming that B_4C reacts with Ti according to the formula $B_4C + 3Ti \rightarrow 2TiB_2 + TiC$ suggest that the ratio should be 0.53, which is very close to the observed value. These results imply that the B and C incorporated into Cr/Ti multilayers are mainly bonded to Ti.

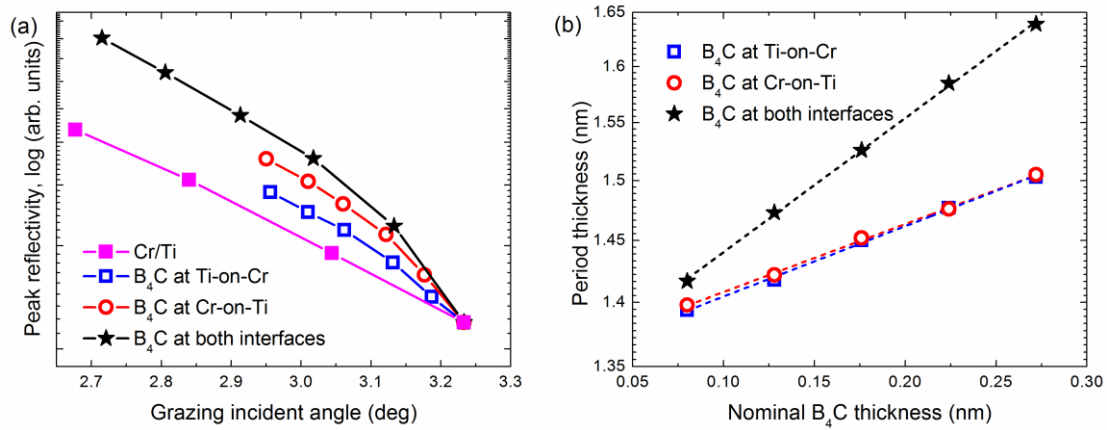


Figure 5.5 (a) Peak reflectivity versus peak angle of the first order Bragg peaks in the XRR curves of the Cr/Ti multilayers. Symbols represent the data and solid lines are only guide for the eye. (b) Period thickness versus nominal B_4C thickness of the Cr/Ti multilayers. Symbols represent the data and dashed lines the linear fit.

2. X-ray photoelectron spectroscopy

In order to study the interface stoichiometry, we use x-ray photoelectron spectroscopy (XPS) measurements on two samples. One had no B_4C incorporated and the other had 0.13 nm of B_4C at both interfaces. Atomic concentrations are calculated on the basis of Scofield's relative sensitivity factors. We can obtain the information of several-nanometer materials near the surface from the XPS spectra. Considering the ultra-short period, it is safe to regard the recorded spectra as averaged results over the whole multilayer period. The Cr $2p$ and Ti $2p$ spectra of the two multilayers show no difference in peak position, which is probably due to the small chemical shift of possible compound ($< 0.2eV$ for CrB_2 or TiB_2) [106]. The B $1s$ and C $1s$ spectra of the multilayer with B_4C are shown in Fig. 5.6 along with the spectra of a B_4C monolayer reference sample which is deposited and measured by the same method described

above. The B 1s spectrum of the monolayer consists of two peaks at 188.4 eV, characteristic of B–B or B–C bond from B atoms in the B₁₂ icosahedra, and 190.6 eV, characteristic of B–C bond from B atoms in the C–B–C chain. The B 1s spectrum of the Cr/Ti multilayer is dominated by a peak at 187.4 eV which is attributed to TiB₂ (187.5 eV) rather than CrB₂ (188.0 eV) [107]. The C 1s spectrum of the monolayer consists of two peaks at 282.8 eV, characteristic of B–C bond in the icosahedra, and 284.1 eV, characteristic of B–C bond in the C–B–C chain. The C 1s spectrum of the Cr/Ti multilayers is dominated by a peak at 281.9 eV which is attributed to TiC (281.7 eV) rather than Cr₃C₂ (282.9 eV) [108]. For the pure Cr/Ti multilayer, the atomic concentrations of Cr, Ti, and O are 58.9%, 27.8%, and 13.4%, respectively. The atomic ratio of Cr and Ti is about 2.1:1, which should be 1.5:1 as calculated using bulk densities and thickness ratio $\Gamma=0.5$. Thus there is ~17% excess of Cr in the multilayer compared to the design value. The excess Cr is probably located in the Ti layer because Cr can diffuse more easily into the less dense Ti layers than vice versa. Thus the pure Cr/Ti multilayer can be described as Cr/Cr_{0.37}Ti_{0.63}. For the Cr/Ti multilayer with B₄C, the atomic concentrations of Cr, Ti, B, C, and O are 47.8%, 22.9%, 17.1%, 4.4% and 7.9%, respectively. As described above, the B and C is mainly bonded to Ti, so that the Cr/Ti multilayer with B₄C can be described as Cr/TiB_xC_y ($x=0.75$ and $y=0.19$ for 0.13 nm of B₄C).

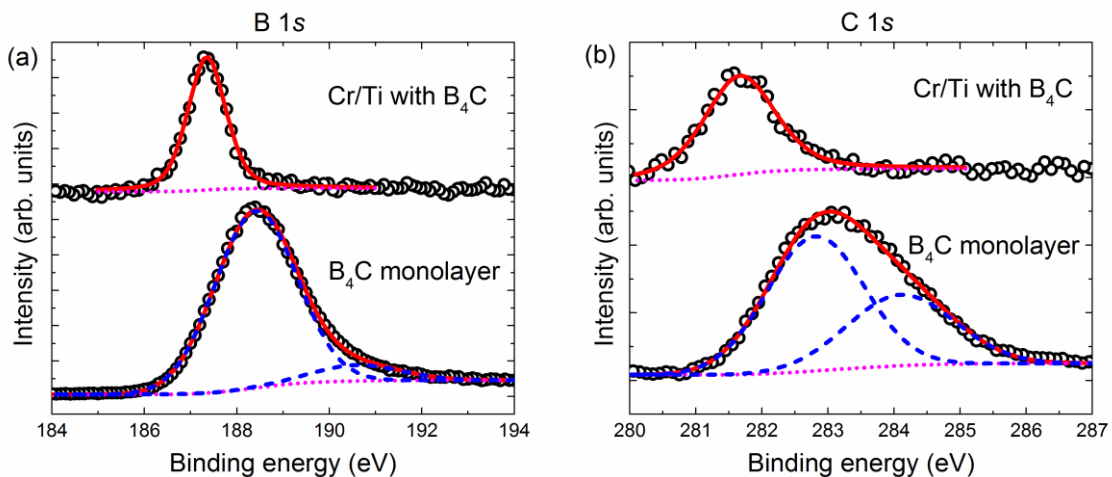


Figure 5.6 (a) B 1s and (b) C 1s XPS spectra of the B₄C monolayer and Cr/Ti multilayer with B₄C. Open symbols represent the measured data, solid lines the fitted spectra, short dashed lines the background, and long dashed lines the peaks used in the fitting if more than one peak is involved.

3. Transmission electron microscopy

Encouraged by the results above, two Cr/Ti multilayers, one without B₄C and the other with 0.13 nm of B₄C at both interfaces, with periodic number N=600 and period $\Lambda=1.38$ nm are deposited. They are designed as high reflection mirrors for wavelength $\lambda=2.73$ nm. Figure 5.7 shows the cross-section transmission electron microscopy (TEM) graphs for the two samples. The multilayer with B₄C shows much better contrast between the Cr and Ti layers although the flatness is similar, confirming that the TiB_xC_y formation prevents diffusion of Cr.

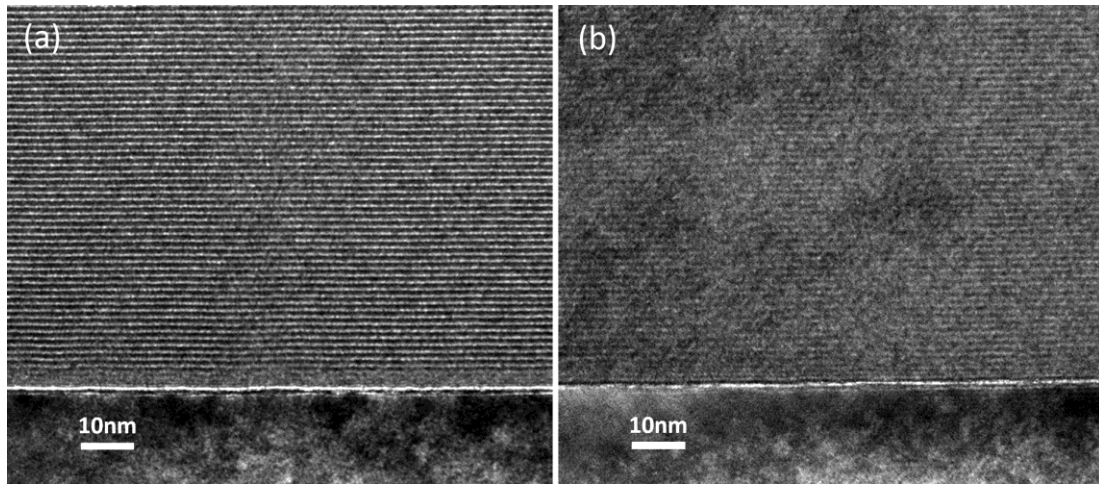
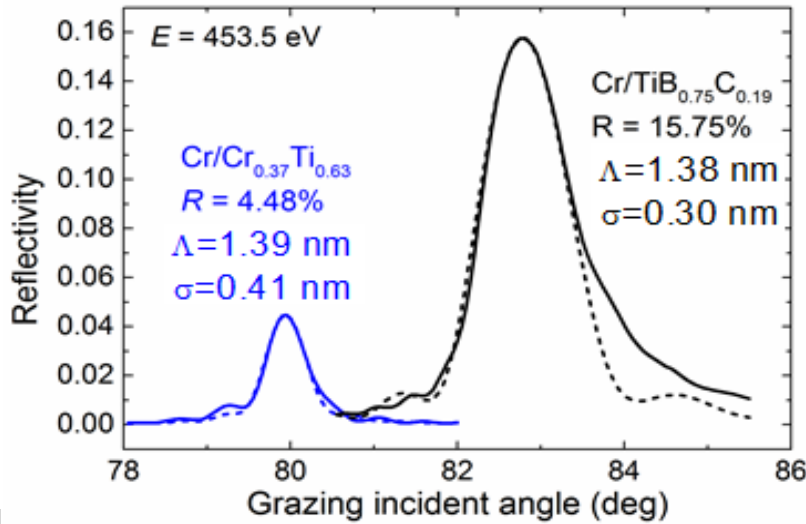


Figure 5.7 Cross-section TEM graphs of Cr/Ti multilayers (a) with and (b) without B₄C.

4. Soft x-ray reflectivity

For the measurement of soft x-ray reflectivity, a Cr filter is selected to suppress the high harmonic contamination from the collimated plane grating monochromator, and the linear horizontal polarization synchrotron radiation with energy at $E=453.5$ eV is used. The reflectivity is plotted in Figure 5.7 as a function of the incidence angle. The reflectivity of the pure Cr/Ti multilayer (Cr/Cr_{0.37}Ti_{0.63}) is $R=4.48\%$ (at 79.95°) and the interface width is determined to be $\sigma=0.41$ nm by simulation using the IMD code. The reflectivity of the Cr/Ti multilayer with B₄C (Cr/TiB_{0.75}C_{0.19}) is $R=15.75\%$ (at 82.75°) and the interface width is determined to be $\sigma=0.30$ nm. The required optical constants are generated following the method in the reference [109]. The used density of Cr_{0.37}Ti_{0.63} and TiB_{0.75}C_{0.19} are 5.27 and 4.59 g/cm³ which are calculated in accordance with the composition. The large improvement of the reflectivity is due to the reduced diffusion of Cr into the nonstoichiometric TiB_{0.75}C_{0.19} layer.



11

Figure 5.8 Soft x-ray reflectivity from the Cr/Ti multilayers with and without B₄C. Solid lines represent the measured data and dashed lines show the calculated reflectivities.

5.3.3 Conclusion

We have shown that pure Cr/Ti multilayers with ultra-short period ($\Lambda \sim 1.4$ nm) have an excess of Cr located in the Ti layers due to Cr diffusion. The multilayer can be described as Cr/Cr_{0.37}Ti_{0.63}. We intentionally incorporated B and C into Cr/Ti multilayers by depositing ultra-thin B₄C at the interfaces. It is found that incorporating 0.13 nm of B₄C at both interfaces dramatically affects the structure and composition of the Cr/Ti multilayers. The B and C incorporated during deposition is mainly bonded to Ti, forming Cr/TiB_{0.75}C_{0.19} multilayer structures. The formation of nonstoichiometric TiB_{0.75}C_{0.19} composition hinders the diffusion of Cr and improves the interface quality of Cr/TiB_{0.75}C_{0.19} multilayers. As a result, Cr/TiB_{0.75}C_{0.19} multilayers (with periodic number $N=600$) exhibit ~250% higher near-normal incidence soft x-ray reflectivity (absolute reflectivity $R=15.75\%$) than pure Cr/Ti multilayers.

Chapter 6 Study of Mo₂C/B₄C and Mo/B₄C multilayers

In this chapter, two systems Mo₂C/B₄C and Mo/B₄C are designed for working in the EUV range at near normal incidence. In Section 4.2, we investigate the optical and structural properties of both systems by combining the XRR, EUVR and TEM techniques. Section 4.3 presents the stress property for both systems.

6.1 Introduction

B₄C-based multilayers are widely used as reflective elements. In EUV range, multilayers for the spectral region near wavelength of 6.7 nm is of strong interest due to the development of next generation EUV lithography [3] and the x-ray spectrometry [50]. Boron-based multilayers are expected to perform well above the Boron K-edge at 6.6 nm. Boron target is difficult to sputter owing to its low conductivity and density. Good optical performance was obtained with multilayer that utilized boron carbide, such as Ru/B₄C, La/B₄C and Mo/B₄C. La/B₄C multilayers give the highest theoretical reflectivity of 60% but lanthanum is highly reactive. Interface engineering, such as nitrogen or carbon treatment should be used to improve the interface quality [110,111]. A near-normal incidence reflectivity of up to 58.6% has been measured for La/B₄C by using carbon as anti-diffusion barrier layer [110]. Mo/B₄C multilayers also promising for the wavelengths near 6.7-7nm because of its good thermal stability and it is easy to handle [112]. In x-ray range, B₄C-based multilayers are used as grazing incident monochromators in beamlines of synchrotron radiation and laboratory-based x-ray diffractometry and reflectometry [52]. Typical multilayer elements are based on materials such as W/B₄C, Ni/B₄C or Mo/B₄C, yielding a relative spectral resolution ($\Delta E/E$) of the order of a few percents and high reflectivity.

We choose to study Mo/B₄C multilayers base on the fine contrast of optical constant between Mo and B₄C, its good thermal stability and the sputtering target availability in our laboratory. Based on previous results, it appears that there are two main shortcomings of Mo/B₄C multilayers. On the one hand, Barthelmess et al. [112] have shown that the interfaces of Mo/B₄C-are far from perfect: amorphous molybdenum and boron carbide layers separated by molybdenum borides exist at the B₄C-on-Mo interfaces and the interlayer thickness grows

with increasing temperature. On the other hand, Mo/B₄C multilayers show high intrinsic stress [112, 116], which can cause undesirable distortion of the substrate figure and even lead to delamination of the coatings.

To improve the interface quality and stability of Mo-based multilayers, some authors have proposed to replace the Mo by Mo₂C, such as Mo₂C/Si [113] and Mo₂C/Be [114]. Choueikani et al. have studied the x-ray properties and interface of Mo/B₄C and Mo₂C/B₄C multilayers [115]. Mo₂C/B₄C multilayers show less interdiffusion and higher reflectance at 1500 eV than Mo/B₄C ones. However, in this study the thermal behavior and the performance in the EUV range are not considered.

There are some methods to reduce the stress of multilayers. For example, controlling the gas pressure [116,117], the post-deposition annealing [118,119] and varying the material ratio Γ [118,119] are commonly used techniques. However, these methods degrade the optical performance of multilayers. In this paper, we show a comparative study of interface properties and optical performance in the 6.7-7 nm range between Mo/B₄C and Mo₂C/B₄C multilayers. X-ray and EUV reflectivities are measured and then a qualitative observation and analysis of high-resolution cross-sectional TEM images are presented to study the structure and interfaces of the as-deposited and annealed multilayers. Before and after deposition, the radius of surface curvatures of substrates are measured using a stylus profiler and then the film stress can be calculated.

6.2 Optical and structural characterization of the Mo₂C/B₄C and Mo/B₄C multilayers

6.2.1 Samples

Following the multilayer design resulting from simulation, we prepare two sets of Mo₂C/B₄C and Mo/B₄C multilayers, whose parameters are given in Table 6.1. Mo₂C/B₄C_1 and Mo/B₄C_1 are optimized for the highest reflectivity at 6.7 nm at 10° near-normal incidence angle. In order to prevent oxidation, both multilayers are capped with a 3.5 nm thick B₄C layer. Mo₂C/B₄C_2 and Mo/B₄C_2 are prepared for TEM characterization. Cr adhesion layers are deposited between the Si substrate and the multilayer for all the samples.

To investigate the thermal behavior of these multilayers, all the samples are annealed at 600 °C for one hour in a furnace with a base pressure of 3×10^{-4} Pa. After annealing, the samples are cooled down to room temperature naturally.

Table 6.1 Designed structure of Mo₂C/B₄C and Mo/B₄C multilayers

Sample name	Period (nm)	Γ_{B_4C}	Simulated reflectivity	Number of periods	Experiments
Mo/B ₄ C_1	3.41	0.45	47.5% @ 6.7nm	200	XRR,EUVR
Mo ₂ C/B ₄ C_1					
Mo/B ₄ C_2	3.8	0.5	-	60	XRR,TEM
Mo ₂ C/B ₄ C_2					

6.2.2 Characterization of structure and interfaces

1. Mo/B₄C

The measured x-ray reflectance curves of Mo/B₄C_2 before and after annealing are shown in Figure 6.1 on a logarithmic scale. Four sharp Bragg peaks are observed in the as-deposited sample. The second and fourth peaks almost vanish as Γ is close to 0.5. In the annealed curves, the second peak becomes higher demonstrating the variation of Γ . All Bragg peaks become broader and slightly shift towards lower angles, which correspond to an expansion of period thickness and to an increase of interdiffusion.

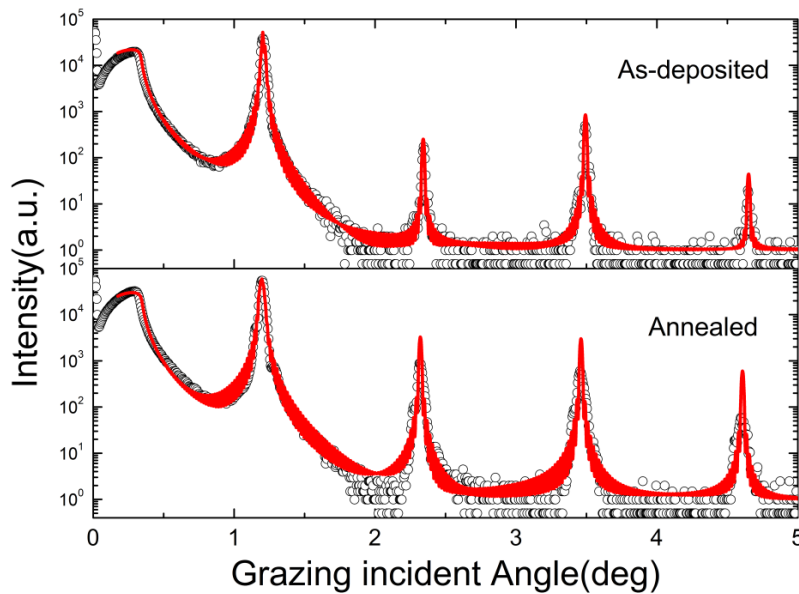


Figure 6.1 Measured (black dots) and fitted (red line) XRR curves of Mo/B₄C samples.

High-resolution TEM images are shown in Figure 6.2. The micrograph indicates that the Mo and B₄C layers are amorphous. Mo layers appear darker as they scatter more electrons than boron carbide layers. The Mo-on-B₄C interface is well defined while the B₄C-on-Mo interface is more diffuse. This behaviour is similar to what is observed at interfaces of Mg/SiC multilayer [120]. When Mo atoms are deposited onto B₄C layers, Mo hardly reacts with B₄C owing to the strong bonding in B₄C. When B and C atoms are deposited onto amorphous Mo layers, the true nature of the interface is a mixture of Mo compound and B₄C.

After annealing, the most noticeable change in the image is an increase in the thickness of the dark layers and a decrease in the thickness of the bright layers. This could be explained with the diffusion of carbon and boron into the molybdenum layers [121], which is agreement to the XRR curves.

We extract the in-depth intensity profile of multilayers along a few periods from the bright field image of each sample. The period thickness is determined by calculating the distance between two peaks. In order to minimize the aberration, we take the average value obtained over almost all the periods of stack. The thickness of one period is determined to be 3.76 nm and 3.81 nm corresponding to the as-deposited and annealed samples, respectively. To obtain the detailed information of each layer in one period and interface between layers, in-depth intensity profile of one period is magnified and shown in Figure 6.2 (c) and (d). All samples exhibit an asymmetric shape. For the as-deposited multilayer, the interface width of the B₄C-on-Mo is determined to be about 1 nm, much larger than that of Mo-on-B₄C interfaces, about 0.1-0.2 nm. After annealing, the interface width of the B₄C-on-Mo appears to decrease to about 0.6 nm. The real width of B₄C-on-Mo interface may be larger since the dark layers contain Mo and MoB_xC_y [121]. The interface width of Mo-on-B₄C has no obvious change upon annealing.

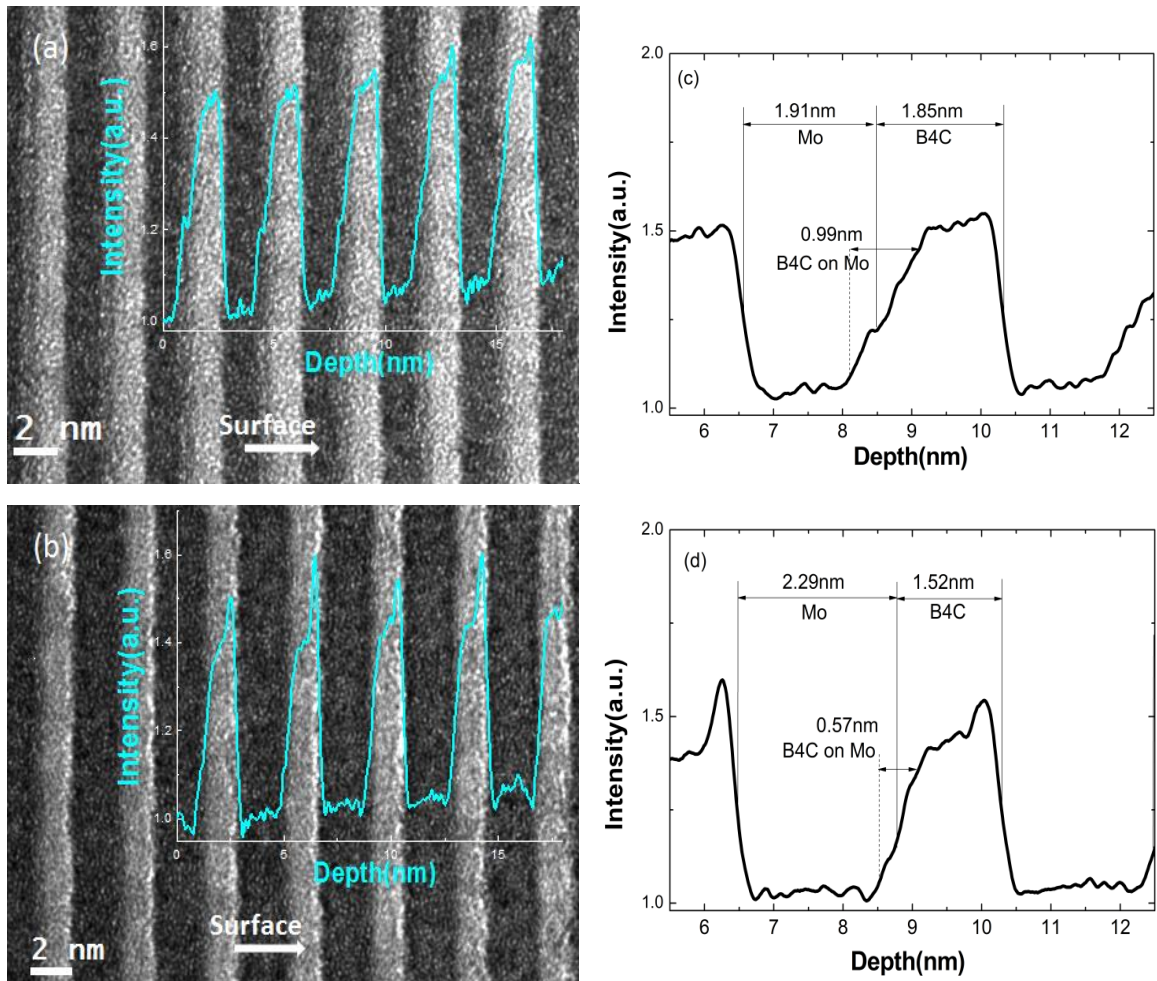


Figure 6.2. TEM cross-sectional images (a) and (b), and in-depth intensity profiles (c) and (d) of Mo/B₄C multilayers. (a) and (c), and (b) and (d) correspond to the as-deposited and 600 °C annealed samples respectively. The thickness of the layers and interfacial widths are indicated.

Choueikani et al. also observed the asymmetric interfaces in Mo/B₄C multilayers from TEM images and a three-layer model was used to fit the XRR results [115]. We fit the XRR curves by two-layer model with asymmetric interface width. The fitting data meet with the as-deposited sample (Fig. 1) but show higher and sharper peaks than the annealing one. This can be attributed to the uneven distribution of interdiffusion in the multilayers during the annealing process.

2. Mo₂C/B₄C

The X-ray reflectance curves of Mo₂C/B₄C_1 before and after annealing are shown in Figure 6.3. Compared with Mo/B₄C, the value of Γ and the width of the peaks have no obvious change upon 600 °C annealing, which indicate that the Mo₂C/B₄C multilayers show a

better thermal stability.

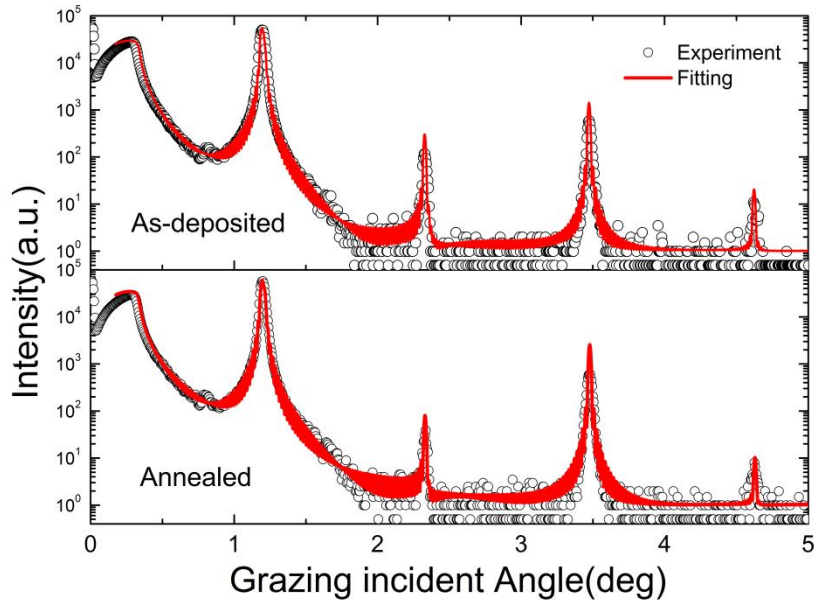
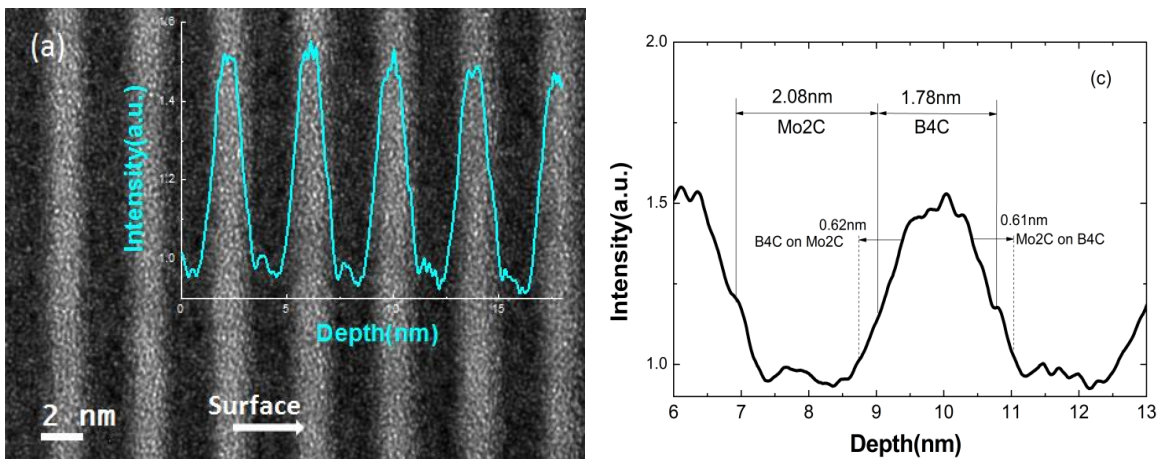


Figure 6.3 Measured (black dots) and fitted (red line) XRR curves of Mo₂C/B₄C samples.

HRTEM images are shown in Figure 6.4. The as-deposited sample has symmetric interfaces. Thus the two-layer model can be used to fit the XRR data of Mo₂C/B₄C as in Ref. [115]. Compared with Mo/B₄C multilayer, the interface of B₄C-on-Mo₂C is much smaller than the one of B₄C-on-Mo because the bonding in Mo₂C limits the formation Mo compound when boron and carbon atoms are deposited onto Mo₂C layer. After annealing, the micrograph shows a slight increase of the thickness of the dark layers which means there is still some diffusion of carbon and boron atoms into the molybdenum.



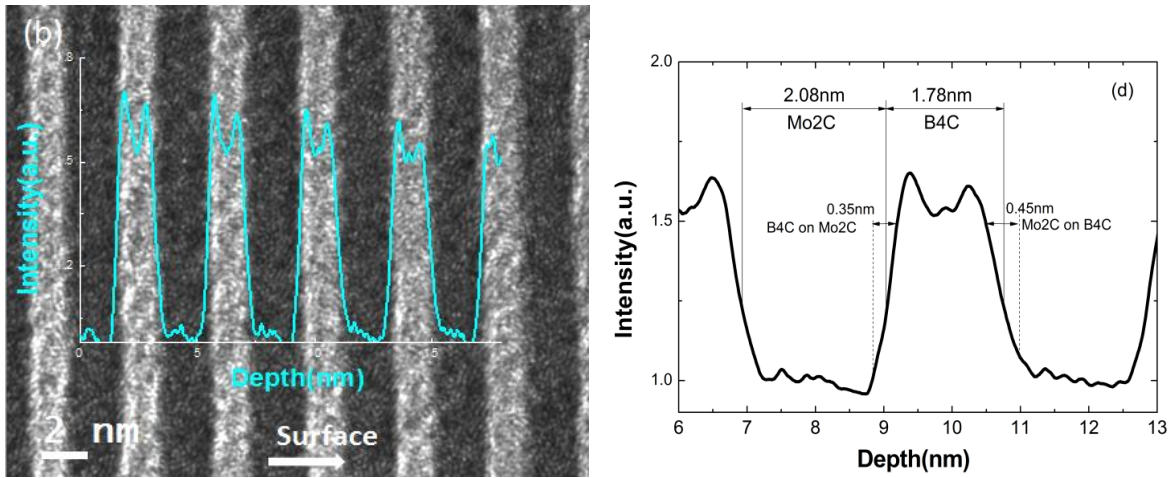


Figure 6.4 TEM cross-sectional images (a) and (b), and in-depth intensity profiles (c) and (d) of Mo₂C/B₄C multilayers. (a) and (c), and (b) and (d) correspond to the as-deposited and 600 °C annealed samples respectively. The thickness of one period layers and interfacial widths are indicated.

For the Mo₂C/B₄C as-deposited multilayer, the interface width of the B₄C-on-Mo₂C and Mo₂C-on-B₄C are determined to be about 0.6 nm. After annealing, the interface width decrease by about 0.2 nm. The Mo₂C/B₄C multilayers have little variation in the thickness of Mo₂C and B₄C layers. The interface width of B₄C-on-Mo₂C is slightly sharper than the one of Mo₂C-on-B₄C. The change of interface width is smaller than the one of Mo/B₄C. Owing to the bonding in Mo₂C, both interfaces of Mo₂C/B₄C are with limited diffusion and thus good chemically modulated Mo₂C/B₄C multilayers can be formed.

6.2.3 EUV reflectivity

The measured curves of the EUV reflectance as a function of the wavelength at 10° incidence are shown in Figure 6.5 as black dots. For Mo/B₄C multilayers, the as-deposited multilayers have a peak reflectance of 22.3%. Annealing to 600 °C reduces the reflectance to 17.5%. For Mo₂C/B₄C multilayer, the as-deposited multilayers have a peak reflectance of 28.5%. After annealing, the reflectance remains as high as 27.0%. Mo₂C/B₄C multilayers present not only a reflectivity higher than Mo/B₄C ones with same multilayer structure, but also a better thermal stability. This behavior coincided well with XRR and TEM

measurements.

The Mo₂C/B₄C system provides high reflectivity because of good symmetry of the optical index profile and small interface width. We fitted the EUV curves and the data of interface width are listed in Table 6.2 with the data obtained from the XRR and TEM. All the fitted curves show reasonable accordance with the measured ones.

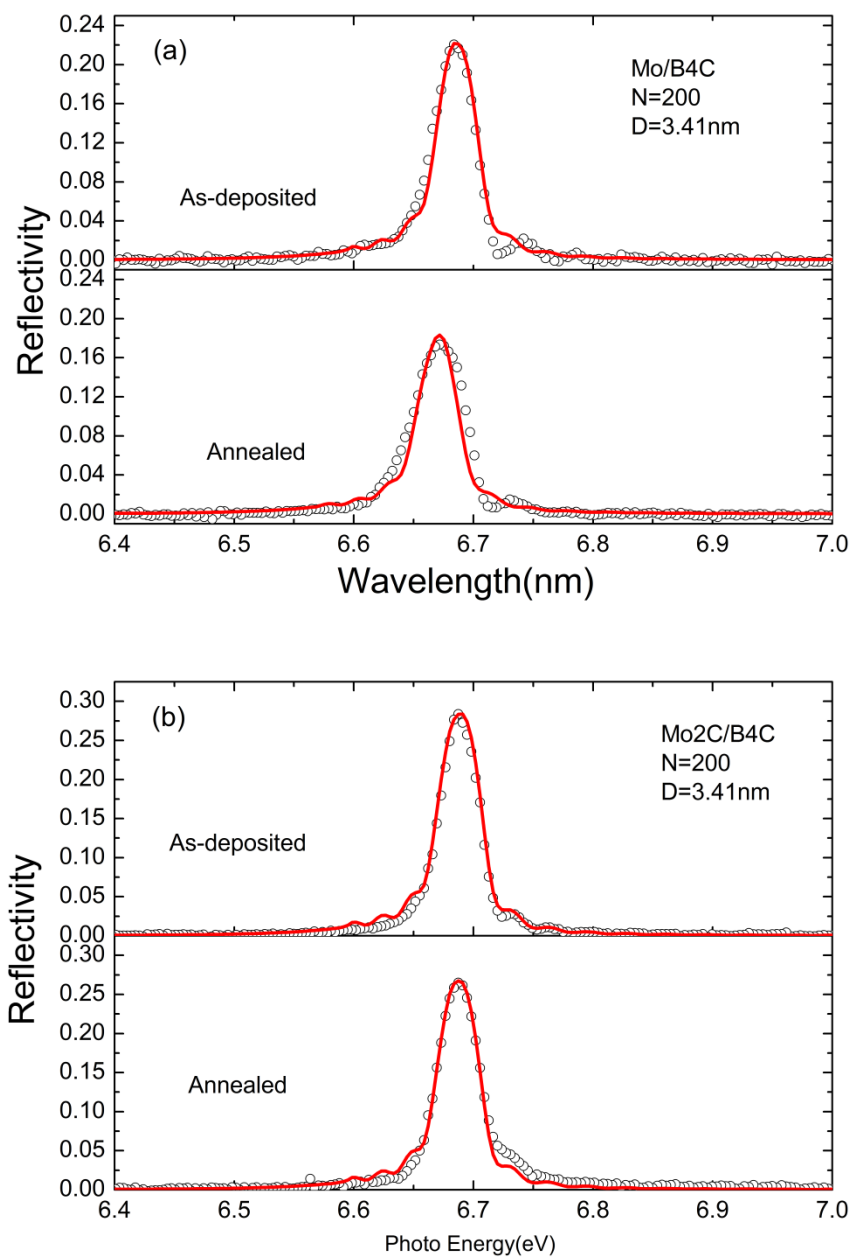


Figure 6.5 Measured (black dots) and fitted (red lines) EUV reflectance curves of (a) Mo/B₄C, (b) Mo₂C/B₄C multilayers.

Table 6.2 Interface widths of Mo/B₄C and Mo₂C/B₄C multilayers estimated from XRR, EUVR and TEM measurements.

Sample	Mo-on-B ₄ C interface (nm)			B ₄ C-on-Mo interface (nm)			
	XRR	TEM	EUVR	XRR	TEM	EUVR	
Mo/B ₄ C	As-deposited	0.21	0.22	0.32	0.67	0.99	0.92
	Annealed	0.24	0.19	0.36	0.81	0.57	1.23
Mo ₂ C/B ₄ C	As-deposited	0.21	0.61	0.56	0.23	0.62	0.54
	Annealed	0.19	0.45	0.61	0.22	0.35	0.58

The values of as-deposited samples derived from EUV curves are close to their respective TEM ones, which reveals that the interfaces of Mo/B₄C and Mo₂C/B₄C multilayer are dominated by interdiffusion. Actually, we have measured the X-ray diffuse scattering for all samples by rocking scan around the Bragg reflections. The scattered intensities are weak and show no obvious change after annealing. For both Mo/B₄C and Mo₂C/B₄C multilayers, the interface widths derived from XRR and EUV measurements share a similar feature: they increase after annealing. However, the interface width derived from TEM images decreases slightly. This can be due to an increase in the thickness of the diffused MoB_xC_y interlayers which show dark color after annealing.

6.2.4 Conclusion

We comparatively studied Mo₂C/B₄C and Mo/B₄C multilayers considered for normal incidence x-ray optics at 6.6-7 nm. The TEM images exhibit an asymmetry in the Mo/B₄C multilayer system with sharp Mo-on-B₄C interfaces and more diffuse B₄C-on-Mo interfaces. The Mo₂C/B₄C multilayers have thinner and more symmetrical interfaces because Mo₂C limits the reaction and diffusion of boron and carbon atoms with molybdenum ones. This makes the Mo₂C/B₄C multilayer more stable than Mo/B₄C up to 600 °C heat treatment. The EUV reflectivity peak at 6.7 nm measured is higher for Mo₂C/B₄C sample than for Mo/B₄C one. Smooth interfaces and excellent thermal stability make Mo₂C/B₄C multilayers a suitable alternative to Mo/B₄C for application in EUV and x-ray ranges.

6.3 Stress of the Mo₂C/B₄C and Mo/B₄C multilayers

Thin film stress can be mainly classified into two categories, thermal stress and intrinsic stress. Thermal stress originates from the different thermal expansion coefficients of thin films and substrates. Intrinsic stress is more complicated which is usually correlated to the growth process of thin film. Microstructure changes during growth, chemical reaction in the interfaces and bombardment of energetic particles and incorporation of impurities can all cause intrinsic stress. Here, we mainly concentrate on the intrinsic stress.

6.3.1 Experimental

The Mo, Mo₂C, B₄C mono-layer thin films and Mo₂C/B₄C, Mo/B₄C multilayers are all deposited by direct current (DC) magnetron sputtering technology on 0.12 mm-thick glass substrates in diameter of 30mm. The thicknesses of mono-layer thin films are all 30 nm. The period of multilayers is 3.5 nm with a thickness ratio of 0.5. The number of periods is 20. The thicknesses of mono-layer thin films and multilayers are characterized by XRR at 8 keV.

To measure the stress of different mono-layer thin films and multilayers, the radius of surface curvature of substrates are measured before and after deposition using a stylus profiler (Dektak 6M). To ensure the reliability of results, each sample is measured in two perpendicular directions repeatedly.

6.3.2 Results and discussion

Before deposition, the deformations of substrates are almost flat as shown in Figure 6.6 (a). After deposition, the substrates are bended due to the residual stress. All the deformed shapes are spherical as shown in Figure 6.7 (b). All the films show compressive stress as deduced from the observed curvature. The stress values of mono-layer thin films and multilayers can be calculated based on the measurement of the radius of surface curvature of substrates. The radius of curvature of substrates can be calculated using a geometrical relation:

$$R \approx d^2 / 8h \quad (5.1)$$

where d is the scan range of the stylus profile and h is the maximum height of the deformed

shape. Then, the stress σ_f can be expressed by the Stoney formula [122]:

$$\sigma_f = \frac{t_s^2 E_s}{6t_f(1-V_s)} \left(\frac{1}{R_o} - \frac{1}{R_1} \right) \quad (5.2)$$

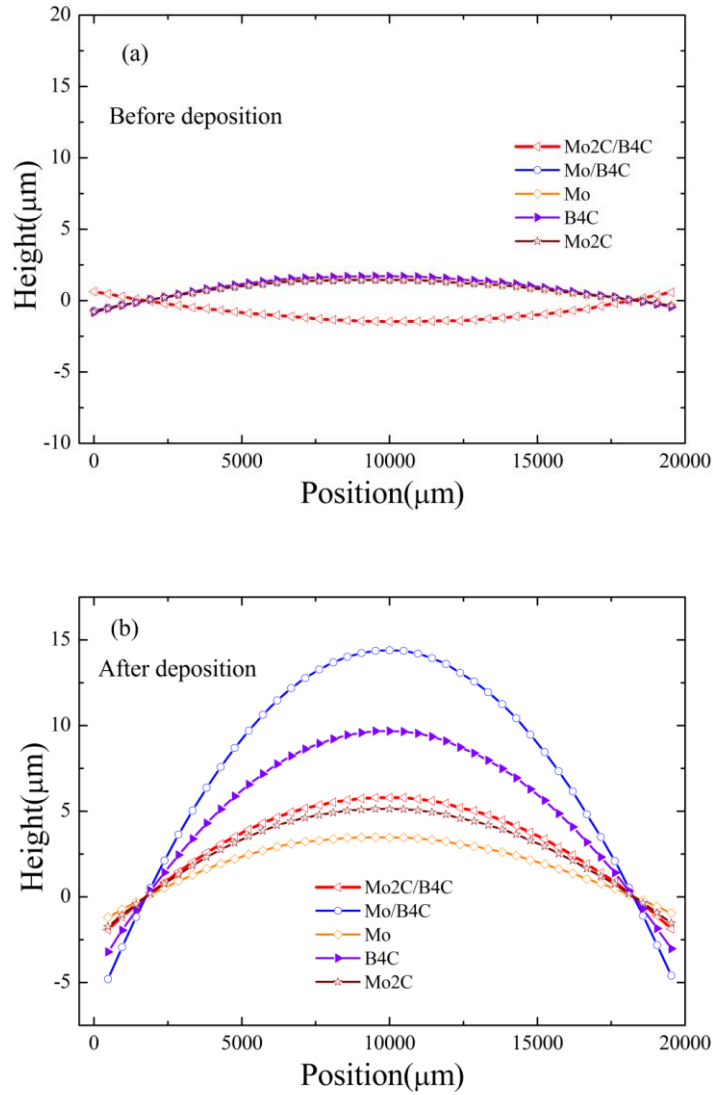


Figure 6.6 One dimensional surface profiles of substrates (a) before deposition and (b) after deposition.

where t_s is the thickness of the substrate and t_f is the thickness of the films. E_s and V_s are the Young's modulus and Poisson ratio of the substrate material. R_o and R_1 are the radius of radius of surface curvature of substrates before and after deposition. The values of stress for all samples are shown in Figure 6.7. The negative values represent compressive stress. The two columns of every sample represent the data in two perpendicular direction.

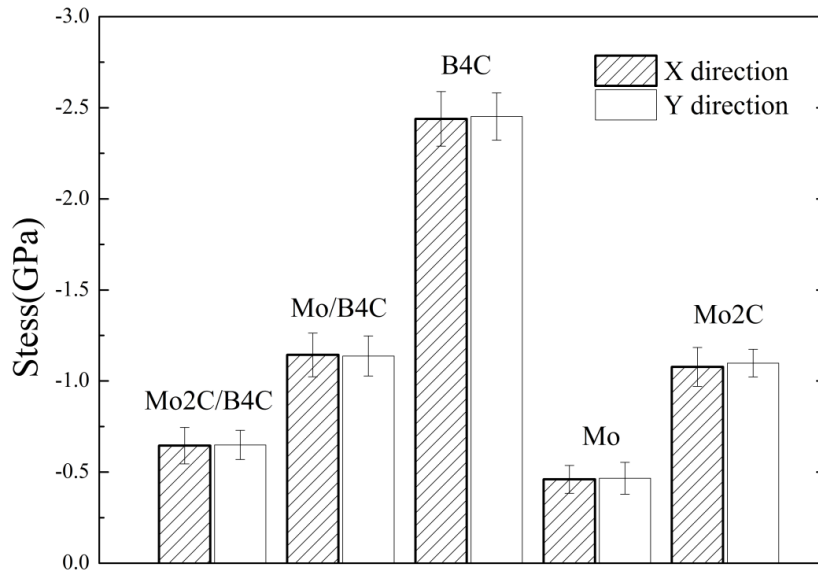


Figure 6.7 Comparison of stress for mono-layer films and multilayers.

The stress values of B₄C, Mo₂C and Mo layers are about -2.5, -1.0 and -0.5 GPa, respectively. The stress values of Mo₂C/B₄C and Mo/B₄C multilayers are about -0.6 and -1.1 GPa. That is to say, the intrinsic stress of Mo/B₄C multilayers is mitigated by replacing Mo by Mo₂C. There are two possible reasons for this phenomenon:

1) The interfaces of Mo/B₄C multilayers are more diffused than the ones of Mo₂C/B₄C. For diffused interfaces, the excess B and C atoms are incorporated into the position of Mo lattice or void and grain boundaries, causing local atomic displacements and densification of the films which results in the compressive stress of multilayers [123].

2) When the Mo or Mo₂C layers are at the state of initial growth, they may show tensile stress. For example, Mo layer initially grows in apparent tension until the thickness reaches 4 nm. This behavior is typical of the Volmer–Weber growth mode in which the film grows as isolated islands. As the islands coalesce, grain boundary cohesion induces, according to Hoffman, a tensile stress in the film [124]. That is why for Mo/Si multilayers, during the growth of Si on Mo, the stress evolves in compressive direction, whereas during the growth of Mo on Si, the stress evolution abruptly changes to tensile direction. The initial stress of Mo₂C layer may be higher than Mo, making the Mo₂C/B₄C multilayers show lower compressive stress than Mo/B₄C layer. However, the assumption should be verified by some precise *in situ* stress measurements.

6.3.3 Conclusion

To reduce the compressive stress in Mo/B₄C multilayers, a series of Mo, Mo₂C, B₄C mono-layer films and Mo/B₄C, Mo₂C/B₄C multilayers are deposited. The surface curvatures of substrates are measured before and after deposition to research the stress property. It is demonstrated that Mo, Mo₂C, B₄C mono-layer films show compressive stress while the compressive stress of Mo/B₄C multilayer is almost two times higher than the one of Mo₂C/B₄C. The sharper interfaces may be the reason why the Mo₂C/B₄C multilayers have lower compressive stress than Mo/B₄C. Thus the material combination of Mo₂C/B₄C is very suitable to deposit thick multilayer optics with a large number of layers for application in EUV and x-ray region.

Conclusions and perspectives

In this thesis we focus on the characterization of interfaces of multilayer monochromators. Several systems, such as Co/Mg, Co/Ti, Cr/Ti, Co/C, Cr/C and Mo/B₄C, have been studied by combining non-destructive and destructive measurements to investigate their interface properties and interface engineering methods to improve their interface quality. The observation of interface change of these systems upon annealing is important for improving their optical performance.

We firstly investigate the optical performance and interface properties of Co/Mg multilayers designed to work near the wavelength of 25-40 nm. The results show that Co/Mg can work up to 350 °C. From the XRD and XDS measurements, we infer that the degradation of Co/Mg multilayers in the annealing process is attributed to MgCo₂ formation. We perform NMR and fluorescence induced by soft x-ray standing wave to observe the asymmetrical behavior when introducing a Zr layer at one or at the other interface or at both interfaces of Co/Mg multilayers. The results show the sharp interface while a strong intermixing process is evidenced at Co-on-Zr interface.

We observe period expansion after annealing in both Cr/C and Co/C multilayers. This phenomenon is attributed to the graphitization of the amorphous carbon layers. Cr/C and Co/C multilayers show different change at the interfaces upon annealing. For Cr/C multilayers, X-ray photoelectron spectroscopy (XPS) results show that C-Cr compound exists at the interfaces and mostly forms upon annealing following the diffusion of Cr and C. On the contrary, for the Co/C multilayer, zero-field nuclear magnetron resonance (NMR) spectroscopy indicates that Co and C layers mixed during deposition and then Co and C atoms separated from their mixed region after annealing. The annealing process also causes an increase of geometrical roughness at interfaces, which is attributed to the crystallization of the Co layers.

We use two interface engineering methods to improve the interfaces of Ti-based multilayers. Co/Ti multilayers are deposited by using reactive sputtering with N₂ and Cr/Ti multilayers are deposited by incorporating ultra-thin B₄C at the interfaces. The reactively sputtered sample with 5% N₂ fraction exhibits 24% higher soft x-ray reflectance than the

Conclusions and perspectives

conventional Co/Ti multilayer. NMR measurements show that Co layers are not pure and alien titanium atoms are mixed with Co over the total Co thickness. The reactive sputtering has positive effects on the interfaces of Co/Ti multilayers, effectively forming crystalline *fcc* TiN_x multilayer structures, which reduce the interdiffusion of Co/Ti multilayers. From the XPS results, we conclude that The B and C incorporated during deposition is mainly bonded to Ti, forming nonstoichiometric TiB_{0.75}C_{0.19} composition hinders the diffusion of Cr and improves the interface quality of Cr/TiB_{0.75}C_{0.19} multilayers. As a result, Cr/TiB_{0.75}C_{0.19} multilayers (with periodic number N=600) exhibit ~250% higher near-normal incidence soft x-ray reflectivity (absolute reflectivity $R=15.75\%$) than pure Cr/Ti multilayers.

At last, we comparatively study the interface and stress properties of Mo₂C/B₄C and Mo/B₄C multilayers. The TEM images exhibit an asymmetry in the Mo/B₄C multilayer system with sharp Mo-on-B₄C interfaces and more diffuse B₄C-on-Mo interfaces. The Mo₂C/B₄C multilayers have thinner and more symmetrical interfaces because Mo₂C limits the reaction and diffusion of boron and carbon atoms with molybdenum ones. This makes the Mo₂C/B₄C multilayers have higher reflectivity and more stable than Mo/B₄C up to 600 °C heat treatment. The sharper interfaces may also be the reason why the Mo₂C/B₄C multilayers have lower compressive stress. Smooth interfaces, excellent thermal stability and stress property make Mo₂C/B₄C multilayers a suitable alternative to Mo/B₄C for application in EUV and x-ray ranges.

In this study, a model for analyzing the internal interfaces within the multilayer stack is developed by using fluorescence induced by XSW. The corresponding simulations of the depth distributions the specific atoms are presented. For Co-based multilayers, we perform NMR measurement to understand Co atoms behavior in the multilayer. Further experiments are needed to improve the analysis of these two powerful tools for analyzing the multilayers without damage. For fluorescence induced by XSW, a better agreement between experiment and simulation will be obtained by using correct optical indices and by taking into account the polarization effects, spatial intensity distribution of the beam and the instrumental geometry. In order to avoid or minimize the problem coming from the variation of the optical indices as a function of the incident energy, it would be better to work with a characteristic emission whose energy is far from the energy of the involved core level. For Co-based multilayers, in

Conclusions and perspectives

order to identify the Co_xX_y (X is the element of Co/X multilayers) compounds at the interfaces, some reference Co_xX_y disordered alloys and Co/X thin layer with different thickness of X layers when thickness of Co layers are fixed should be prepared and NMR, XES and XPS used to improve the analysis of the Co-based system.

Reference

1. Brewer C A, Brizuela F, Wachulak P, et al. Single-shot extreme ultraviolet laser imaging of nanostructures with wavelength resolution. *Opt. Lett*, 2008, 33(5): 518-520.
2. Chao W, Harteneck B D, Liddle J A, Anderson E H, Attwood, D T, Soft X-ray microscopy at a spatial resolution better than 15 nm. *Nature*, 2005, 435(7046): 1210-1213.
3. Wagner C, Harned N. EUV lithography: Lithography gets extreme. *Nature Photonics*, 2010, 4(1): 24-26.
4. Winter B, Weber R, Hertel I V, et al. Electron binding energies of aqueous alkali and halide ions: EUV photoelectron spectroscopy of liquid solutions and combined ab initio and molecular dynamics calculations. *Journal of the American Chemical Society*, 2005, 127(19): 7203-7214.
5. Bowyer S, Drake J J, Vennes S. Extreme ultraviolet astronomy. *Annu Rev Astron Astr*, 2000, 38(1): 231-288.
6. Lampton M, Margon B, Bowyer S. Parameter estimation in X-ray astronomy. *The Astrophysical Journal*, 1976, 208: 177-190.
7. Key M, Barbee Jr T, Da Silva L, et al. New plasma diagnostic possibilities from radiography with xuv lasers. *Journal of Quantitative Spectroscopy and Radiative Transfer*, 1995, 54(1): 221-226.
8. Dwivedi B. EUV spectroscopy as a plasma diagnostic. *Space science reviews*, 1993, 65(3-4): 289-316.
9. Kirkpatrick P, Baez A V. Formation of optical images by x-rays. *J Opt Soc Am*, 1948, 38(9): 766-773.
10. Chase R C, VanSpeybroeck L P. Wolter-Schwarzschild telescopes for x-ray astronomy. *Appl Opt*. 1973, 12(5): 1042-1044.
11. Meekins J F. Diffraction pattern of self-supporting transmission gratings. *Appl Opt*, 1989, 28(6): 1221-1227.
12. Barbee Jr T W, Mrowka S, Hettrick M C. Molybdenum-silicon multilayer mirrors for the extreme ultraviolet. *Appl Opt*, 1985, 24(6): 883-886.
13. Jonnard P, Le Guen K, André J M. High - resolution x - ray analysis with multilayer

Reference

- gratings. *X-Ray Spectrometry*, 2009, 38(2): 117-120.
14. André J M., Benbalagh R, Barchewitz R, et al. X-ray multilayer monochromator with enhanced performance. *Appl Opt.* 2002, 41(1): 239-244.
 15. Underwood J H, Barbee Jr T W. Layered synthetic microstructures as Bragg diffractors for X rays and extreme ultraviolet: theory and predicted performance. *App Opt.* 1981, 20(17): 3027-3034.
 16. Vinogradov A, Zeldovich B Y. X-ray and far uv multilayer mirrors: principles and possibilities. *Appl Opt*, 1977, 16(1): 89-93
 17. Spiller E. Reflective multilayer coatings for the far UV region. *Appl Opt.* 1976, 15(10): 2333-2338.
 18. Windt D L. IMD—Software for modeling the optical properties of multilayer films. *Comput Phys*, 1998, 12: 360.
 19. Bajt S, Stearns D G, and Kearney P. A, Investigation of the amorphous-to-crystalline transition in Mo/Si multilayers. *J. Appl. Phys.* 2001, 90(2): 1017–1025.
 20. Yulin S, Feigl T, Kuhlmann T, Kaiser N, et.al. Interlayer transition zones in Mo/Si superlattices. *J. Appl. Phys.* 2002, 92(3):1216–1220.
 21. Yulin S, Benoit N, Feigl T, et al. Interface-engineered EUV multilayer mirrors. *Microelectron Eng*, 2006, 83(4): 692-694.
 22. Clift W M, Folta J A, Alameda J B, et al. Improved reflectance and stability of Mo-Si multilayers. *Opt. Eng.*, 2002, 41(8): 1797-1804.
 23. Ghafoor N, Eriksson F, Gullikson E, et al. Incorporation of nitrogen in Cr/Sc multilayers giving improved soft x-ray reflectivity. *Appl Phys Lett.* 2008, 92(9): 091913-3.
 24. Windt D L. Reduction of stress and roughness by reactive sputtering in W/B4C multilayer films. *Proc. SPIE* 6688, 2007: 66880R.
 25. Bellotti J A, Windt D L. Depth-graded Co/C multilayers prepared by reactive sputtering. *Proc. SPIE* 7437, 2009: 743715.
 26. Eriksson F, Ghafoor N, Schäfers F, et al. Atomic scale interface engineering by modulated ion-assisted deposition applied to soft x-ray multilayer optics. *Appl Opt*, 2008, 47(23): 4196-4204.
 27. Ghafoor N, Eriksson F, Persson P O, et al. Effects of ion-assisted growth on the layer

Reference

- definition in Cr/Sc multilayers. *Thin Solid Films*, 2008, 516(6): 982-990.
28. Ziegler E. Multilayers for high heat load synchrotron applications. *Opt Eng.* 1995, 34(2): 445-452.
 29. Ziegler E, Lepetre Y, Schuller I K, et al. Stability of multilayers for synchrotron optics. *Appl Phys Lett.* 1986, 48(20): 1354-1356.
 30. Mitsuda K, Kelley R L, Boyce K R, et al. The high-resolution x-ray microcalorimeter spectrometer system for the SXS on ASTRO-H. *Proc. SPIE 7732*, 2007: 773211.
 31. Vitta S, Yang P. Thermal stability of 2.4 nm period Ni-Nb/C multilayer x-ray mirror. *Appl Phys Lett.* 2000, 77(22): 3654-3656.
 32. Böttger T, Meyer D C, Paufler P, et al. Thermal stability of Mo/Si multilayers with boron carbide interlayers. *Thin Solid Films*, 2003, 444(1): 165-173.
 33. Wu L, Wei S, Wang B, et al. Interlayer microstructure of sputtered Mo/Si multilayers. *J Phys Condens Matter.* 1997, 9(17): 3521.
 34. Zhong Q, Li W, Zhang Z, et al. Optical and structural performance of the Al (1% wtSi)/Zr reflection multilayers in the 17–19nm region. *Opt express.* 2012, 20(10): 10692-10700.
 35. Nedelcu I, Van De Kruijs R W E, Yakshin A E, et al. Thermally enhanced interdiffusion in Mo/Si multilayers. *J Appl Phys.* 2008, 103(8): 083549.
 36. Holloway K, Do K B, Sinclair R. Interfacial reactions on annealing molybdenum-silicon multilayers. *J Appl Phys.* 1989, 65(2): 474-480.
 37. Tu Y, Zhu J, Li H, et al. Structural Changes Induced by Thermal Annealing in Cr/C Multilayers. *Appl surf Sci.* 2014, 313: 341-345.
 38. Jiang Z, Dupuis V, Vidal B, et al. Improvement of the thermal stability of W/C multilayers. *J Appl Phys.* 1992, 72(3): 931-937.
 39. Lodha G S, Pandita S, Gupta A, et al. Thermally induced structural modification in Pt/C X-ray multilayer mirrors fabricated by electron beam evaporation. *Appl Phys A.* 1996, 62(1): 29-32.
 40. DuMond J, Youtz J P. An X - Ray Method of Determining Rates of Diffusion in the Solid State. *J. Appl. Phys*, 1940, 11(5): 357-365.
 41. Dinklage J B. X - Ray Diffraction by Multilayered Thin - Film Structures and Their Diffusion. *J Appl Phys*, 1967, 38: 3781.

Reference

42. Barbee Jr T W, Mrowka S, Hettrick M C. Molybdenum-silicon multilayer mirrors for the extreme ultraviolet. *Appl Opt*, 1985, 24(6): 883-886.
43. <http://www.asml.com/>
44. Kohl J L, Hartmann L W, van Ballegooijen A A, et al. UVCS: an Ultraviolet Coronagraph Spectrometer for SOHO. *The SOHO Mission. Scientific and Technical Aspects of the Instruments*, 1988, 1: 49-54.
45. Golub L, Bookbinder J, DeLuca E, et al. A new view of the solar corona from the transition region and coronal explorer (TRACE). *Physics of Plasmas*. 1999, 6(5): 2205-2216.
46. Podgorski W A, Cheimets P N, Boerner P, et al. SDO-AIA mirror performance. *Proc. SPIE 7438*, 2009: 74380F.
47. <https://www.llnl.gov/news/llnl-multilayer-mirrors-fly-nasa%E2%80%99s-solar-dynamics-observatory>
48. Soufli R, Windt D L, Robinson J C, et al. Development and testing of EUV multilayer coatings for the atmospheric imaging assembly instrument aboard the Solar Dynamics Observatory. *Proc. SPIE 5901*, 2005: 59010M.
49. Windt D L, Donguy S, Seely J F, et al. EUV multilayers for solar physics. *Proc. SPIE 5168*, 2004.
50. Hombourger C, Jonnard P, André J M, et al. Use of layered synthetic microstructures for the quantitative x-ray analysis of light elements. *X - Ray Spectrometry*, 1999, 28(3): 163-167.
51. Le Guen K, Maury H, André J M, et al. X-ray spectroscopic application of Cr/Sc periodic multilayers. *Appl Phys Lett*. 2007, 91(23): 23410-3.
52. Sammar A E, André J M, Ouahabi M, Pardo B, and Barchewitz, R. Monochromateur multicouche á bande passante étroite pour le rayonnement X," *C. R. Acad. Sci. Paris 316-II*, 1993, 1055-1060.
53. Häussler D, Spiecker E, Jäger W, et al. Quantitative TEM characterizations of La/B₄C and Mo/B₄C ultrathin multilayer gratings by the geometric phase method. *Microelectronic engineering*, 2007, 84(3): 454-459.
54. Andreev S S, Mertins H, Platonov Y Y, et al. Multilayer dispersion optics for X-ray

Reference

- radiation. *Nuclear Instruments and Methods in Physics Research Section A: Accelerators, Spectrometers, Detectors and Associated Equipment*, 2000, 448(1): 133-141.
55. Freund A K. Synchrotron hard x-ray beam optics, in: *Complementarity Between Neutron and Synchrotron X-Ray Scattering*, A. Furrer, editor, pp. 329-349, World Scientific, Singapore (1998).
56. Bilderback D H. Wide bandpass monochromator for synchrotron radiation. *Nucl. Instr. & Methods*. 1982, 195: 67-72
57. Kazimirov A, Smilgies D M, Shen Q, et al. Multilayer X-ray optics at CHESS. *Journal of synchrotron radiation*, 2006, 13(2): 204-210.
58. Kortright J B, Kimura H, Nikitin V, et al. Soft x-ray phase retardation using transmission multilayers. *Appl. Phys. Lett.* 1992, 60(24): 2963-2965.
59. Schäfers F, Mertins H C, Schmolla F, et al. Cr/Sc multilayers for the soft-x-ray range. *Appl. Opt.* 1998, 37(4): 719-728.
60. Schäfers F, Yulin S A, Feigl T, et al. At-wavelength Metrology on Sc-based Multilayers for the UV and Water Window. *Proc. SPIE 5188*. 2003.
61. Morawe C, Peffen J C, Dufresne E, et al. Double gradient multilayers for broadband focusing. *Proc. SPIE 5195*. 2003.
62. Mimura H, Handa S, Kimura T, et al. Breaking the 10 nm barrier in hard-X-ray focusing. *Nature Physics*, 2009, 6(2): 122-125.
63. Hatano T, Harada T. Multilayer reflectometry and quantitative analysis of higher order diffraction impurities of grating monochromator. *Journal of Electron Spectroscopy and Related Phenomena*. 2014, 196: 156-158.
64. Spiller E, Segmüller A, Rife J, et al. Controlled fabrication of multilayer soft x-ray mirrors. *Appl. Phys. Lett.* 1980, 37(11): 1048-1050.
65. Barbee T W , *Multilayers for X-ray Optics*, *Opt. Eng.* 1986, 25 (8): 893–915.
66. Gaponov S V, Garin F V, Gusev S L, et al. Multilayer mirrors for soft x-ray and VUV radiation. *Nuclear Instruments and Methods in Physics Research B*, 1983, 208(1): 227-231.
67. Windt D L. IMD—Software for modeling the optical properties of multilayer films. *Computers in physics*, 1998, 12(4): 360-370.

Reference

68. Savage D E, Kleiner J, Schimke N, et al. Determination of roughness correlations in multilayer films for x-ray mirrors. *J. Appl. Phys*, 1991, 69(3): 1411-1424.
69. Li H, Zhu J, Wang Z, et al. Integration method for directly analyzing interface statistics of periodic multilayers from X-ray scattering. *Journal of synchrotron radiation*, 2013, 21(1): 91-103.
70. Becker R S, Golovchenko J A, Patel J R. X-ray evanescent-wave absorption and emission. *Phys. Rev. Lett.* , 1983, 50(3): 153.
71. Barbee T W, Warburton W K. X-ray evanescent-and standing-wave fluorescence studies using a layered synthetic microstructure. *Mater. Lett.* 1984, 3(1): 17-23.
72. Mény C, Jedryka E, Panissod P. Satellite structure of ^{59}Co NMR spectra in some Co alloys. *J. Phys. Condens. Matter.* 1993, 5(10): 1547.
73. Malinowska M, Meny C, Jedryka E, et al. The anisotropic first-neighbour contribution to the hyperfine field in hexagonal-close-packed Co: a nuclear magnetic resonance study of diluted alloys and multilayers. *J. Phys.: Condens. Matter.* 1998, 10(22): 4919.
74. Vickerman J C. *Surface Analysis-The Principal Techniques*. John Wiley & Sons, 1997.
75. Stearns D G, Ceglio N M, Hawryluk A M, et al. TEM and x-ray analysis of multilayer mirrors and beamsplitters. *Proc. SPIE 0688*, 1987.
76. Ferrari A C, Robertson J. Raman spectroscopy of amorphous, nanostructured, diamond-like carbon, and nanodiamond. *Philosophical Transactions of the Royal Society of London. Series A: Mathematical, Physical and Engineering Sciences*, 2004, 362(1824): 2477-2512.
77. Rousseau A D, Windt D L, Winter B, et al. Stability of EUV multilayers to long-term heating, and to energetic protons and neutrons, for extreme solar missions. 2005: 590004-590004.
78. Maury H, Jonnard P, Guen K, et al. Thermal cycles, interface chemistry and optical performance of Mg/SiC multilayers. *The European Physical Journal B*, 2008, 64(2): 193-199.
79. Ejima T, Yamazaki A, Banse T, et al. Aging and thermal stability of Mg/SiC and Mg/Y₂O₃ reflection multilayers in the 25-35 nm region. *Appl. Opt*, 2005, 44(26): 5446-5453.
80. Aquila A, Salmassi F, Liu Y, et al. Tri-material multilayer coatings with high reflectivity

Reference

- and wide bandwidth for 25 to 50 nm extreme ultraviolet light. *Opt. Express*, 2009, 17(24): 22102-22107.
81. Nayeb-Hashemi A A, Clark J B. The Mg-Zr (Magnesium-Zirconium) system. *Journal of Phase Equilibria*, 1985, 6(3): 246-250.
 82. Nayeb-Hashemi A A, Clark J B. The Co-Mg (cobalt-magnesium) system. *Journal of Phase Equilibria*, 1987, 8(4): 352-355.
 83. Zhu J, Zhou S, Li H, et al. Comparison of Mg-based multilayers for solar He II radiation at 30.4 nm wavelength. *Appl. Opt*, 2010, 49(20): 3922-3925.
 84. Zhu J, Zhou S, Li H, et al. Thermal stability of Mg/Co multilayer with B₄C, Mo or Zr diffusion barrier layers. *Opt. Express*, 2011, 19(22): 21849-21854.
 85. Li H, Zhu J, Zhou S, et al. Zr/Mg multilayer mirror for extreme ultraviolet application and its thermal stability[J]. *Appl. Phys. Lett*, 2013, 102(11): 111103.
 86. Stearns D G. X-ray scattering from interfacial roughness in multilayer structures. *J. Appl. Phys*, 1992, 71(9): 4286-4298.
 87. Hu M H, Le Guen K, André J M, et al. Investigation of the thermal stability of Mg/Co periodic multilayers for EUV applications. *Appl. Phys. A*, 2012, 106(3): 737-745.
 88. Li W, Zhu J, Ma X, et al. Geometrical factor correction in grazing incident x-ray fluorescence experiment. *Review of Scientific Instruments*, 2012, 83(5): 053114.
 89. B. Predel, *Phase Equilibria, Crystallographic and Thermodynamic Data of Binary Alloys*, Landolt-Börnstein, New Series, Group IV, Vol. 5, edited by O. Madelung (Springer, Berlin 1991).
 90. Le Guen K, Hu M H, André J M, et al. Development and interfacial characterization of Co/Mg periodic multilayers for the EUV range. *The Journal of Physical Chemistry C*, 2010, 114(14): 6484-6490.
 91. Vitos L, Ruban A V, Skriver H L, et al. The surface energy of metals. *Surface Science*, 1998, 411(1): 186-202.
 92. Takenaka H, Nagai K, Ito H, et al. Soft X-ray reflectivity and structure evaluation of CoCr/C multilayer X-ray mirrors for spectral region around 6nm. *Nuclear Instruments and Methods in Physics Research Section A: Accelerators, Spectrometers, Detectors and Associated Equipment*, 2001, 467: 337-340.

Reference

93. Artyukov I A, Bugayev Y, Devizenko O Y, et al. Carbon window soft x-ray imaging using multilayer optics. *Optics & Photonics 2005. International Society for Optics and Photonics*, 2005: 59190E-59190E-10.
94. Ferrari A C, Robertson J. Interpretation of Raman spectra of disordered and amorphous carbon. *Physical review B*, 2000, 61(20): 14095.
95. Robertson J. Properties of diamond-like carbon. *Surf. Coat. Technol.* 1992, 50(3): 185-203.
96. Funada Y, Awazu K, Shimamura K, et al. Thermal properties of DLC thin films bombarded with ion beams. *Surf. Coat. Technol.* 1998, 103: 389-394.
97. Cho N H, Veirs D K, Ager Iii J W, et al. Effects of substrate temperature on chemical structure of amorphous carbon films. *J. Appl. Phys.* 1992, 71(5): 2243-2248.
98. Dillon R O, Woollam J A, Katkanant V. Use of Raman scattering to investigate disorder and crystallite formation in as-deposited and annealed carbon films. *Physical Review B*, 1984, 29(6): 3482.
99. Jiang Z, Vidal B, Desrousseaux G, et al. Raman scattering from carbon in tungsten/carbon multilayer films. *J. Appl. Phys.* 1993, 74(1): 249-254.
100. Das N, Mitra J, Murty B S, et al. Miedema model based methodology to predict amorphous-forming-composition range in binary and ternary systems. *Journal of Alloys and Compounds*, 2013, 550: 483-495.
101. Wilson G M, Saied S O, Field S K. Mechanical and physical properties of C and C–Cr sputter coatings measured at the nano-scale. *Thin Solid Films*, 2007, 515(20): 7820-7828.
102. Artyukov I A, Bugayev Y, Devizenko O Y, et al. Carbon window soft x-ray imaging using multilayer optics. *Optics & Photonics 2005. International Society for Optics and Photonics*, 2005: 59190E-59190E-10.
103. The diffraction information for Co is obtained from ICDD-PDF No.05-2727 and No.15-0806
104. Kubota H, Ishio S, Miyazaki T, et al. Giant magnetoresistance and interlayer exchange coupling in Ni-Co/Cu multilayer films. *Journal of magnetism and magnetic materials*, 1994, 129(2): 383-388.

Reference

105. De Boer D K G, Leenaers A J G, Van den Hoogenhof W W. The profile of layered materials reflected by glancing-incidence X-ray analysis. *Appl. Phys. A*. 1994, 58(3): 169-172.
106. Wagner C C, Riggs W M, Davis L E, Moulder J F, and Mullenberg G E, *Handbook of X-Ray Photoelectron Spectroscopy* (Perkin-Elmer Corporation, Physical Electronics Division, Eden Prairie, Minnesota, 1979)
107. Mavel G, Escard J, Costa P, et al. ESCA surface study of metal borides. *Surface Science*, 1973, 35: 109-116.
108. Galuska A A, Uht J C, Marquez N. Reactive and nonreactive ion mixing of Ti films on carbon substrates. *Journal of Vacuum Science & Technology A*, 1988, 6(1): 110-122.
109. Berkeley Center for X-ray Optics (<http://www-cxro.lbl.gov>).
110. Chkhalo N I, Künstner S, Polkovnikov V N, et al. High performance La/B4C multilayer mirrors with barrier layers for the next generation lithography. *Appl. Phys. Lett.* 2013, 102(1): 011602.
111. Makhotkin I A, Zoethout E, van de Kruijs R, et al. Short period La/B and LaN/B multilayer mirrors for ~ 6.8 nm wavelength. *Opt. Express*, 2013, 21(24): 29894-29904.
112. Barthelmess M, Bajt S. Thermal stability on Mo/B4C multilayers. *SPIE Optics Optoelectronics. International Society for Optics and Photonics*, 2011: 807710-807710-11.
113. Feigl T, Lauth H, Yulin S, et al. Heat resistance of EUV multilayer mirrors for long-time applications. *Microelectronic engineering*, 2001, 57: 3-8.
114. Bajt S, Barbee Jr T W. High reflectance and low stress Mo2C/Be multilayers: U.S. Patent 6,229,652. 2001-5-8.
115. Choueikani F, Bridou F, Lagarde B, et al. X-ray properties and interface study of B4C/Mo and B4C/Mo2C periodic multilayers. *Appl. Phys. A*, 2013, 111(1): 191-198.
116. Niibe M, Nii H, Sugie Y. Stress changes and stability of sputter-deposited Mo/B4C multilayer films for extreme ultraviolet mirrors. *Jpn. J. Appl. Phys.* 2002, 41(5R): 3069-3075.
117. Hoffman D W, Thornton J A. The compressive stress transition in Al, V, Zr, Nb and W metal films sputtered at low working pressures. *Thin Solid Films*, 1977, 45(2): 387-396.

Reference

118. Windt D L. Stress, microstructure, and stability of Mo/Si, W/Si, and Mo/C multilayer films. *J. Vac. Sci. Technol. A*, 2000, 18(3): 980-991.
119. Montcalm C. Reduction of residual stress in extreme ultraviolet Mo/Si multilayer mirrors with postdeposition thermal treatments. *Opt. Eng.* 2001, 40(3): 469-477.
120. Li H, Zhu J, Wang Z, et al. Asymmetrical diffusion at interfaces of Mg/SiC multilayers. *Opt. Mater. Express*, 2013, 3(5): 546-555.
121. de Rooij-Lohmann V, Veldhuizen L W, Zoethout E, et al. Chemical interaction of B₄C, B, and C with Mo/Si layered structures. *J. Appl. Phys.* 2010, 108(9): 094314.
122. Freund L B, Floro J A, Chason E. Extensions of the Stoney formula for substrate curvature to configurations with thin substrates or large deformations. *Appl. Phys. Lett.* 1999, 74(14): 1987-1989.
123. Detor A J, Hodge A M, Chason E, et al. Stress and microstructure evolution in thick sputtered films. *Acta materialia*, 2009, 57(7): 2055-2065.
124. Hoffman R W. The mechanical properties of thin condensed films. *Physics of thin films*, 1966, 3: 211-273.

Appendix: other publications

Publication as author and co-author:

1. Jingtao Zhu, Yuchun Tu, Haochuan. Li, Shuanpeng Yue, Qiushi Huang, Aiguo Li, Zhanshan Wang, X-ray nanometer focusing at the SSRF basing on multilayer Laue lens, *Thin Solid Films* (2014) submitted.
2. Tu Yuchun, Song Zhuqing, Huang Qiushi, et al, Fabrication of laterally graded periodic Mo/Si multilayer using magnetron sputtering technology, *High Power Laser and Particle Beams*, (2011), 23(09), 2419-2422, in Chinese.
3. Wenbin Li, Xiaoyue Yang, Jingtao Zhu, Yuchun Tu, Baozhong Mu, Haisheng Yu, Xiangjun Wei, Yuying Huang and Zhanshan Wang, Correction method for the self-absorption effects in fluorescence extended X-ray absorption fine structure on multilayer samples, *Journal of Synchrotron Radiation*, (2014) 21, 561–567.
4. He Shifeng, Tu Yuchun, Feng Zhixiang, Yue Shuaipeng, Wang Fengli, Zhu Jingtao, Stress analysis of high reflective multilayers fabricated by magnetron sputtering. *High Power Laser and Particle Beams*, (2014), 26(05): 40021-40024, in Chinese
5. Jingtao Zhu, Qiushi Huang, Haochuan Li, Yuchun Tu, Zhuqing Song, Lei Pan, Li Jiang, Xiaoqiang Wang, Fengli Wang, Zhong Zhang, Zhanshan Wang, Lingyan Chen, Multilayer Optics and Applications in EUV and X-ray region, *Proc. of SPIE* (2010) 79952R-1.

We also participated in the study of multilayer Laue lens. A multilayer Laue lens (MLL) was fabricated as a hard x-ray focusing device. WSi_2/Si system is chosen owing to their excellent optical properties and relatively sharp interface. The multilayer was fabricated by using direct current (DC) magnetron sputtering technology. Thickness of each layer was determined by scanning electron microscopy (SEM) image analysis with marking layer. The focusing property of the MLL was measured at Beamline 15U, Shanghai Synchrotron Facility (SSRF). One-dimensional (1D) focusing resolutions of 92 nm are obtained at photon energy of 14 keV. The paper about this study has been submitted as follows:

X-ray nanometer focusing at the SSRF basing on multilayer Laue lens

Jingtao Zhu^{1*}, Yuchun Tu¹, Haochuan Li¹, Shuaipeng Yue¹, Qiushi Huang¹, Aiguo Li²,
and Zhanshan Wang¹

¹)MOE Key Laboratory of Advanced Micro-structured Materials, School of Physics Science and Engineering, Tongji University, Shanghai 200092, China

²) Shanghai Synchrotron Radiation Facility, Shanghai Institute of Applied Physics, Chinese Academy of Science, Shanghai 201204, China

Abstract: We designed and fabricated a multilayer Laue lens (MLL) as a hard x-ray focusing device. WSi_2/Si multilayers were chosen owing to their excellent optical properties and relatively sharp interface. The multilayer was fabricated by using direct current (DC) magnetron sputtering technology. Thickness of each layer was determined by scanning electron microscopy (SEM) image analysis with marking layer. The focusing property of the MLL was measured at Beamline 15U, Shanghai Synchrotron Facility (SSRF). One-dimensional (1D) focusing resolutions of 92 nm are obtained at photon energy of 14 keV.

Keywords: hard X-ray; nano-focusing; multilayer Laue lens (MLL); synchrotron radiation

PACS : 42.79.Ci, 07.85.Tt

*E-mail address: jtzhu@tongji.edu.cn

1 Introduction

X-ray microscopy has been found numerous applications in materials sciences, medicine, biology, environmental sciences and many other fields by utilizing analytical techniques such as diffraction, x-ray fluorescence and spectroscopy, as well as imaging techniques using absorption and phase contrast. Among these analytical methods, the resolution, signal strength and contrast must be as high as possible and the development of a hard-X-ray focusing device is important for meeting these requirements [1, 2]. There are many types of hard X-ray focusing devices utilizing reflection, refraction and diffraction optics. In the past decade, rapid advancement in micro-fabrication technology, high-precision surface polishing, controlled layer deposition and precision metrology have led to the realization of hard X-ray

Appendix

focusing to nanometer dimensions [3]. Zone plates have realized the highest resolution of 10-12 nm in the soft X-ray range [4]. Capability of focusing to 47 nm with a compound refractive lens has been experimentally demonstrated at wavelength of 0.06 nm [5]. A line focus with a width of 26nm was achieved with a planar waveguide at photon energy of 13.3 keV [6]. Reflective mirrors have shown great progress recently with the advance of precision manufacturing techniques, it breaks the 10 nm barrier in hard-X-ray focusing [7].

Diffraction optics is intrinsically well suited to achieve a high spatial resolution because a large numerical aperture (NA) can be achieved. A novel approach to making diffraction optics with high NA is Multilayer-Laue-Lens (MLL) [8]. The MLL can be considered as a special type of zone plate and used in Laue geometry. It is fabricated by depositing the depth-graded multilayer inversely on a flat substrate then slicing and thinning the multilayer sample to an ideal cross-section depth. Through this process, MLL can reach a much larger aspect-ratio (the ratio of cross section depth to the outermost layer thickness) compared with zone plates, and this make it capable of focusing hard X-rays with higher efficiency [9]. Based on this method, a line focus of 16 nm width with efficiency of 31% has been obtained at photon energy of 19.5 keV [10]. To obtain the point focus that most applications require, two MLL's have to be placed in series in a crossed geometry. A nano-scale 2D imaging with $25\text{nm} \times 27\text{nm}$ resolution was reported recently [11]. In this paper, we report the design, fabrication and characterization of a partial MLL structure with a width of 10 nm outermost zone and 1582 zones. The multilayer was fabricated by using direct current (DC) magnetron sputtering technology. Thickness of each layer was determined by scanning electron microscopy (SEM) images. The focusing property of the MLL was measured at the Shanghai Synchrotron Facility (SSRF). One-dimensional (1D) focusing resolutions of 92 nm are obtained at X-ray photon energy of 14 keV.

2 Design and fabrication of MLL

The MLL was designed at photon energy of 14 keV using WSi_2 and Si as the material combination. In the depth-graded multilayer, the minimum layer thickness was designed to be 10 nm, while the total multilayer thickness was $27 \mu\text{m}$, and the number of layers was 1582. The focusing property was calculated using the Fresnel-Kirchhoff diffraction formula [14].

Appendix

During deposition a few thickest layers contributing little to the focus and can be omitted. Thus, the total thickness of the actual deposited multilayer is thinner than that of designed structure. The focal length was designed to be 7.95 mm. The calculated intensity profile in the focal plane of the MLL is shown in Fig.1 and full width of half maximum (FWHM) of the peak is 23.5 nm.

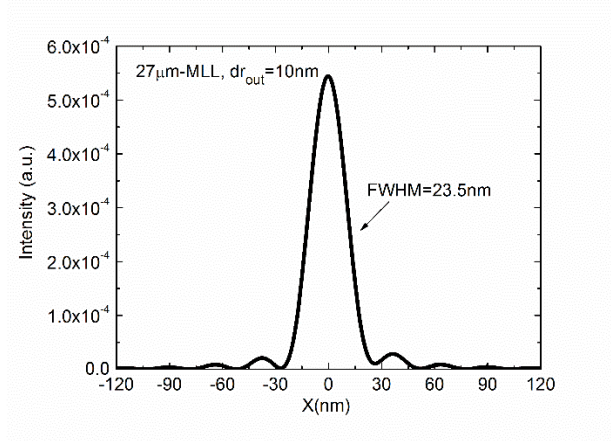


Fig.1. Intensity profile in the focal plane of the MLL structures.

The fabrication of the MLL includes two parts. The first part is the deposition of the depth-graded multilayer. The material combination of WSi_2/Si is selected to fabricate the MLL due to its stable stress property and sharp interfaces [15, 16]. The multilayer is deposited on a super-polished silicon substrate using direct current magnetron sputtering technology. The base pressure before deposition is 2.0×10^{-4} Pa and argon is used as the working gas with a pressure of 1.5 mtorr. The layer thicknesses of the designed MLL are in the range of 10.0-48.6 nm. The outermost thinnest layer is the first layer deposited. Secondly, subsequent to deposition, the multilayer is sectioned and thinned to the requisite optical depth to form the halves of the MLL. More details have been described in Ref. [17].

3 Characterization of the MLL

3.1 Scanning electron microscope (SEM)

The cross-section of the multilayer was observed by a scanning electron microscope (SEM) after the sampling process as shown in Fig.2. Fig.2 (a) shows the entire multilayer structure. Figs.2 (b), (d) are magnified images of the areas close to the surface and substrate,

Appendix

Fig.3(c) refers to the middle area of the entire multilayer. It can be seen that the multilayer structure is undamaged after the repeated grinding and polishing. All the layer interfaces keep flat and sharp. The image was converted into a binary one and the layer thicknesses were directly calculated as reported in Ref. [18]. The measured layer thickness distribution is shown in Fig.4 where the designed structure is also shown for comparison. Different sub-areas from the substrate to the surface are represented by numbers 1-17 in Fig.3. Fig.3 (a) is the result of the layer structure while (b) is the relative errors between the deposited and designed layer thicknesses, $(d_{\text{meas}} - d_{\text{desi}})/d_{\text{desi}}$. The result demonstrates that the structure fabricated conforms to the designed one and the error of the thickness curve are less than $\pm 7\%$.

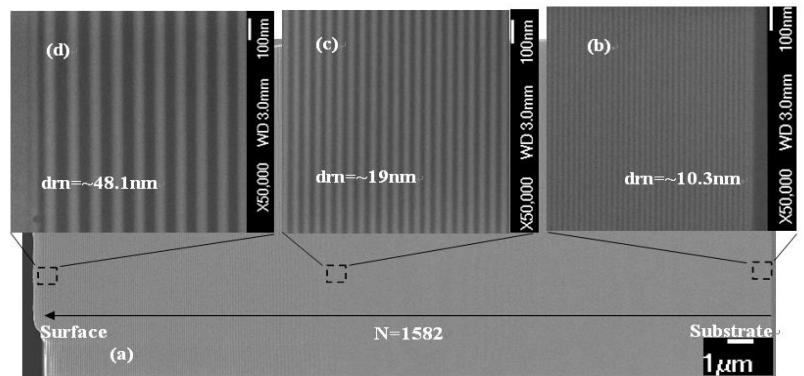


Fig.2. SEM images of the cross-section of 27 μm -MLL after the sampling process.

3.2 Nano-focusing measurement

The x-ray nano-focusing measurement reported here were performed at beamline 15U of Shanghai synchrotron radiation facility (SSRF). The focal beam size was measured by the knife-edge method. A nickel (Ni) film was aligned and then scanned across the focus using a nanometer translation-stage. Geometrical relationships among the incident x-ray, the MLL, and the Ni film are shown in Fig. 4. The intensity of Ni $K\alpha$ lines was monitored by the fluorescence detector and shows abrupt change when the Ni knife-edge passed through the focal line.

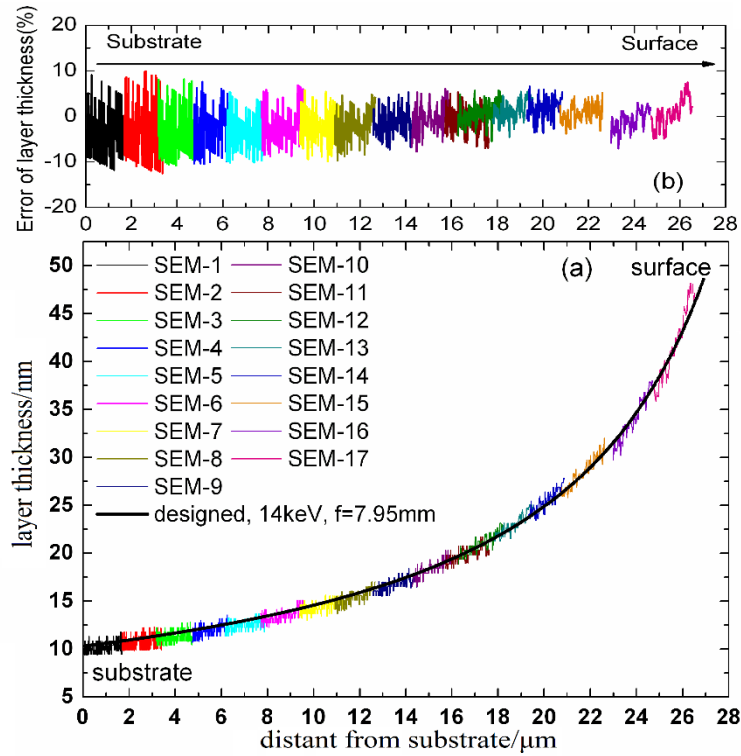


Fig.3. (color online) Layer thickness distribution of the deposited 27 μm -thick multilayer.

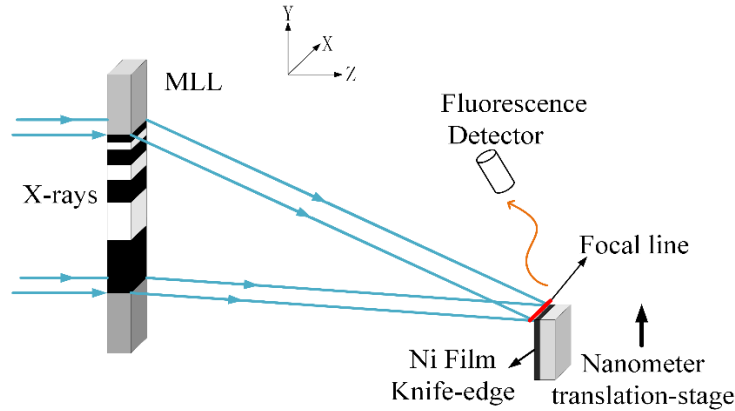


Fig.4. (color online) Schematic of the focusing measurement of MLL on BL 15U, SSRF

The measured focusing results of the 27 μm -MLL are shown in Fig.5. Fig.5 (a) is a color map of fluorescence intensity by two dimension scanning of the Ni knife-edge. It suggests that the width of focal line is minimum between 42.1 mm and 42.2 mm in the beam direction, which demonstrates the focus. Fig.5 (b) is a curve of fluorescence intensity along the scanning direction at the position of focus. The differentiation of the smoothed curve of intensity displays a peak and the FWHM of the peak closely approximates to the focusing resolutions.

Appendix

The width of the focal line at photon energy of 92 nm (FWHM), shown in Fig.5 (c). This measurement has been performed several times to ensure repeatability.

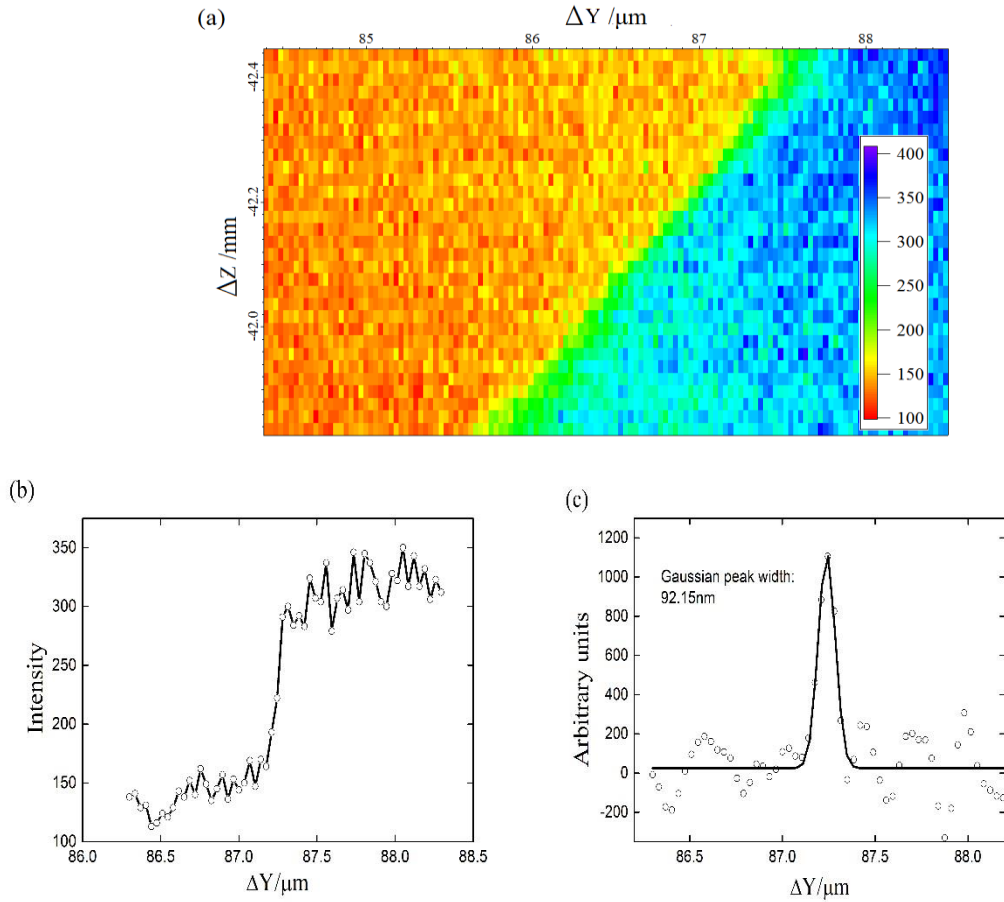


Fig.5. (a) (color online) The 2D fluorescence intensity scanning near the focal plane;
(b) The 1D fluorescence intensity scanning at the position of focus
(c) The differentiation of the smoothed curve of intensity

It should be noted that the focus of the MLL is still not perfect. The discrepancy between the measured width and the theoretical value is attributed to three reasons. Firstly, the layer position errors of the depth-graded multilayer and the structural damage induced by the sampling process would broaden the focal line. Secondly, the minimal scanning step of nanometer translation-stage is 35 nm which is not very precise relative to the width of focal line. Thirdly, the wave front aberration of the incident beam and the vibration of the measurement system will also broaden the focus. If these will be improved, better resolution could be expected in the future work.

4. Conclusion

A 27 μm -thick multilayer Laue lens with an outermost layer thickness of 10 nm was designed and fabricated. The focusing property of the MLL was measured at the SSRF. The measured results show that a focusing resolution of 92 nm was achieved at 14 keV. Up to now, this is the best results for MLL in the hard X-ray region in China. More efforts should be made to improve the fabrication process and the nano-focusing experiment system to further decrease the resolution of the MLL.

Acknowledgement:

This work was supported by National Basic Research Program of China (No.2011CB922203), and National Natural Science Foundation of China (Nos. 11375131 and U1432244).

Reference

- (1) A. Sakdinawat, D. Attwood. *Nat. Photonics*, 4, (2010) 840
- (2) H. Bluhma, K. Andersson, T. Araki, et al. *J. Electron. Spectrosc. Relat. Phenom*, 150, (2006)86
- (3) W. Chao, B. Harteneck, J. Liddle, Erik. Anderson, D. Attwood., *Nature*, 435, (2005) 1210
- (4) J. Vila-Comamala, K. Jefimovs, J. Raabe, T. Pilvi, R. Fink, M. Senoner, A. Maassdorf, M. Ritala, C. David, *Ultramicroscopy*, 109, (2009)1360
- (5) C. G. Schroer, O. Kurapova, J. Patommel, P. Boye, J. Feldkamp, B. Lengeler, M. Burghammer, C. Riekell, L. Vincze, A. van der Hart and M. Kuehler, *Appl.Phys.Lett.*, 87, (2005) 124103
- (6) M. Zwanenburg, J. Bongaerts, J. Peters, D. Riese, J. van der Veen, *Physica B*, 283, (2000) 285
- (7) H. Mimura, S. Handa, T. Kimura, et al. *Nat.Phys.*, 6, (2010)122
- (8) H. Yan, H. Kang, R. Conley, C. Liu, A. Macrander, G. Stephenson, J. Maser, *X-ray Optics and Instrumentation*, (2010) 401854
- (9) H. Kang, J. Maser, G. Stephenson, C. Liu, R. Conley, A.T. Macrander, S. Vogt, *Phys. Rev. Lett.*, 96, (2006) 127401
- (10) H. Kang, H. Yan, R. Winarski, M. Holt, J. Maser, C. Liu, R. Conley, S. Vogt, A. Macrander, G. Stephenson, *Appl.Phys.Lett.*, 92, (2008) 1114
- (11) H. Yan, V. Rose, D. Shu, E. Lima, H. Kang, R. Conley, C. Liu, N. Jahedi, A. Macrander, G. Stephenson, M. Holt, Y. Chu, M. Lu, and J. Maser, *Opt. Express*, 19, (2011) 15069
- (12) Q. Huang, H. Li, Z. Song, J. Zhu, Z. Wang, A. Li, S. Yan, C. Mao, H. Wang, F. Yan, L. Zhang Ling, X. Yu, P. Liu and M. Li, *Chinese Physics C*, 37, (2013) 028002
- (13) Q. Huang, H. Li, Z. Song, J. Zhu, S. Tian, Z. Wang, L. Yan, *Acta. Photonica. Sinica*, 38, (2009, in Chinese) 2299
- (14) D. Attwood, *Soft X-rays and Extreme Ultra violet Radiation: Principles and Applications*.

Appendix

- Cambridge: Cambridge University Press, (1999) 349-356
- (15) C. Liu, B. Shi, J. Qian, R. Conley, H. Yan, M. Wiczorek, A. Macrander, J. Maser and G. Stephenson, AIP Conf.Proc., 1234, (2010) 47
- (16) C. Liu, R. Conley, A. Macrander, Proc.of SPIE, 6317, (2006) 63170J
- (17) Q. Huang, J. Zhu, H. Li, Z. Shen, X. Wang, Z. Wang, Y. Tang, Chin. Opt. Lett., 10, (2012) 013103
- (18) N. Jahedi, R. Conley, B. Shi, J. Qian, K. Lauer, A. Macrander, Nucl. Instrum. Methods A., 616, (2013) 89